GAMMA-RAY OBSERVATIONS OF X-RAY BINARIES

A Dissertation

Submitted to the Faculty

of

Purdue University

by

Angelo Varlotta

In Partial Fulfillment of the

Requirements for the Degree

of

Doctor of Philosophy

December 2013

Purdue University

West Lafayette, Indiana

To my family and friends for their support.

Ebbene, forse voi credete

che l'arco senza fondo della volta spaziale

sia un vuoto vertiginoso di silenzi.

Vi posso dire allora che verso

questa terra sospettabile appena

l'universo già dilaga di pensieri.

MARIO SOCRATE, *Favole paraboliche*

Well, maybe you think

that the endless arch of the space vault

is a giddy, silent hollowness.

But I can tell you that,

overflowing with thought,

the universe is approaching

this hardly guessable earth.

MARIO SOCRATE, *Parabolic Fables*

ACKNOWLEDGMENTS

There is a long list of people I would like to thank for all of these years in graduate school at Purdue University. First of all though, I would like to thank my parents, who have supported and encouraged me in my passion for astronomy.

I remember a professor who said once that "your advisor is more important than your father, since he will help you graduate and find a job". To this day, I still think that is so true, so I really want to thank my advisor Wei Cui, who has (patiently!) helped me through the graduation process. I also want to thank John Finley, who always has been a positive (and enjoyable) presence in the department and especially in our weekly VERITAS meetings. A big thanks also goes to Glenn Sembroski for the (many, many) times I had to go to his office and ask for help!

A great thanks also goes to Michael McCollough at the Harvard-Smithsonian Center for Astrophysics in Cambridge, MA, for learning many things about Cygnus X-3, including the capricious nature of the source that seems to go off and do something interesting just when you can't observe it!

I have had the pleasure to meet in graduate school many friends and colleagues, who have since gone off into the wide world pursuing their own dreams and aspirations. Of these at Purdue University, I need to mention my fellow colleagues and friends Miguel Araya, Talvikki Hovatta, Kostas Gourgouliatos, David Lomiashvili, Edwin Antillon, Eric Clausen-Brown, Daniel Gall, Ben Zitzer, Qi Feng, Suzanne Lorenz, Kari Frank, Mary Kertzman, Jignesh Mehta, Joey Richards and Andrea Morandi.

Out at the Whipple Observatory base camp I had the pleasure to meet most of the members of VERITAS Collaboration, including some fellow Italians such as Victor Acciari, Andrea Cesarini and Nicola Galante, who have been able to make Italy feel not so far away even in the midsts of the Arizona desert.

TABLE OF CONTENTS

LIST OF TABLES

LIST OF FIGURES

SYMBOLS

Z	Atomic Number
ω_c	Critical Frequency
L_{Edd}	Eddington Luminosity
e	Electron Charge
m_e	Electron Mass
n_e	Electron Number Density
g_{ff}	Gaunt Factor
r_0	Gyration Radius
n_i	Ion Number Density
σ_{KN}	Klein-Nishina Cross Section
γ	Lorentz factor
B	Magnetic Field
E_{nuc}	Nuclear Energy
U_{ph}	Photon Energy Density
h	Planck Constant
m_p	Proton Mass
T	Temperature
σ_T	Thomson Cross Section
c	Velocity of Light
β	Velocity Relative to Speed of Light
$\beta_\perp$	Perpendicular Component of β With Respect to the Magnetic Field
ϵ_γ	Gamma-Ray Photon Energy
ϵ_*	Stellar Photon Energy
L_x	X-Ray Luminosity

ABBREVIATIONS

AGILE	Astro-rivelatore Gamma ad Immagini LEggero
AGN	Active Galactic Nuclei
AMI-LA	Arcminute Microkelvin Imager - Large Array
BAT	Burst Alert Telescope (Swift)
BATSE	Burst And Transient Source Experiment (CGRO)
CGRO	Compton Gamma-Ray Observatory
COMPTEL	COMPton TELescope (CGRO)
CTA	Cherenkov Array Telescope
EGRET	Energetic Gamma Ray Experiment Telescope (CGRO)
GBM	Gamma-Ray Burst Monitor (Fermi)
HE	High Energy
HEGRA	High Energy Gamma Ray Array
HESS	High Energy Stereoscopic System
HMXB	High-Mass X-Ray Binary
IACT	Imaging Atmospheric Cherenkov Telescope
LMXB	Low-Mass X-Ray Binary
LAT	Large Area Telescope (Fermi)
MAGIC	Major Atmospheric Gamma Imaging Cherenkov Telescope
MAXI	Monitor of All-sky X-ray Image
OSSE	Orientation Scintillation-Spectrometer Experiment (CGRO)
PAIRITel	Peters Automated InfraRed Imaging Telescope
SNR	Supernova Remnant
UVOT	UV/Optical Telescope (Swift)
VERITAS	Very Energetic Radiation Imaging Telescope Array System
VHE	Very High Energy

XRT   X-ray Telescope (Swift)

ABSTRACT

Varlotta, Angelo Ph.D., Purdue University, December 2013. Gamma-Ray Observations of X-Ray Binaries. Major Professor: Wei K. Cui.

The detection of GeV/TeV emission from X-ray binaries (XRBs) has established a new class of high-energy (HE, >0.1 GeV) and very-high-energy (VHE, >100 GeV) gamma-ray emitters. XRBs are formed by a compact object, either a neutron star or a black hole, and by an optical companion star. Some XRBs are known to possess collimated relativistic jets, and are called microquasars. VERITAS has conducted observations of the high-mass X-ray binary (HMXB) 1A 0535+262 and of the microquasar Cygnus X-3. Many theoretical models predict VHE emission when these sources manifest persistent relativistic jets or transient ejections. In light of these considerations, VERITAS has been employed to study the two XRBs for possible TeV emission. With the aid of VERITAS, it can be possible to cast light on the particular conditions which could trigger VHE emission. This can help us understand the mechanisms that may trigger VHE gamma-ray emission, thus improving our knowledge of particle acceleration and radiative processes in the jets. The implications have far reaching consequences on the understanding of other XRBs and microquasars and also of active galactic nuclei, which are in many ways similar to microquasars and are prominent VHE gamma-ray sources themselves.

1. TeV Gamma-Ray Astronomy

Gamma rays make up part of the highest energy radiation of the electromagnetic spectrum. They are produced by non-thermal processes in the most extreme conditions and environments of the universe. Their detection constitutes an important probe for understanding the nature of the extreme environments they are generated in. The nature of the acceleration mechanisms and the understanding of the particle interactions drive the astronomical community in the endeavor of high-energy astrophysics.

Since they lack charge, gamma-ray photons propagate through space without changing their direction. Therefore, they preserve the information of their point of origin. As they travel through space, gamma rays don't lose a significant part of their energy, but their flux decreases with increasing energy due to the intrinsic nature of the sources. Gamma rays can be detected from space, but due to the energy dependence of the flux and the cost of deployment of large collection areas in satellites, space-based detectors have been limited to the detection of gamma rays below ~ 100 GeV. However, new technologies and increased support from the gamma-ray astronomical community may improve the condition of larger space-borne detectors in the near future.

The atmosphere blocks all gamma-ray radiation from reaching the surface of the Earth, making it impossible to directly detect gamma-ray emission. Fortunately though, gamma rays are known to initiate air showers of charged particles and Cherenkov radiation in the atmosphere, which carries the information of the original gamma-ray photon. Unfortunately, cosmic rays also produce similar air showers and contribute to a very significant background noise which makes the detection of the gamma-ray photons difficult. In the 1980's, the Whipple collaboration had shown that the Imaging Atmospheric Cherenkov technique could be successfully employed

to detect, with high significance, gamma-ray initiated air showers from the more numerous air showers started by cosmic rays. This technique has been used to detect gamma-ray sources with energy ranges from ~ 100 GeV to ~ 10 TeV, paving the way for ground-based VHE astronomy.

1.1 History of Gamma-Ray Astronomy

The history of space-based and ground-based gamma-ray astronomy are so intertwined that one needs to illustrate the history of both fields to get the complete picture of the development of gamma-ray astronomy. The following paragraphs are an attempt to show the paths that both space-based and ground-based gamma-ray astronomy have taken over the course of the many years, since their beginning in the early twentieth century. It also creates the opportunity to list the main achievements of the field and to illustrate how our knowledge of high-energy astrophysics has expanded over the course of time.

1.1.1 Space-Based Gamma-Ray Astronomy

The history of gamma-ray astronomy starts in 1912 with the discovery of cosmic rays by Victor Hess in Vienna and confirmed a year later by Werner Kolhörster in Berlin, through ionization rate measurements at high altitudes in the atmosphere. At the time of the discovery, the radiation was called "high-altitude radiation" and not "cosmic radiation". The term "cosmic rays" was later defined by Millikan in the mid-1920s, who proposed that gamma rays were responsible for the measured ionization in the upper atmosphere. We currently know that this did not mark the actual birth of gamma-ray astronomy. It was in fact later in 1929 that Bothe and Kolhörster discovered the corpuscular nature of the "high-altitude radiation" through Geiger counters in coincidence, pushing back the real start of the history of gamma-ray astronomy to some years later.
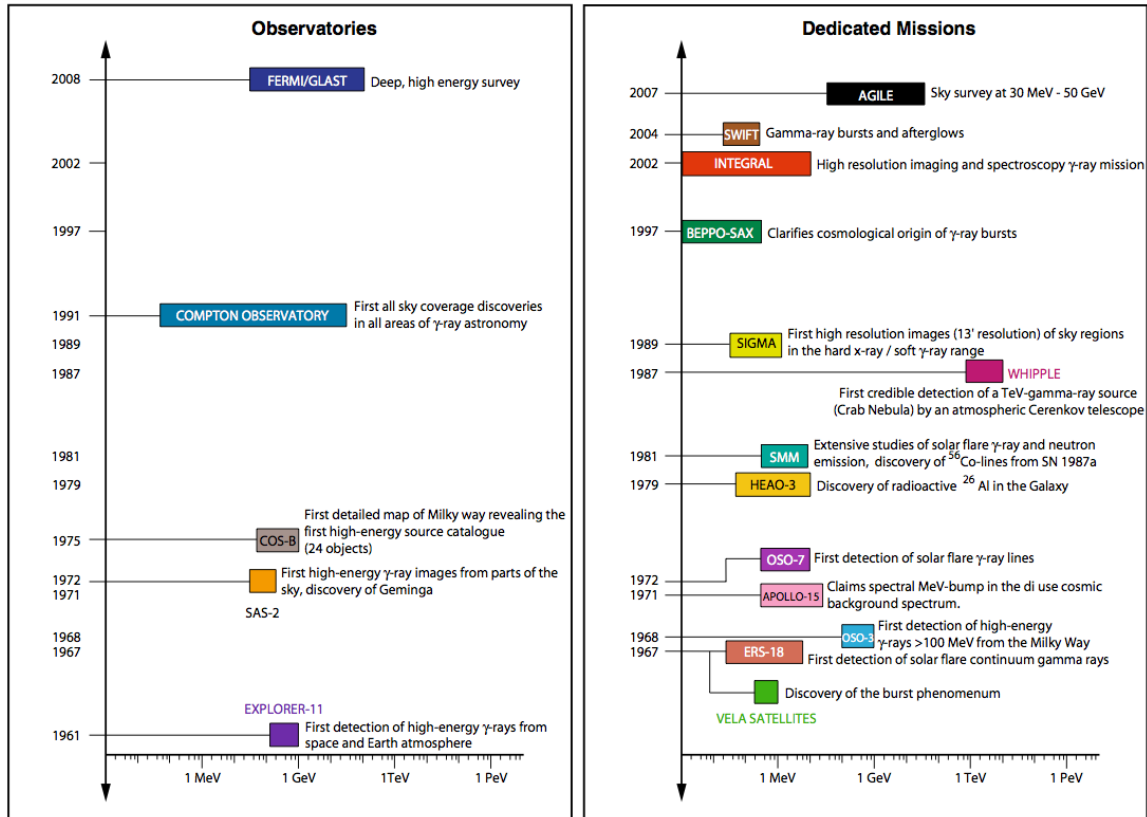
Figure 1.1.: Time line of the history of gamma-ray astronomy [3].

The most famous theoretical prediction on cosmic gamma-ray sources was made in 1958 when the possibility of detecting MeV photons was first discussed [1]. As a result, the first efforts with ballon and satellite experiments started in earnest in the early 1960s in order to detect the first cosmic gamma rays. Today we know that these first predictions were actually too optimistic and that the first instruments lacked the sensitivity and complexity that were necessary to detect gamma-ray sources. Gamma-ray fluxes from celestial objects are extremely small, and this is why it took gamma-ray astronomy such a long time to reach the level of maturity and refinement necessary to explore the field. Large collection areas and sophisticated instruments turned out to be absolutely necessary for gamma-ray observations [2].

The first real cosmic gamma-ray detections were made by the Explorer-11 and OSO-3 satellites in 1961 and 1968, respectively. Both experiments were designed to

Figure 1.2.: An image of the ESA mission COS-B. Credit: ESA.

measure high-energy gamma-rays above 50 MeV. Explorer-11 discovered a total of 31, and OSO-3 621 cosmic gamma-rays. The OSO-3 results showed clear evidence for gamma-ray emission from the Milky Way. In 1967, the network of Vela satellites from the United States Department of Defense, which were designed to monitor nuclear tests in the atmosphere after the signature of the Nuclear Test Ban Treaty in 1963, made the discovery of cosmic-ray gamma-ray bursts, or GRBs. The discovery was later declassified and in 1973 publicized by the astronomical community as a new class of astronomical phenomena, whose origin were to remain a puzzle for many more years to follow.

A major step forward in gamma-ray astronomy was accomplished by the two satellite missions COS-B and SAS-2 in the 1970s, which provided clear evidence for the first significant gamma-ray detections. These experiments operated in the 35 MeV-5 GeV energy range, and were capable of detecting the diffuse gamma-ray flux concentrated along the galactic plane and the isotropic extragalactic gamma-ray emission. The satellites were capable of providing evidence for as many as 25 gamma-

ray point sources, including the Crab and Vela pulsars and the AGN 3C 273. The strongest sources were the Crab and Vela pulsars, and a source called Geminga, which remained unidentified for another twenty years, and which proved to be a pulsar as well.

In the field of cosmic gamma-ray line spectroscopy, a major landmark was achieved by the German spectrometer onboard the HEAO-3 with the detection of the nucleosynthetic line from the radioactive decay of ^{26}Al at 1.809 MeV, which was discovered in the direction of the Galactic center region.

The 1990s are marked as the start of the golden age of gamma-ray astronomy, with the launch of the French telescope SIGMA onboard the Russian GRANAT mission in 1989. SIGMA allowed the observations of the transition region between X-ray and gamma-ray astronomy, for the most part around 100 keV, with unparalleled angular resolution of the order of $10'$. It discovered 30 sources around the Galactic center, showing a great variety of systems with compact objects, most of which were black hole candidates.

The launch of the Compton Gamma-Ray Observatory (CGRO) in 1991 established gamma-ray astronomy as an important branch of astronomy and astrophysics in general. Thanks to its nine-year mission in orbit, gamma-ray astronomy has become an integral part of astronomy. The main instruments onboard the CGRO were the Energetic Gamma Ray Experiment Telescope (EGRET) for energies >30 MeV, the Compton Telescope (COMPTEL) for the energy range 1-30 MeV, the gamma-ray Burst and Transient Source Experiment (BATSE) and the Orientation Scintillation-Spectrometer Experiment (OSSE).

CGRO has expanded our knowledge on the different variety of sources that are present in the universe, such as the Sun, isolated spin-down pulsars, accreting binaries with stellar neutron stars and black holes, supernovae and supernova remnants, the interstellar medium, normal and radio galaxies, Seyfert galaxies, quasars and gamma-ray bursts. One of the highlights of the CGRO mission are the COMPTEL and EGRET all-sky maps of gamma-ray sources, which can viewed in Figure 1.3. The

COMPTEL and EGRET Gamma-Ray Sources

MeV < E < GeV
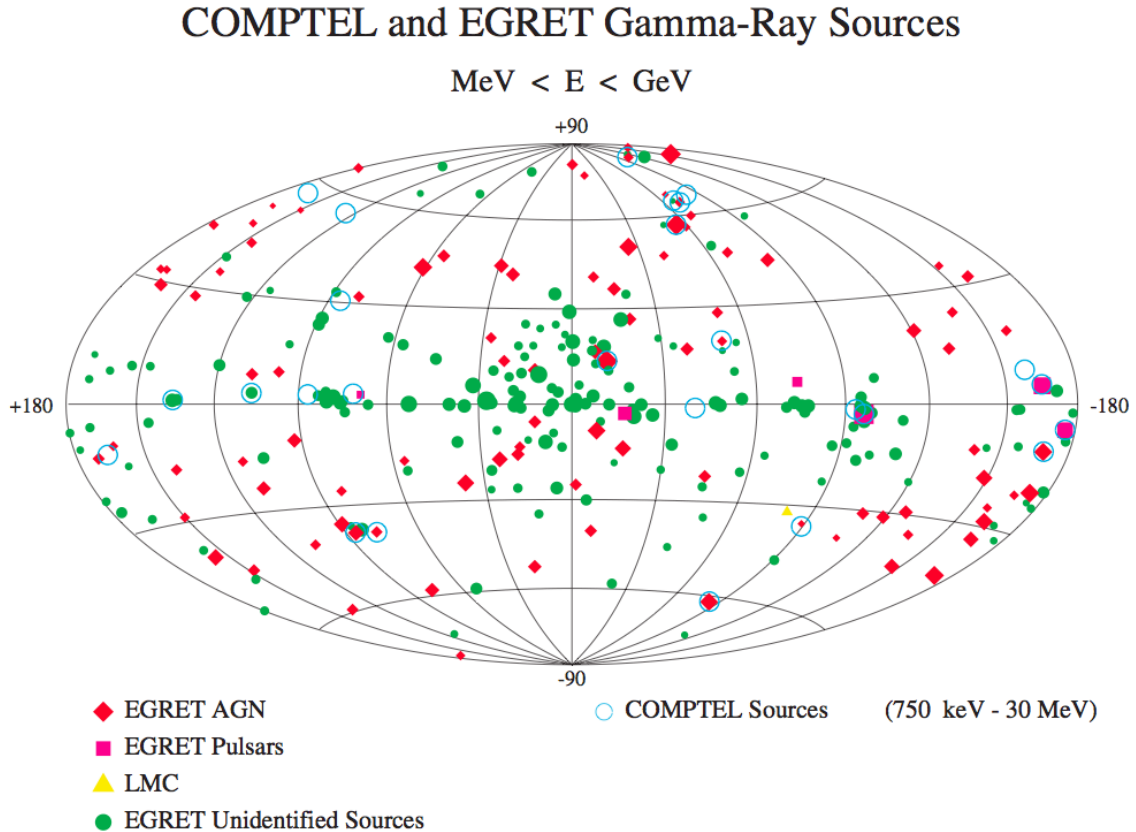
Figure 1.3.: COMPTEL & EGRET all-sky source maps [2].

figure contains over 300 sources, mostly from spin-down pulsars, X-ray accretion binaries and gamma-ray blazars. The other highlight from the galactic survey is the COMPTEL ^{26}Al all-sky map, which was the very first all-sky map of a radioactive gamma-ray line. Other gamma-ray lines from the radioactive isotopes (^{56}Co, ^{57}Co, ^{44}Ti) lines have been detected by OSSE and COMPTEL as well.

As for gamma-ray bursts, BATSE was able to measure the location, energy spectra and time profiles of more than 2500 single gamma-ray bursts. The real breakthrough though arrived in 1997, when the Italian/Dutch satellite Beppo/SAX made the discovery of the extragalactic origin of the bursts, after succeeding in observing the X-ray afterglows. The subsequent observations of these objects at optical wavelengths established the clear extragalactic origin of gamma-ray bursts. The gamma-ray energy

Figure 1.4.: Image of the Italian/Dutch satellite Beppo/SAX. Credit: Italian Space Agency (ASI) and BeppoSAX Science Data Center (SDC).

released from these sources is of the order of 10^{52} erg to several 10^{54} erg if the emission is isotropic. These values are comparable to the entire rest-mass energy of the Sun. This tremendous amount of energy could be released during the coalescence of compact objects or during the collapse of a massive star in the formation of a black hole [2].

1.1.2 Ground-Based Gamma-Ray Astronomy

In the early 1960s, it was suggested that gamma-ray particles of even higher energies than those visible by satellite could be revealed by ground-based air shower detectors [4]. The 1960s and 1970s marked the decades of the first ground-based atmospheric Cherenkov telescopes, when the techniques to distinguish gamma-ray showers from cosmic-ray initiated showers were first developed [5]. The Crab Nebula was one of the first sources to be proposed as a TeV gamma-ray source. The first purposed-built instrument for gamma-ray astronomy was the Whipple Observatory

Figure 1.5.: The very first TeV gamma-ray observatory in the United States was derived from World War II searchlight reflectors, which are visible in the picture on the left. The telescopes were manually operated by eye and were located at a dark site in Arizona south of Tucson, during the winter of 1967-1968. Just by chance, they were located exactly at the same place where the VERITAS telescope array is currently located [7].

10 meter gamma-ray telescope in Arizona, which saw its first light in 1968. The telescope operated for more than 40 years and would eventually make its major discovery with the detection of the Crab Nebula in 1989 [6].

To say that the road of ground-based gamma-ray astronomy was fraught with difficulties and efforts is to say the least. Many were the three sigma bumps along the way before a credible detection of a TeV source came into being. Before the Imaging Atmospheric Cherenkov Telescope (IACT) technique had reached its maturity, many of the early observations were concentrated on pulsars and binary systems, where it was hoped that the time variation of the observed events would eventually lead to a

true detection. Through phase folding of the data with the pulsar period from the radio and X-ray emission, a signal above the noise was expected to be produced against the large cosmic-ray background. Several initial low-significance TeV detections of the Crab pulsar were reported, which appeared in conflict with negative reports claiming only flux upper limits.

Of all the early marginal detections, the most controversial was the detection claim for TeV gamma-ray emission from Cygnus X-3, when the X-ray binary was in a state of radio outburst in 1973. Some claims of PeV emission of gamma-rays was also made around that time. The results also suggested that an atypical interaction at $\sim 10^{15}$ eV was taking place, which got the gamma-ray community excited and prompted further investigation. Observations of Cygnus X-3 and other X-ray binaries, such as Her X-1, Vela X-1, were undertaken by a number of groups at Durham University, the Whipple Observatory, the Haleakala Observatory in Hawaii and others. At this time, the spaced-based observations of Cygnus X-3 created some excitement as well, since SAS-2 claimed a periodic signal [8] but COS-B could not confirm it [9].

It was later recognized that even for the strongest gamma-ray sources, the cosmic-ray background events outnumber the gamma-ray events by a factor of $\sim 10^3$ or more. It was therefore clear that the sensitivity of the technique would need to be substantially improved by an efficient method of cosmic-ray background rejection. It was the idea initially proposed by Jelley and Porter, that would significantly boost the performance of the imaging atmospheric Cherenkov technique. Through an improved angular resolution of the telescope, they realized that the shape of the image of the Cherenkov light in the telescope cameras could be used as an effective and independent discriminant to reject cosmic-ray background events.

The detection of Cherenkov light from gamma-ray induced air showers in different projections allowed for a further improvement of the IACT technique. Although the problem of building stereoscopic Cherenkov telescopes was initially confronted by Grindlay and coworkers with two 7 m aperture reflectors in the mid-1970s, the full potential of the stereoscopic approach had been convincingly demonstrated two

decades later by the HEGRA system of imaging telescopes [10]. The HEGRA group built its first stereoscopic IACT telescope array consisting of five small-area 8.5 m^2 dishes at the Canary Islands in 1996. Prompted by the EGRET instrument results onboard the CGRO (launched in 1991), many other groups turned their instruments to the GeV sources that were being discovered. In 1992, IACT observations of the southern VHE sky began with the 3.8 m diameter, 220-pixel instrument constructed in Australia by the Japanese-Australian CANGAROO collaboration. At about the same time, several French groups formed the CAT Collaboration and constructed an IACT consisting of a 20 m^2 reflector with a 558-pixel camera. Located in Namibia, the Mark-6 IACT telescope of the Durham University group was built with a different design in mind. It had lower imaging capability but provided three independent samples and therefore was able to reach lower energy thresholds ($\lesssim$ 200 GeV).

1.2   Status of Major VHE Observatories

Currently, they are three major IACT observatories in the world. Beside the Very Energetic Radiation Imaging Telescope Array System, or simply VERITAS, which I will explain in great detail later, there are the High Energy Stereoscopic System (HESS) array in Namibia in southern Africa, which is designed and managed by the HESS Collaboration [11], and the Major Atmospheric Gamma-ray Imaging Cherenkov (MAGIC) array, run by the MAGIC Collaboration at Las Palmas, on the Canary Islands off the coast of Morocco [12].

1.2.1   HESS

Positioned in the Khomas Highland, Namibia at 1800 m above sea level, HESS is an array of four 13 m diameter imaging atmospheric Cherenkov telescopes that are sensitive to the faint flashes of Cherenkov light emitted in extensive air showers created by cosmic rays or gamma rays [11]. The telescopes are able to detect VHE gamma-rays in the energy range from 100 GeV to several tens of TeV, which positions
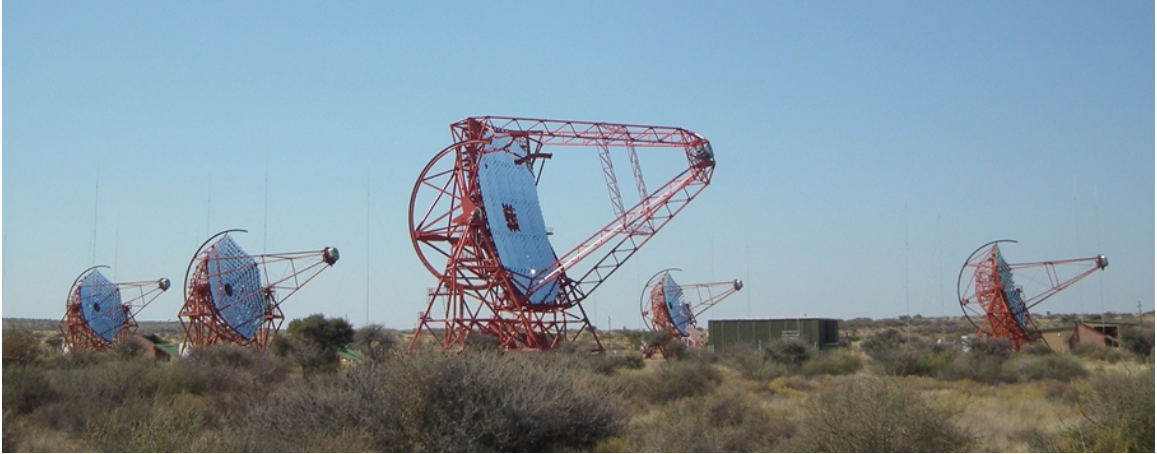
Figure 1.6.: Image of the High Energy Stereoscopic System telescope array in Namibia. Image courtesy of the HESS Collaboration.

its energy sensitivity close to that of VERITAS. HESS possess a total field of view of 5°. The angular resolution of the array system is $\lesssim$0.1°, with an average energy resolution of about 15%. HESS is able to detect point sources with a flux of 1% of the Crab nebula in a 25-hour exposure at the 5σ significance level, again similar to what VERITAS is currently capable of achieving.

The initial four HESS telescopes are arranged on a square with a 120 m side length. Each telescope camera contains 960 photomultiplier tubes (PMT), with each PMT being 29 mm in size and subtending a 0.16° angle. The main mirrors are segmented into 382 round mirror facets, each of which is 60 cm in diameter. The mirrors are made of aluminized glass with a quartz coating. The total mirror area is 108 m² per telescope. The mirror has a focal length of 15 m and a d/f ratio of 0.8. The mirror facets are arranged in a Davies-Cotton design (on a sphere of radius f). Mirror reflectivity is >80% (300 to 600 nm).

In the second phase of the project, an enormous single dish of 614 m² in mirror area (equivalent to a 28-m diameter circular dish) was added at the center of the array, increasing the energy coverage, sensitivity and angular resolution of the instrument. There are a total of 875 mirror facets of 90 cm each. The focal length of the central

Table 1.1: Characteristics of the HESS II Telescope

Mount	
Mount type	Alt-Az mount
Azimuth drive system	12 wheels in 6 bogies on 36 m diameter rail.
	4 wheels driven by servo motors, plus backup motors.
	Peak positioning speed 200°/minute.
	Range +/ 280° from park position.
Height of elevation axis	24 m
Elevation drive system	Toothed ring on either side of the dish.
	2 drive units with 2 servo motors each, plus backup motors.
	Peak positioning speed 100°/minute.
	Range 125° to +90° from vertical.
Dish	
Dimensions	32.6 m by 24.3 m, equivalent to 28 m circular dish.
Shape of reflector	Parabolic
Focal length	36 m
Total mirror area	614 m^2
Mirror facets	875 hexagonal facets of 90 cm (flat-to-flat) size,
	quartz-coated aluminized glass.
	Weight per facet ∼25 kg
Facet alignment	Each facet equipped with 2 actuators,
	with 2 μm positioning step size.
Focal plane instrumentation (Camera)	
Photo sensors	2048 1-1/4' photo multipliers
Packaging	128 drawers of 16 PMTs each, drawer includes digitization,
	trigger, slow control, high voltage generation.
Pixel size	42 mm (hexagonal, flat-to-flat), equivalent to 0.067°.
Sensitive area / field of view	∼200 cm in diameter, equivalent to 3.2° on the sky.
	1 GHz signal sampling using the SAM ASIC.
Signal recording	2 gain channels for each pixel for large dynamic range,
	records signal amplitude, timing, and shape.
Effective exposure time	16 ns
Image recording rate	3600 images/second
Power consumption	8 kW
Dimensions of camera body	227 cm wide × 240 cm high × 184 cm deep.
Camera weight	2.8 tons
Camera support	Quadrupod
Weight of complete telescope	580 tons (including mirrors & camera)

The data is from the public HESS web site (`http://www.mpi-hd.mpg.de/hfm/HESS/pages/press/2012/HESS_II_first_light/`).

Figure 1.7.: MAGIC IACT array at the Roque de los Muchachos site on the Canary island of La Palma. Image courtesy of the MAGIC Collaboration.

telescope is 36 m. The camera is composed of 2048 1-1/4' photo multipliers tubes, each 42 mm in size and subtending an angle equivalent to 0.067°. The Table 1.1 illustrates the characteristics of the central telescope of the HESS array system.

1.2.2 MAGIC

MAGIC is a system of two 17-m diameter Imaging Atmospheric Cherenkov Telescopes (IACT), for the observations of particle showers produced by very high energy (VHE, $\gtrsim$ 30 GeV) gamma-rays from galactic and extragalactic sources. The MAGIC site is positioned at an altitude around 2200 above sea level, at the Roque de los Muchachos site on the Canary island of La Palma, a volcanic island off the African coast at 28° N and 17° W. The site has excellent conditions for optical observations which makes it one of the best astronomical locations in the world.

Initially, MAGIC started operations in 2004 with a single, 234 m² reflective mirror (MAGIC-I). The construction and the commissioning of the second telescope, in the second phase of operations (MAGIC-II), finished in the Fall of 2009. Separated by 85 m, both telescopes operate in stereoscopic mode, where only events which trigger

both telescopes are recorded and analyzed. This permits the full three-dimensional reconstruction of the air showers, as seen by both telescopes. The precursor experiment of MAGIC-I was the HEGRA telescope, which used several telescopes of the same type but of smaller size [10].

Each MAGIC telescope is provided with a 3.5° diameter camera with photomultipliers (PMTs) as pixels. In the MAGIC-I camera, two types of pixels are used. The inner 397 PMTs have a diameter of 0.1°, while the 180 outer ones have a wider diameter (0.2°). On the other hand, the camera of MAGIC II consists of 1039 hexagonal pixels with a diameter of 0.1°. The current set of PMTs possess a quantum efficiency around 30%. This allows MAGIC-I to reach a threshold trigger energy of ∼50 GeV, and an analysis threshold of ∼70 GeV at small zenith angles, increasing the observations of sources with higher redshift than in the past [12]. More information on the performance of MAGIC can found on the MAGIC Collaboration web site[1].

Table 1.2: MAGIC Telescope Array Performance Numbers

Maximum trigger rate	>1kHz
Yearly duty time percentage	>90%
Average yearly duty time	∼1100 h
Average yearly duty time (with moonlight)	∼1400 h
Energy threshold at small zenith angle	∼50 GeV (trigger), ∼60 GeV (analyzed)
MAGIC-I sensitivity (at 5σ significance)	(0.76 ± 0.03)% Crab in 50 h (E >290 GeV)
Angular resolution	0.07° at ∼300 GeV
Energy resolution (from Crab analysis)	±22% (E >150 GeV)

Information from MAGIC web site at `https://wwwmagic.mpp.mpg.de/introduction/factsheet/`

1.2.3 VERITAS

The Very Energetic Radiation Imaging Telescope Array System (VERITAS) is a ground-based gamma-ray telescope array located at the Fred Lawrence Whipple Observatory (FLWO) in southern Arizona (31° 40′ N, 110° 57′ W, 1268 m a.s.l.). It

---

[1]`https://wwwmagic.mpp.mpg.de/`

Figure 1.8.: View of the FLWO base camp and the VERITAS array. Image courtesy of the VERITAS Collaboration.

consists of four 12-meter imaging atmospheric Cherenkov telescopes designed to detect the faint flashes of Cherenkov light from air showers initiated in the atmosphere by TeV gamma rays or cosmic rays. VERITAS is sensitive to gamma rays in the energy range from 85 GeV to 30 TeV (energy resolution: 15-25%), with a maximum effective area of approximately 10^5 m^2.

Each of the VERITAS telescopes is similar in design to the Whipple 10-meter Cherenkov telescope [13], originally situated in southern Arizona near Mt. Hopkins. The first VERITAS telescope became operational in early 2005, while the first stereoscopic-mode operations started in March 2006 with the construction of the second telescope. The third and fourth telescope were built in the winter of 2006, and the first scientific operations with the four VERITAS telescopes began in April of 2007.

In the summer of 2009, one of the four telescopes of the array was relocated to a different position, increasing the overall sensitivity of the array by about 30%. After the relocation, VERITAS is capable of detecting sources at the flux level of 1% of the Crab Nebula with a $\sim$25-hour exposure [15]. VERITAS has also been improved by the installation of an updated Level 2 trigger system (Summer 2011) and a new set of camera detector PMTs with higher quantum efficiencies (Summer 2012).
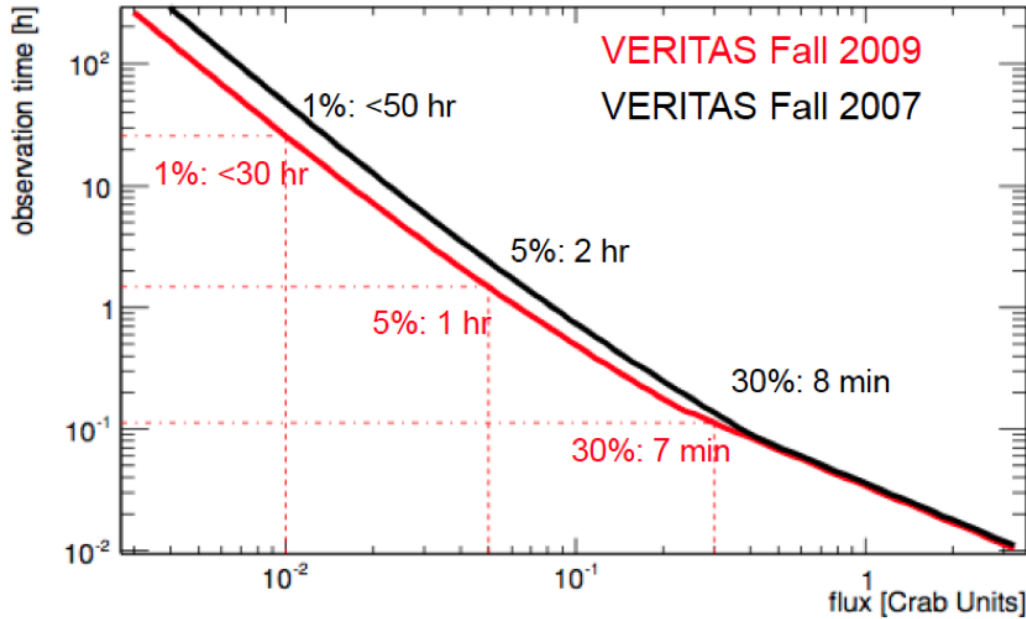
Figure 1.9.: Improvements in VERITAS sensitivity, from 2007 to 2009 [14].

Table 1.3: Current VERITAS Specifications

Energy range	85 GeV-30 TeV
Yearly duty time	>1000 h
Maximum effective area	$\sim 10^5$ m^2
Energy resolution	$\sim$15-25%.
Angular resolution (at 1 TeV)	$\lesssim 0.1°$ (68% containment level)
Pointing accuracy	$<50''$
Camera field of view (FoV)	3.5°
Sensitivity (at 5σ significance)	1% Crab in $\sim$25-h exposure

Information from the VERITAS public web site at `http://veritas.sao.arizona.edu/`
`about-veritas-mainmenu-81/veritas-specifications-mainmenu-111`.

Table 1.3 and Figure 1.9 respectively highlight the specifications and improvements in
the VERITAS telescope array system. More information about VERITAS can found
on the VERITAS Collaboration web site[2].

---

[2]`http://veritas.sao.arizona.edu/`

Figure 1.10.: A picture of myself at the command of the nightly observation shift. Photo by Mary Kertzman.

1.2.4   One Year in Arizona

At the beginning of my graduate work, I had the opportunity to work first hand at the VERITAS telescope array, which is situated just one hour's drive south of Tucson, AZ. The chance to work hands-on at the facility represented an opportunity I felt I couldn't just say no to.

During my stay, which lasted from August 2008 to July 2009, I learned about the VERITAS hardware, which mostly consisted in the trailer electronics and the mirror alignment system, which I had been heavily involved in. I was on a total of four observation shifts, and toward the end of my stay I was able to direct with confidence the observation session, a task which is usually conducted by the "czar", or the observation coordinator as they are called within VERITAS. I also provided my help for one of the major telescope facility upgrades, when Telescope 1 (T1) was

moved from its initial position on the east side of the base camp to the opposite side close to the entrance of the base camp. This was a feat that greatly improved the sensitivity of the telescope array.

My stay in Arizona is one I won't forget easily. What I like about Arizona and the US Southwest in general is the beautiful wildlife, which still retain to this day the imagery and fascination of the pristine lands of the Far West.

1.3 Radiative Emission & Absorption

Radiative emission from astrophysical objects that rely on relativistic electrons (or positrons) are called *leptonic*. The principle leptonic radiation mechanisms are *bremsstrahlung*, *synchrotron* and *inverse Comptonization* emission. A more detailed treatment of the radiation processes that occur in high energy astrophysics may be viewed in Rybicki & Lightman [16].

1.3.1 Bremsstrahlung

Radiation due to the acceleration of a charged particle in the electric field of another charged particle is called *bremsstrahlung* or *free-free emission*. Bremsstrahlung emission is known to occur for example in H II regions, which are regions of singularly ionized hydrogen, and in the hot gasses in the gravitational potential well of galaxy clusters. The general expression for bremsstrahlung is given by the formula

$$\frac{dW}{d\omega\,dV\,dt} = \frac{16\pi e^6}{3\sqrt{3}c^3m^2v}n_e n_i Z^2 g_{ff}(v,\omega),\tag{1.1}$$

where $g_{ff}(v,\omega)$ is a correction factor called the *Gaunt* factor, which for any regime (classical to quantum) can be applied to give the exact expression for bremsstrahlung emission. It is a function of the energy of the electron and its frequency of emission, and there are extensive tables of Gaunt factors in the literature. If we have a thermal distribution of electrons, then the Eq. 1.1 in CGS units assume the form

$$\epsilon_{ff} \equiv \frac{dW}{dV\,dt\,d\nu} = 6.8 \times 10^{-38} Z^2 n_e n_i T^{-1/2} e^{h\nu/kT}\bar{g}_{ff}.\tag{1.2}$$

where $\bar{g}_{ff}$ is the velocity-averaged Gaunt factor. Thermal bremsstrahlung will have a rather flat spectrum, to then cut off at the frequency where $h\nu \sim kT$, which derives from the Maxwellian shape for the velocity distribution [16]. The bremsstrahlung expression for non-thermal emission may be derived from the previous formula (1.2) with the knowledge of the appropriate velocity distributions and Gaunt factor corrections.

The frequency range of bremsstrahlung radiation depends on the amount of interaction between the electron trajectory and the positive ions. This depends on the relative velocities of the two bodies, which in turn depends on the temperature of the gas.

Bremsstrahlung is not a major process in VHE astrophysics, but relativistic bremsstrahlung from TeV electrons can be responsible for soft gamma-ray emission. Bremsstrahlung is an important physical process for atmospheric Cherenkov air showers (see Section 2.1).

1.3.2 Synchrotron Emission

Charged particles rotating in magnetic fields will radiate. In the non-relativistic case, the radiation is called *cyclotron* and the emission frequency is simply the gyration frequency of the particle in the magnetic field. In the relativistic case though, the emission frequency is more complex and can be several times greater than the gyration frequency. This case is known as *synchrotron* radiation. The total synchrotron emission per particle can be expressed by the formula

$$P = \frac{2}{3}r_0^2 c\beta_\perp^2 \gamma^2 B^2 \tag{1.3}$$

where r_0 is the gyration radius of the particle and $\beta_\perp$ is the perpendicular component of the velocity ($\beta \equiv v/c$) with respect to the magnetic field. For an isotropic distribution of velocities, and averaging over all angles, we can write the total radiated energy by synchrotron emission as

$$P = \frac{4}{3}\sigma_T c\beta^2 \gamma^2 U_B \tag{1.4}$$

where $\sigma_T = 8\pi r_0^2/3$ is the Thomson cross section, γ is the Lorentz factor and $U_B \equiv B^2/8\pi$ is the magnetic energy density.

There are some characteristics of synchrotron radiation worthy of notice. Due to the relativistic nature of the particles, most of the synchrotron emission will occur in a cone of angle $1/\gamma$ in the direction of motion of the particle ("beaming effect"). As seen by the observer, the synchrotron radiation is peaked at the critical frequency

$$\omega_c \equiv 3\gamma^2 qB \sin\vartheta/2mc, \tag{1.5}$$

where ϑ is the angle between the magnetic field B and the direction of the particle, and will fall off for higher frequencies. For a power-law distribution of electron energies of index p and for optically thin cases, the synchrotron spectrum also follows a power law of

$$F(\nu) \sim \nu^{-s} \tag{1.6}$$

where spectral index is $s = (p-1)/2$ [16].

Synchrotron radiation is the one of the primary non-thermal emission processes in astrophysics, responsible for emissions from the radio to the X rays, and plays an important role in TeV gamma-ray astrophysics through the *synchrotron self-Compton* process, or SSC process, which is also explained in a bit more detail below.

1.3.3   Compton Scattering

In the Compton scattering process, an high-energy photon interacts with a low-energy electron, which causes the decrease of the photon energy to the advantage of the electron energy. In the inverse Compton process, a low-energy photon gains energy from scattering off a relativistic electron. If $\epsilon_\gamma = h\nu$ is the energy of the photon, then the condition $\epsilon_\gamma \ll m_e c^2$ defines the *Thomson* or classical regime, and $\epsilon_\gamma \gg m_e c^2$ defines the *Klein-Nishina*, or relativistic regime.

In the non-relativistic regime, the cross section is given by the Thomson scattering cross section. For the relativistic regime, the cross section is given by the Klein-Nishina formula, which is inversely proportional to the photon energy ϵ_γ

$$\sigma_{KN} = \pi r_e^2 \frac{m_e c^2}{\epsilon_\gamma} \left[\ln \left(\frac{2\epsilon_\gamma}{m_e c^2} + \frac{1}{2} \right) \right]. \tag{1.7}$$

The principal effect of the relativistic regime on the electrons is to reduce the cross section, which causes the Compton scattering to become less efficient in the high energy regime.

For a population of relativistic electrons with Lorentz factor γ and power-law energy distribution of $N(E_e) \sim E_e^{-\alpha}$, the gamma-ray photons will have a characteristic energy of $\gamma^2 h\nu$ in the Thomson regime and energy of $\gamma h\nu$ in the Klein-Nishina regime. The energy spectrum of the gamma-ray photons is

$$N(\epsilon_\gamma) \sim \epsilon_\gamma^{-(\alpha+1)/2}. \tag{1.8}$$

The formula of the net power radiated from a single electron is given by

$$P_{comp} = \frac{dE_{rad}}{dt} = \sigma_T c \gamma^2 \beta^2 U_{ph} \tag{1.9}$$

where U_{ph} is the photon energy density, $\beta \equiv v/c$ [16].

In gamma-ray astronomy, inverse Comptonization is one of the main mechanisms of high energy and very high energy gamma-ray emission from a population of relativistic electrons. Relativistic electrons can be found in shocks within supernova remnants (SNR), AGN and microquasar jets, and pulsars. If a magnetic field is present, the electrons radiate photons through the synchrotron process, and some of these relativistic electrons impart a boost to the synchrotron photons by inverse Compton scattering. This is a well known radiation mechanism called the synchrotron self-Compton process and has been observed in many occasions in gamma-ray astronomy.

1.3.4 Pion Production & Decay

Astrophysical emission models that incorporate neutral pion decay as the source of gamma rays are referred to as *hadronic*. Pions are produced from the violent interactions between high energy protons and other high energy protons or nuclei. The decay process is shown in the reaction mechanism

$$p + p \rightarrow \pi^0 + X \rightarrow 2\gamma + X \tag{1.10}$$

where X represents other decay products of the interaction, mostly charged pions and neutrinos.

With a average lifetime of $\sim 8.3 \times 10^{-17}$ s, the neutral pions will quickly decay into a pair of gamma rays. The charged pions ($\pi^\pm$) will decay into charged muons ($\mu^\pm$), which will then in turn decay into an electron or a positron and relative neutrinos, according to the initial charge of the muon [17]. Consequently, pion decay has an important role in the study of VHE astrophysics and cosmic-ray physics. The presence of neutrinos, a product of the charged pion decay, could be used to distinguish hadronic models from leptonic ones.

1.3.5 Photon-Photon Pair Production

VHE gamma rays are energetic enough to produce $e^+ e^-$ pairs, by interaction with other ambient photons. The threshold for two photons to produce a pair, $\gamma + \gamma \rightarrow e^+ + e^-$, is given by the expression

$$\epsilon_* \epsilon_\gamma \gtrsim \frac{2m_e^2 c^4}{1 - \mu} \tag{1.11}$$

where ϵ_* and ϵ_γ represent the energies of the two photons, and where the threshold and cross-section depend on the incident angle φ between the photons ($\mu = \cos\varphi$, with $\varphi = \pi$ for head-on collisions) [18].

In the case of the dense photon fields in binary systems, absorption can play a major role in the outcome of the gamma-ray processes. Photons in the energy range

0.1-1 TeV are most likely to scatter off photons with wavelengths in the UV/optical and IR ranges. If we take the example of the gamma-ray binary LS 5039, the typical energy of the stellar photon is $\epsilon_* \approx 2.7$ kT ≈ 9 eV, so the threshold for pair production for head-on interactions is $\epsilon_\gamma \approx 30$ GeV. This is the cutoff expected from pair production in LS 5039.

2. The Atmospheric Cherenkov Technique & VERITAS Observatory

2.1 Physics of Extended Air Showers

The main interaction of a primary gamma ray above 10 MeV with matter of the air medium is through electron-positron pair production in the presence of an ion or proton N,

$$\gamma + N \rightarrow e^- + e^+ + N \tag{2.1}$$

where the ion or proton is required for conservation of momentum, since the interaction cannot take place in empty space. The resulting electron-positron pair further interact with the medium nuclei through pair production and bremsstrahlung, producing more gamma rays while the energy of the pair is reduced by $1/e$ per radiation length. This process continues, producing an extensive air shower, until the average energy of the particle in the shower fall below the energy required for bremsstrahlung (~ 83 MeV). After this point, the dissipative processes become ionization and Compton scattering. As a consequence of the low transverse momentum of the primary gamma ray, the shower is strongly concentrated along the initial direction of the primary gamma-ray photon. From the point of first interaction until the point where the energy of the electron falls below ~ 21 MeV, the shower will produce Cherenkov radiation, by which the presence of the primary gamma ray can be inferred.

Cosmic rays produce air showers as well. If the primary cosmic ray possesses an energy greater than ~ 1 GeV, charged and neutral pions are produced until the

Development of gamma–ray air showers
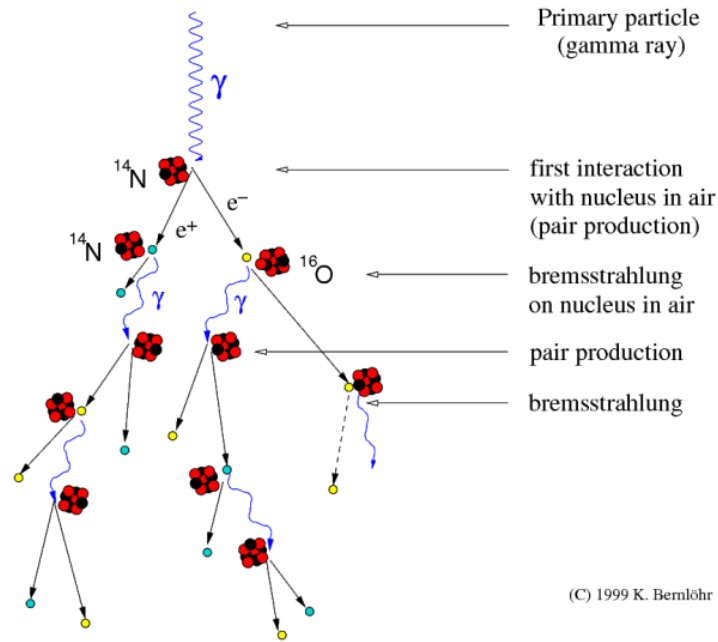
Figure 2.1.: Gamma-ray initiated air shower. Image courtesy of Konrad Bernlöhr.

energy drops below this threshold. Neutral pions decay almost instantly into gamma rays, while the charged pions decay into muons according to the decay reaction

$$\pi^0 \rightarrow 2\gamma \qquad \tau \sim 8.3 \times 10^{-17}\,\text{s} \tag{2.1a}$$

$$\pi^+ \rightarrow \mu^+ + \nu_\mu \qquad \tau \sim 2.6 \times 10^{-8}\,\text{s} \tag{2.1b}$$

$$\pi^- \rightarrow \mu^- + \bar\nu_\mu \qquad \tau \sim 2.6 \times 10^{-8}\,\text{s.} \tag{2.1c}$$

The muons, due to their relatively long lifetime, reach the surface of the Earth before decaying, according to the decay mechanism

$$\mu^+ \rightarrow \; e^+ + \bar\nu_\mu + \nu_e \tag{2.1d}$$

$$\mu^- \rightarrow \; e^- + \nu_\mu + \bar\nu_e. \tag{2.1e}$$

Cosmic-ray air showers possess greater lateral spread, due to the greater transverse momentum imparted to the pions compared to the electron-positron pair from a gamma ray.

Cosmic-ray initiated showers tend to generate less Cherenkov light compared to a gamma-ray air shower, since most of the energy of the primary cosmic ray goes into the hadronic and muons components, which are heavier than electrons and carry most of the energy but radiated little Cherenkov light. In a gamma-ray initiated air shower, all of the energy goes into the secondary electron-positron pairs which produce Cherenkov light. In addition, cosmic-ray showers produce neutrinos which don't produce any Cherenkov light. These feature are extensively used to distinguish cosmic-ray initiated air showers from gamma-ray initiated air showers.

2.1.1 Cherenkov Radiation

When a charged particle travels in a dielectric medium at a velocity greater than the speed of light in that medium, the medium emits a radiation known as *Cherenkov radiation*. This is caused by the polarized electromagnetic emission produced by the oscillations of the medium by the relativistic particle. The electromagnetic radiation interferes constructively for the relativistic speeds of the particle, causing a coherent radiation to be emitted at an angle ϑ_c to the trajectory of the particle. This angle is given by the formula

$$\cos \vartheta_c = \frac{1}{n\beta} \tag{2.2}$$

where n is the refractive index of the medium. ϑ_c is called the Cherenkov angle of the medium. This is maximum for $\beta \equiv v/c = 1$

$$\vartheta_{max} = \cos^{-1} \frac{1}{n}. \tag{2.3}$$

In the case of a gamma-ray initiated shower, with a refractive index of 1.0003 at sea level, the opening angle of the Cherenkov cone is $\sim 1.4°$. At higher altitudes, due to the lower refraction index, the opening angle is smaller, and increases as the shower progress downwards. The number of Cherenkov photons emitted per unit length dx and per wavelength interval $d\lambda$ by a charged particle Ze is given by

$$\frac{d^2N}{dxd\lambda} = \frac{2\pi\alpha Z^2}{\lambda^2} \left(1 - \frac{1}{\beta^2 n^2(\lambda)}\right) \tag{2.4}$$

where α is the fine structure constant and $n(\lambda)$ is the wavelength-dependent refraction index. From this last, one can see that the number of Cherenkov photons emitted is proportional to $1/\lambda^2$. The bulk of the Cherenkov emission generated in the atmosphere occurs in the UV and blue parts of the electromagnetic spectrum. The photomultiplier tube (PMT) in the cameras of each telescope are designed to possess maximum quantum efficiency for the UV and blue parts of the spectrum.

2.1.2   Imaging Atmospheric Cherenkov Technique

The Cherenkov technique basically consists in taking a snapshot of the Cherenkov light with a high resolution camera at the focus of the telescope cameras. Its application to gamma-ray astronomy was first proposed in 1963 by Jelley and Porter [19], but the first true detection of a gamma-ray source was accomplished by the Whipple Collaboration in 1989 [6], with the perfection of the Cherenkov Imaging Technique (Figure 2.2).

There are key specifications to the detection of gamma-ray sources with the imaging technique. The detector must be placed at high altitudes where the most of Cherenkov light is emitted. Due to the low photon intensity of the Cherenkov light cone, which is ~ 50 ph m^{-2} within the 100 m shower cone for a 1 TeV primary gamma ray, the detector must have a large collection area to grab the highest amount of Cherenkov photons. A high resolution of the shower event is given by the use of a large amount of PMTs in the camera, which also guarantees an ample field of view to catch the angular extent of the shower event ($\sim 1°$).

One of the main factors that needs to be considered is the subtraction of the night sky background from the Cherenkov light. The Cherenkov light duration is on the order of nanoseconds, and the integration time of the detector must match the length of the Cherenkov light flash. Multiple coincident detections of light pulses in the same camera or in different cameras can enable the rejection of fluctuations due to the night sky background or to local muons. Lastly, the total Cherenkov light intensity is a
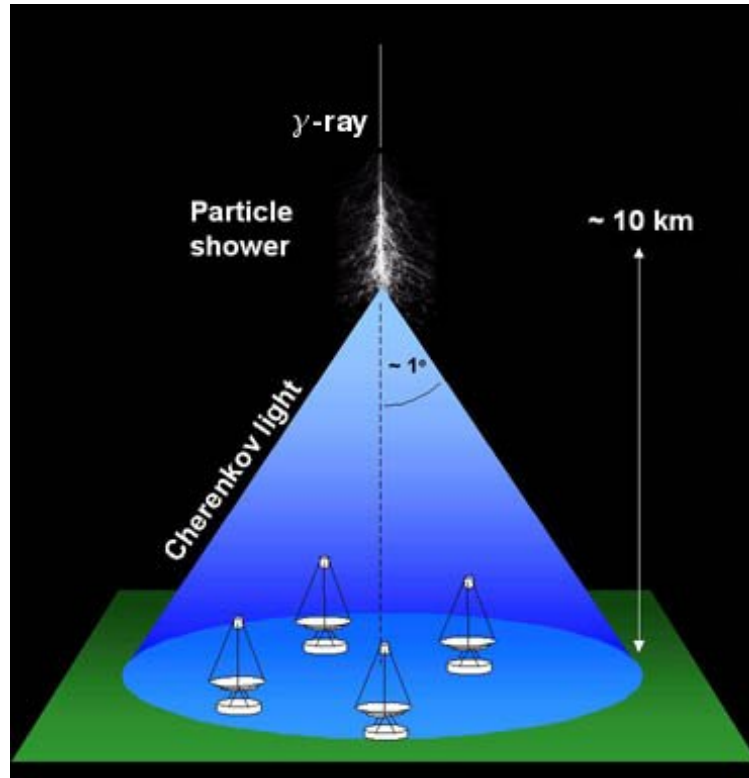
Figure 2.2.: Diagram showing the particle shower light cone compared to the Cherenkov telescope array. The shower starts at ∼10 km in altitude, and produces a light cone that reaches a diameter of ∼125 meters by the time it touches the ground. Credit: H.E.S.S.

calorimetric measure of the primary gamma-ray photon, allowing to reconstruct the energy of the primary gamma-ray photon from the total energy of the light cone.

Once we can remove the light caused by the night sky background, the biggest challenge is to detect gamma-ray induced shower from the much larger background of cosmic rays air showers. For gamma-ray air showers, the Cherenkov light of the shower axis is emitted along a small cone. The shower core, the point where the air shower hits the ground, is usually at a large distance from the detector, and this is projected in the camera as an ellipse. The shape and orientation of these ellipses in the focal plane of the camera are different for gamma-ray and cosmic-ray air showers. Cosmic rays are isotropic in origin and don't have a preferred direction in the camera.
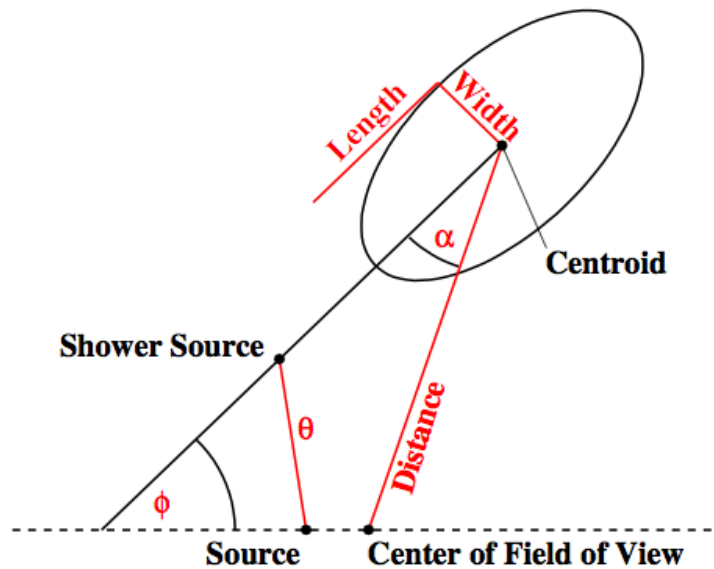
Figure 2.3.: The six Hillas parameters: α, distance, length, width, centroid & size [22].

On the other hand, since the telescope can be pointed in the direction of a gamma-ray source, gamma-ray ellipses are oriented towards the center of the field of view. Due to the narrower spread of the light cone, the ellipses tend to be narrower and more elongated in the camera compared to the cosmic-ray showers. The gamma-ray images also tend to be more symmetric around the projection of the shower axis in the camera. Even with this simple scheme, one can remove 99.9% of the background cosmic rays while retaining more than a third of the gamma-ray events.

Hillas devised the first method of moment-based analysis to fit the image of a shower with a set of six specific parameters. From the Figure 2.3, these parameters are α, distance, length, width, centroid and size [20]. A full description of the Hillas technique can be found in [21]. These parameters are a reflection of the physical attributes of the gamma-ray shower over the cosmic-ray shower. Through simulations of gamma-ray and cosmic-ray air showers, one can define regions of the parameter space where gamma-ray events are more abundant. After the application of event selection criteria that retain gamma-ray events over cosmic-ray events, the incident

direction of candidate gamma-ray events can be determined from shower alignment. The energy of primary gamma-ray photon can be inferred using look-up tables created by simulations which are based on the impact distance and size parameter of the event. This method has acquired a noteworthy boost with the advent of multiple Cherenkov telescope arrays. Stereoscopic observations allow for a much improved reconstruction of the shower parameters, which allows for a much better determination of the core position of the shower axis. Stereoscopic observations consequently also gives a greater improvement in the angular resolution of the camera detector. A second advantage is also given by the extra trigger level requirement of coincident detection by multiple telescope of the shower event, which can be done by hardware and enables the detector to be more sensitive at the lower energies.

2.2 VERITAS Telescope Array

In this section, I will explain in detail the VERITAS instrument, starting from the mechanical and optical components of the telescope, the camera components, the trigger hardware components and then finishing with the details of the data analysis procedure.

2.2.1 Optics & Camera

The mechanical structure of the VERITAS telescopes consists of a steel-frame optical support structure (OSS) on a commercial altitude-azimuth positioner. The positioner is capable of a pointing accuracy of $<50''$. The Davies-Cotton optical design [23] is employed on the OSS over other configurations, due to the advantage of the use of segmented mirrors, each spherical and identical, which are easy to fabricate, mount and align. The design allows for small off-axis aberrations, giving good image quality within a few degrees from the optical axis. The only drawback of the design is that the flux introduces a time spread in the Cherenkov pulse, which is kept low by the use of a low f-number. The f-number in optics is the ratio of the diameter of

the optical system to its focal length, which in the case for VERITAS was chosen to be f/1.0.

Each telescope is composed of 345 separate hexagonal mirror facets covering an area of about 110 m². Each mirror has curvature radius of 24 m $\pm$ 1%, and are set out on a 12-m radius spherical surface of the OSS, by means of a triangular frame which isolates the mirror facets from the OSS flexing during telescope operations. The mirrors are optimized to reflect the most at the typical wavelengths of the Cherenkov light pulses ($\sim$320 nm). More details of the mirror facets can be found in [24].

The mirrors on the OSS can be adjusted to permit optimal mirror alignment. The alignment of each individual mirror is an important factor that effects the point spread function (PSF) of the telescopes. Using raster scans across a bright point source, a system was devised to check for the alignment of each mirror facet. Using a star which can be considered as a point source at an infinite distance, a CCD camera placed at the focal point measures the light from each facet during the scan, and can provide a measure of the mirror misalignment. Each mirror can then be corrected for misalignment by moving the mounting screws on the individual facet [25].

The VERITAS cameras are positioned at the focal plane of each telescope at a distance of 12 m from the mirrors, and are supported by four steel beams from the OSS. Each camera has a field of view of 3.5° and contains 499 photomultiplier tube (PMTs), which serve effectively as pixels in the camera, and are arranged in a hexagonal grid to minimize the spacing between them. The angular resolution of the camera is <0.1°, at 68% containment. The main characteristic of the PMTs is that they are capable of providing fast reaction times and high gains to capture the quick Cherenkov light pulses from the air showers. The size of the PMTs in the camera plane corresponds to an angular distance of 0.15° between PMT centers. Each PMT is connected to a high voltage supply and to a preamplifier to amplify the signal from the last anode before reaching the trigger electronics. A plate of hexagonal Winston light cones is situated on top of the PMTs to focus the Cherenkov light pulses towards the more sensitive areas of the PMTs. The light cones remove the dead space between
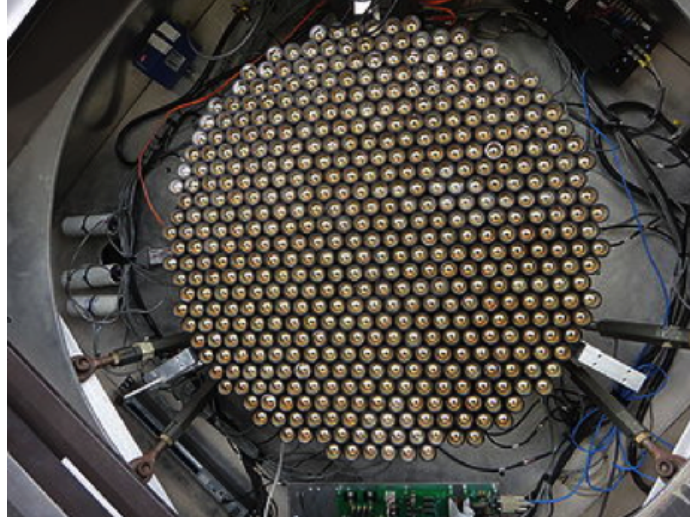
Figure 2.4.: VERITAS camera with the improved high-QE pixels, after the 2011 upgrade [26].

PMTs and protect the PMTs from the ambient background light, by limiting the acceptance cone just to solid angle subtended by the telescope mirror.

In the summer of 2012, the VERITAS Collaboration replaced the old Photonis XP2970 PMTs of each telescope camera with new super-bialkali Hamamatsu R10560-100-20 PMTs. The new PMTs are characterized by a higher quantum efficiency (QE) of 32%-34%, compared to the QE of 18%-22% for the previous PMTs. The quantum efficiency is the measure of the probability that a photo-electron will be emitted if the photo-cathode is hit by a photon. The PMTs have demonstrated a 35-50% increase in photon sensitivity compared to the previous ones used in VERITAS, permitting an increase in the VERITAS effective area at low energies. More details on the PMT upgrade can be found at [14].

Each PMT is connected to a high voltage power supply which controls the voltage by means of a control program through an Ethernet interface. The voltages may be set manually, but are usually preset from the values in the VERITAS database. The gain of a PMT is given by the ratio of the anode current to the cathode current. VERITAS operates with a nominal gain of 2×10^5. The procedure of flat-fielding
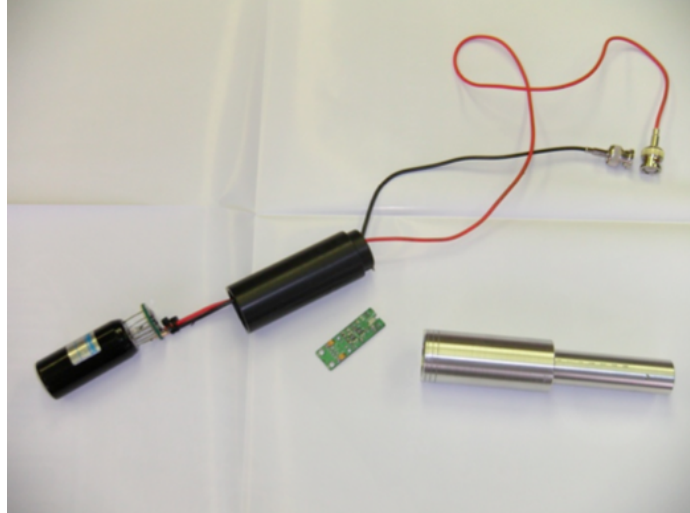
Figure 2.5.: VERITAS high-QE PMT components. From left to right: Hamamatsu R10560-100-20 High QE PMT, Delrin mounting tube, preamplifier and aluminum mounting tube [14].

assures that every PMT operates at the same nominal gain, to make sure that each PMT has the same weight in the camera when triggering on the events. The rise time (10%-90%) of the PMTs is currently set at 1.7 ns.

Excessive currents can degrade the operation lifetime in the PMTs. For the preservation of the PMTs, the HV control program monitors the anode currents during data operations, and suppresses the high voltage in the PMT in case the current surpasses the threshold limit. This can occur for bright stars in the PMT field of view, or by accidental human intervention, for example by flashlights or headlights from cars at the base camp.

A preamplifier is located at the base of each PMT, to boost the anode signal before it is sent out to the data acquisition (DAQ) system. Bias currents from the night sky background are removed in the preamplifier through an AC coupling with the PMT signals. The preamplifier has a large 300 MHz bandwidth, in order to accommodate for the fast rise times of the Cherenkov pulses.
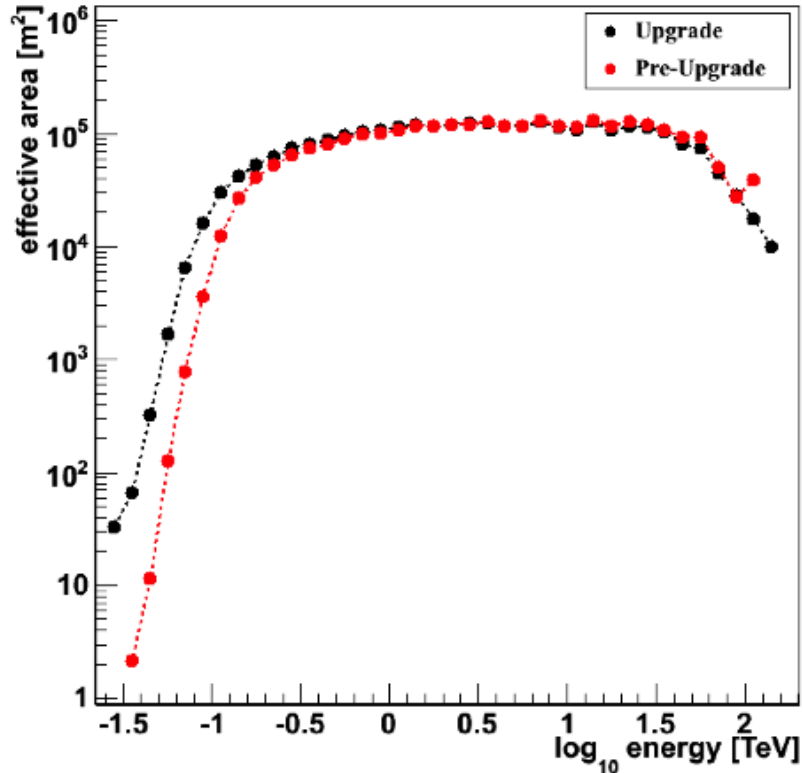
Figure 2.6.: Comparison of the simulated VERITAS effective area to primary gamma-ray energy, before (red dots) and after (black dots) upgrade, for soft cuts [26].

2.2.2 Trigger

The trigger system is a hardware mechanism that discerns with high efficiency candidate gamma-ray events from the random night sky noise. Selecting possible gamma-ray event at the hardware level is important, since the main limitation of the data acquisition system is that it is incapable of recording events while it is in the process of saving the previous events. To keep the data acquisition dead time as low as possible and to keep the trigger rates at acceptable levels, a three trigger system was devised for the VERITAS telescope array. The trigger system operates on the level of the single pixel (L1), on three adjacent pixels of the same telescope (L2) and within at least three telescopes in the four-telescope array (L3).
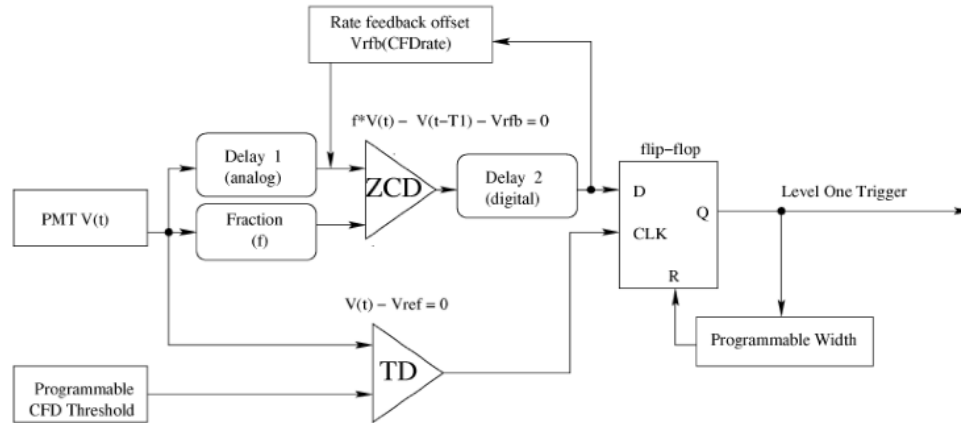
Figure 2.7.: Block diagram of the VERITAS CFD circuit for the L1 trigger [27].

The first level trigger works on the level of the single pixel, and is fed into the constant fraction discriminator (CFD) by splitting the input signal into three components. The first component is delivered to a simple threshold discriminator (TD) which generates a trigger signal if the programmable threshold level is reached. The second signal component is inverted, delayed and fed to the zero-crossing discriminator (ZCD), while the third component is attenuated and also passed to the ZCD. The ZCD sums the two pulses and determines the CFD trigger time as the point of zero crossing where the two signal cancel each other. The ZCD output is forwarded to the flip-flop with the output of the TD which is then routed to the L2 trigger [27]. With the CFD, the timing of the output logic pulses can be determine with good precision, which helps reduce the coincidence time of the L2 trigger and consequently lower the energy threshold. The timing resolution can be deteriorated by the jitter in the arrival time of the trigger, which is caused by noise on the ZCD. This can be solved by adding a small DC offset to the ZCD, but since most of the noise comes from the night sky background, which can change back a factor of four, this is not a desirable solution. The solution consists in the addition of a circuit within the CFD, called a rate feedback loop (RFB), which dynamically adjusts the ZCD offset when
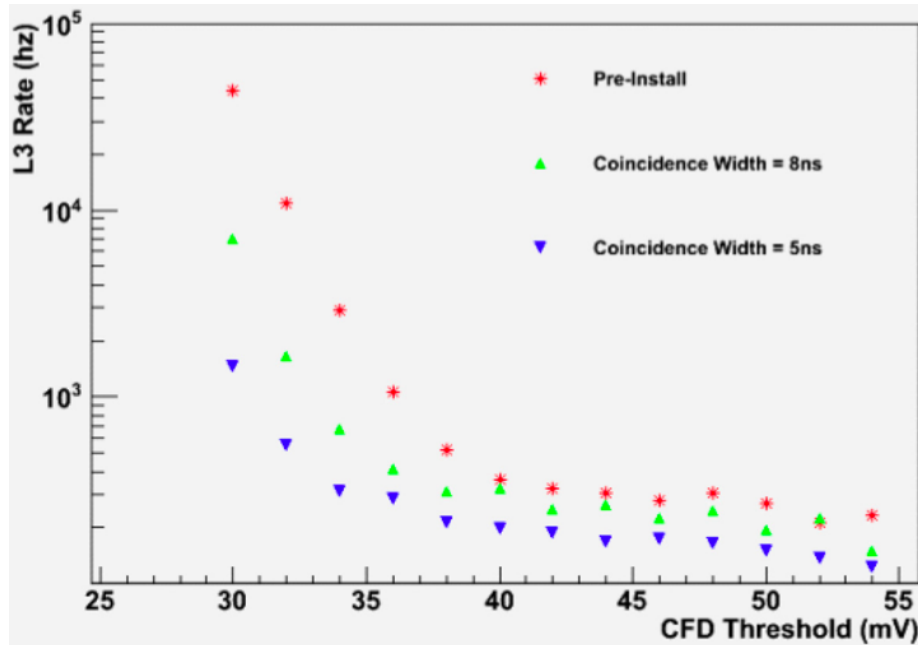
Figure 2.8.: Bias curve from one of the VERITAS telescopes with the original trigger and with the new trigger at the two different coincidence width settings of 5 ns and 8 ns [29].

the noise level rises. The VERITAS CFDs normally operate at a 50 mV threshold and an output signal width of 10-12 ns.

The second level (L2) of the VERITAS trigger functions on the output of the L1 triggers from each pixel. In the summer of 2011, the L2 trigger system on VER-ITAS was upgraded to a new FPGA-based pattern trigger system. The system is programmed to discern gamma-ray like events from patterns of the L1 trigger when three adjacent pixels within the camera are triggered, within a coincident time window that is set to 5 ns [28]. This can be done since gamma-ray air showers tend to be more compact, while by contrast pulses caused by the night sky background tend to be confined to one or two pixels. The Level 1.5 boards in the L2 trigger system perform the pattern recognition processing of the pixels in each individual telescope. If a pattern is found that matches a pattern in memory, a telescope level (L2) trigger is sent to the telescope array level 3 (L3) trigger [29].

The last trigger level (L3) operates on the level of the telescope array, which consists in the simultaneous observation of an air shower by multiple telescopes. Cherenkov light from muons, at low energies and for large impact parameters at the telescope, dominate the background and produce patterns in the telescope camera which are hard to distinguish from the images created by VHE gamma-ray air showers. In general though, the Cherenkov light from local muons will only effect an area large enough to trigger a single telescope, therefore an array of telescopes with a coincidence trigger can effectively remove the local muons from the data pipeline. This greatly reduces the energy threshold of the array and substantially increases its sensitivity.

The heart of the L3 hardware is composed of two custom-built VME modules, the Pulse Delay Module (PDM), the Sub-Array Trigger (SAT) board and a commercial GPS clock. The PDM is responsible for the addition of a constant time delay to the L2 signals, due to the telescope position in the array. The PDM is also in charge of the calculation of the second component of the time delay which is caused by the arrival times of the Cherenkov wavefront on each single telescope, which change as the telescope follows a source on the sky. These time delay are calculated from the current telescope pointing and updated every 5 seconds for the L3 trigger calculation. The SAT module is responsible in determining whether an array trigger condition occurs within a certain coincidence time window ($\sim$50 ns) for the delay-adjusted L2 signals [28]. If the condition is met, the SAT issues a command to the data acquisition system to record the event. The SAT also stops for 10 μs after an event decision, to allow the L3 signal propagation to the telescopes. The dead time occurs during read out of the L3 triggered events, and scales linearly with the array trigger rate, reaching $\sim$6-8% at 150-170 Hz and 10-11% at 225 Hz [30].

2.2.3   Data Acquisition

The VERITAS data acquisition (DAQ) system is divided into three levels, the VME crate DAQ, the telescope DAQ and the array DAQ. Each crate is a hardware

container with the electronic modules specific to a certain function for each telescope. The DAQ system is devised to merge events from the pixels at the telescope level into data events on the array level, which are then stored in the archive system. The PMT signals are directed into the FADC boards in each telescope, where they are sampled every 2 ns (for a total of 24 samples) by a 500 MHz flash analog-to-digital converter (FADC) and stored in a 64 μs deep memory buffer.

The acquisition of the FADC traces is managed by the VHE data acquisition system (VDAQ). The VDAQ serves as an interface between crates responsible for the digitalization of pulses in the FADCs and the event builder system that merges the event fragments from the other VME crates. When the L3 array trigger identifies an air shower event, each FADC channel is directed to read out a portion of the buffer relevant to the event. During readout, the VHE crates that manage the FADCs send a BUSY flag that prevents further L3 triggers until the event is read out. The clocking for event readout is managed by clock trigger boards (CTBs) on the VHE crates that manage the FADCs, and by a master CTB and GPS clock that are handled by an auxiliary crate. This permits the synchronization of the time stamps on events over the entire system, together with the record of the unique event number and trigger type of each event.

The event fragments are passed from the crates of the VME DAQ to the Event Builder to assemble the fragments into telescope-level events, and then at this point the data is written to the local disk and sent to the array DAQ program, the Harvester. The Harvester is responsible for the array-level data acquisition. It performs a number of real-time sanity checks to assure all of the telescopes are read out according to the array-trigger information. The Harvester then saves the data in the VERITAS custom format called VERITAS Bank Format (VBF), which has been designed for high read-write performance, portability, compactness and extensibility.
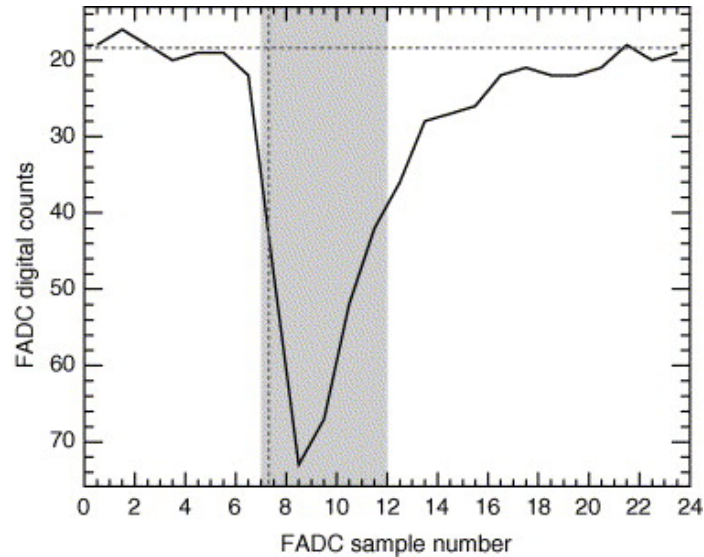
Figure 2.9.: Amplitude of the signal pulse in digital counts versus sample number for the FADC trace in the PMT. The vertical dashed line represents the T_0 and the horizontal dashed line represents the pedestal contribution to the PMT signal pulse [31].

2.3   VERITAS Data Analysis

This section describes the steps of TeV gamma-ray data analysis with the VEritas Gamma-ray Analysis Suite (VEGAS), one of the main data analysis packages used in VERITAS [32]. The first step of the analysis, done in VEGAS stage 1, consists in the calibration calculations, which removes all hardware dependencies from the measured values. Stage 2 of VEGAS is in charge of using the calibration calculations on the raw data to remove as much of the hardware dependencies as possible from further analysis. This stage also takes care of the parameterization of the air shower images and passes the results further down the analysis chain. Stage 4.2 is responsible for the reconstruction of the shower parameters that created the images and for the estimation of the qualities of the primary initiator of those air showers. Stage 5 allows for the application of cuts to remove as many cosmic rays as possible. Stage

6 finally produces the higher-level results, such as source detection, spectral analysis and timing analysis, once the background subtraction is performed on the data.

2.3.1 Data Format

The VERITAS data is conserved in a custom format, the *VERITAS Bank Format* (VBF), which contains all data of the Cherenkov air shower in an *array event* framework. The framework consists of an *array trigger*, which contains top-level information such as the event number, the GPS time of arrival and type of trigger, and of a *telescope event* which retains the actual data from the telescope.

2.3.2 Calibration

The calibration procedure is the first step in the VERITAS data analysis. It consists in the removal of all hardware dependencies from the data. The main calibration parameters are the pedestal level contributions on each PMT from the night sky background, the time adjustments introduced by the hardware on the signal from each PMT and the gain of each channel from the conversion of the photo-electrons to charge.

The night sky background is responsible for a significant positive or negative fluctuation to the actual Cherenkov signal registered by the PMT. Since the FADC records only signals of positive polarity, a negative offset, known as the *pedestal*, is added to the FADC sample, before being digitized. In order to calculate the value of the charge in the PMT solely due to the Cherenkov light, the mean pedestal and the fluctuation around the mean, also called *pedvar*, are calculated by introducing an artificial trigger rate of 1-3 Hz during observations, to provide a measurement of the light in the PMT due to the night sky background. During the first step of the data analysis, these pedestal events are used to determine the mean charge and the width of the distribution for the night sky background.

The arrival time of the signal on a pixel T_0 is defined as the time on the rising edge of the pulse at which the pulse reaches half of its peak value with respect to the pedestal (see Figure 2.7). T_0 depends not solely on the gradient from the inclination of the Cherenkov wavefront to the telescope array, but also on the differences in cable lengths and delays introduced by the HV and electronics between the FADC and the PMT channels. Distinct *flasher* runs are taken every night which simultaneously illuminate the telescope to assess the time differences, called T_{offset}, and are also used to evaluate any variation of the gain on the PMTs. The T_{offset} is defined as the average difference between the start time of the pulse T_0 in a single channel and the start time of the event T_{event} over M events

$$T_{offset} = \frac{1}{M} \sum_{i=1}^{M} (T_{0,i} - T_{event,i}),$$ (2.5)

where T_{event} is defined as as the average arrival time of the signal over all of the N camera pixels

$$T_{event} = \frac{1}{N} \sum_{j=1}^{N} T_{0,j}.$$ (2.6)

The T_{offset} are then removed in the data analysis from the arrival time of the signal at each channel to recover the actual arrival time of the Cherenkov light pulse.

The amount of charge in the FADC trace from each camera pixel is directly proportional to the number of photons detected, and ideally for equal amounts of light intensity the PMTs produce the same amount of charge relative to the other PMTs. The aging of the PMTs though tend to transform the charge response, so to correct for this the PMT voltages are adjusted seasonally to modify the gain so that equal amounts of photons produce a proportional amount of charge. The effect is also corrected on a nightly bases by the flasher runs, which illuminate the camera pixels with the same light intensity to gauge the response. Currently with the upgraded camera PMTs, one FADC digital count (d.c.) corresponds to roughly 5-6 photo-electrons.

This part of the analysis is also responsible for removing from the data chain pixels that do not have meaningful traces or a reasonable amount of charge. These
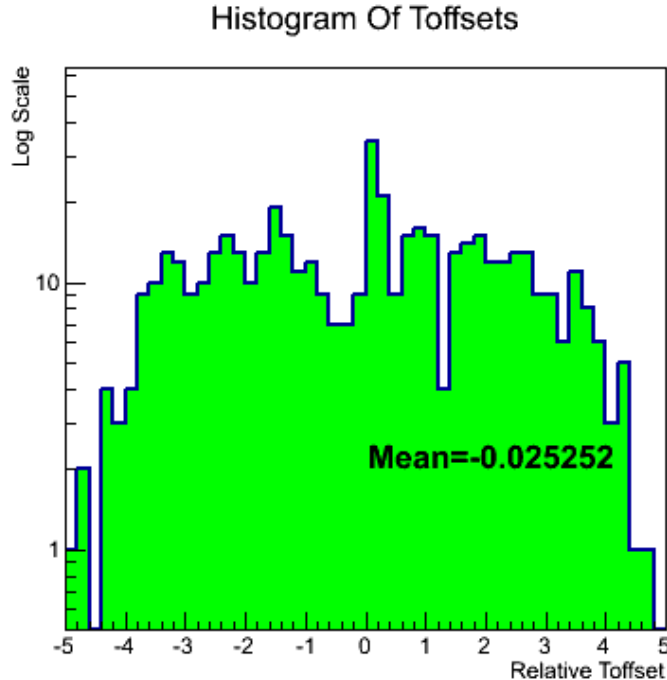
Figure 2.10.: Distribution of the T_{offset} in a single telescope.

channel can be recognized by the distribution of signals recorded during the run, and are removed before the reconstruction of the shower image in the camera. The criterion used to distinguish these anomalous pixels is given by the quantity called *scaled pedvar*,

$$scaled \ pedvar = \frac{pedvar - \langle pedvar \rangle}{\sigma_{pedvar}} \qquad (2.7)$$

where $\langle pedvar \rangle$ is the mean pedvar measurement and σ_{pedvar} is the statistical error on the pedvar distribution. The outliers this way can be visualized in a convenient way with a scale that is independent of the mean.

2.3.3 Image Parametrization

At this point, once the signals have been identified, the shower images from the Cherenkov light pulses are parametrized by calculating the moments of light distributions through a technique first proposed by Hillas [20]. The images themselves are
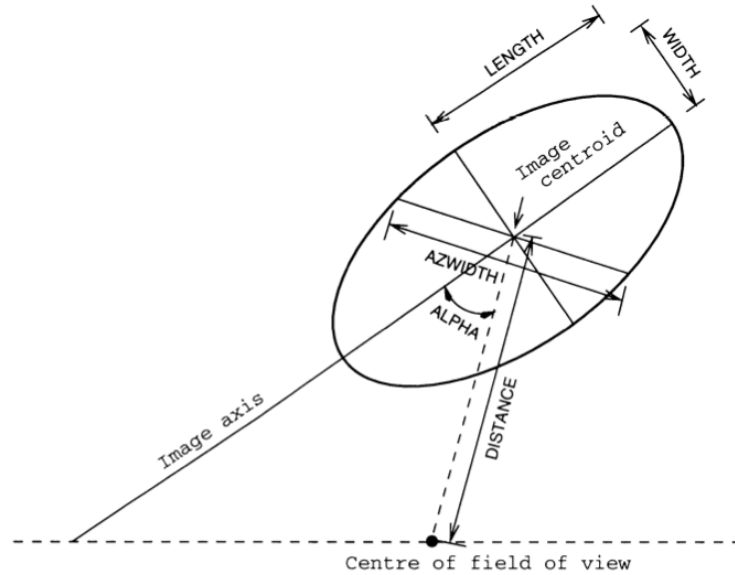
Figure 2.11.: A visual representation of the Hillas parameters from [33], as described in Table 2.1.

singled out through a cleaning procedure. First of all, pixels containing an integrated charge greater than 5 times their pedvars are selected as *picture pixels*, while any pixels adjacent to the picture pixels and with a charge 2.5 times their pedvars are labelled as *boundary pixels*. Isolated pixels with no picture or boundary pixels are removed from the camera. What remains defines the Cherenkov shower image in the camera, and the parametrization proceeds with these images.

The images are parametrized by characterizing their shape and orientation in the camera field of view, and are obtained from the first and second moments of the Cherenkov air shower image. The parameters, first proposed by Hillas [20], are *distance*, *length*, *width*, *azwidth*, *miss*, *asymmetry*, *frac3*, *alpha* and *size*. A brief description of the Hillas parameter can be found in Table 2.1, with some of them visible in Figure 2.11. The first six parameter are independent from each other and can be calculated directly from the second moments of the image. *alpha* is calculated from *miss* and *distance*, while *size* and *frac3* derive from the signal strength of the

Table 2.1: Summary of the Original Hillas Parameters

Parameter	Definition
Distance	Distance from the image centroid to the center of the field of view.
Length	RMS spread along the major axis of the image.
Width	RMS spread along the minor axis of the image.
Azwidth	RMS spread along the image width perpendicular to the distance to the center of the field of view.
Miss	Perpendicular distance of the major axis of the image to the center of the field of view.
Asymmetry	Measure of the asymmetry in light distribution along the major axis of the image.
Frac3	Percentage of the total light contained within the three pixels with the highest signals.
Alpha	Angle between the major axis of the image and the line from the centroid to the center of the field of view.
Size	Total charge contained in all of the pixels of the image.

The definitions are taken from [20].

pixel. *Size* and *frac3* depend on the total light from the air shower, which in turn depend on the energy of the primary gamma-ray photon.

2.3.4 Quality Selection & Shower Core Reconstruction

At this point, the images are tested against a series of selection criteria to validate the quality of the images. The image selection criteria are based on the parameters N_{tubes}, *size* and *distance*, which are listed in the Table 2.2. The parameters are used to remove images that would cause a poor reconstruction of the shower parameters, because either the images are too faint (N_{tubes}), or have irregular shape (*size*) or are too distant from the camera center and could be truncated at the camera edge (*dis-*

tance). N_{tubes} and *distance* are commonly set at the preconfigured values of ≥ 5 and $\leq 1.43°$ respectively, while optimization procedures have shown that different values of the *size* parameter may increase the sensitivity to sources with softer or harder spectra. In the standard VERITAS data analysis, the values of the size parameters are 200, 400 and 1000 for soft, medium and hard cuts respectively.

Table 2.2: Selection Criteria for Image Quality, Event Quality and γ/Hadron Separation of the Primary Gamma-Ray Photon

	Image selection			**Event selection**				γ/**hadron selection**		
Cuts	Size	N_{tubes}	dist.	Tel. comb.	# tel.	min. angle	Impact dist.	MSW[†]	MSL[‡]	θ^2
Soft	200	≥ 5	$\leq 1.43°$	No T1-T4	≥ 2	$\geq 10°$	≤ 10 km	1.15	1.3	≤ 0.03
Medium	400	≥ 5	$\leq 1.43°$	No T1-T4	≥ 2	$\geq 10°$	≤ 10 km	1.15	1.3	≤ 0.01
Hard	1000	≥ 5	$\leq 1.43°$	No T1-T4	≥ 2	$\geq 10°$	≤ 10 km	1.1	1.2	≤ 0.01

[†]Lower value for MSW is 0.05. [‡]Lower value for MSL is 0.05.

After the application of the image selection criteria, the data analysis applies the event selection criteria. In this case, an event is removed if less than two telescope images are left for reconstruction or if there are two telescope images left where the major axes of the images have an angle of $< 10°$. A specific telescope combination may also be removed at this stage. In the case of telescope events triggered by the T1-T4 combination, the events are removed from subsequent analysis if only one other telescope was triggered in the same event, since these are events that are dominated by the accidental coincidences of small showers due to the short baseline of the T1-T4 configuration. Once the shower core position is determined, the last event selection criteria consists in the removal of all showers with a large impact distance of ≥ 10 km to avoid biases in the calculation of the mean scaled parameters.

In the field of view of the cameras, the intersection of the major axes of the shower images gives the impact position of the primary gamma-ray particle. The impact position is given by the point in the camera plane where the weighted perpendicular

distance between the point and the major axes of the images is minimum. A measure of the position consistency of the shower core can be given by the parameter θ^2, which represents the square of the angle between the shower-reconstructed source position and the expected source position in the camera field of view. Small θ^2 angles highly suggest a gamma-ray source at the expected source position in the field of view. A cut on this parameter is useful to remove background events that are far from the core center.

2.3.5   Shower Parametrization

At this stage of analysis, more than 99% of the shower events are still largely composed of cosmic-ray events. In order to separate the gamma-ray induced events from the cosmic-ray events, a particular technique [10] has been developed to determine two event parameters, the *mean scaled length* and the *mean scaled width*. The technique involves the use of simulations of the gamma-ray showers and of the detector to produce look-up tables that contain the expected values of the parameters *length* and *width* from the *size* and impact distance r parameters, where r is the distance between the shower core and the telescope. The expected values from the look-up tables are then used to scale the calculated values of length and width, according to the formula

$$MSP = \frac{1}{N_{tel}} \sum_{i=1}^{N_{tel}} \frac{p_i}{\bar{p}_{simul}(size, r)} \tag{2.8}$$

where N_{tel} is the number of telescopes, p_i is the parameter involved for the scaling (length or width), and $\bar{p}_{simul}(size, r)$ is the average simulated parameter at the corresponding *size* and impact distance r. For gamma-ray initiated showers, the MSP should be ~1 while for cosmic-ray initiated showers, the MSP will tend to be larger. An upper limit on the MSP provides an effective means of rejecting cosmic-ray showers while retaining a relatively high number of gamma-ray showers.

2.3.6   Energy Reconstruction

Just as the case for the look-up tables for the MSP parameter, energy look-up tables are employed to estimate the energy for all telescope images that survive the image quality selection. The energy of the primary gamma-ray particle is calculated as the size-weighted average of all of the telescope image energy estimates. The observing conditions determine the look-up table that will be used, and the energy for each telescope image is decided by the value in the look-up table corresponding to the size and impact distance for that telescope.

2.3.7   Results Extraction

In the last stage of the data analysis, a series of cuts derived from shape and orientation of the shower images are applied to remove cosmic-ray events and retain as many gamma-ray events as possible (gamma-ray/hadron separation). The cuts are based on the mean scaled width and mean scale length and θ^2 parameters. The values of these parameters, which are derived from optimization procedures for softer or harder sources, are listed in Table 2.2. The cuts are conceived to minimize the ratio R_{bg}/R_γ^2. This ratio is proportional to the time required to detect a source at a certain flux level. An important part of the analysis at this stage is the determination of the background gamma-ray rate, and the background estimation is determined by two different methods, the *reflected region* model and the *ring background* model.

Under the assumption of an azimuthal distribution of cosmic rays in the field of view, the reflected region model derives background regions which are symmetrically displaced around the center of the field of view and which are far enough as possible from the source to avoid gamma-ray contamination. Background regions with overlap on bright stars are also remove from the background estimation. The method is most suited for point-like sources and sources of limited extension, but is not intended for sources at the center of the field of view. Since the background is estimated from
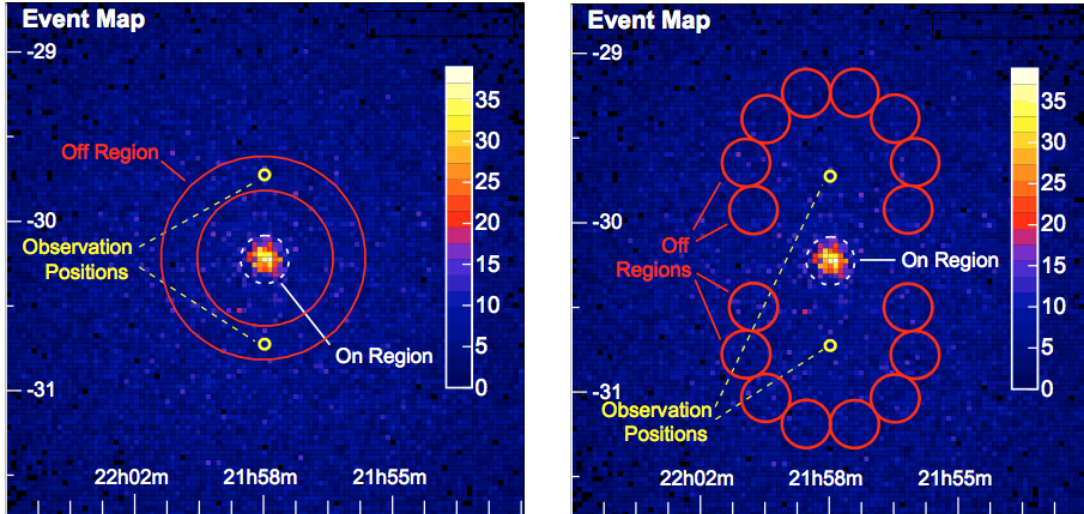
Figure 2.12.: Schematic representation of the ring-background model (left) and the reflected region model (right) [34].

events of the same runs, systematic effects from weather and hardware performance are reduced.

The ring-background model estimates the background by use of an annulus around the source region. Since the ring covers points at different offsets compared to the field of view center, an acceptance or relative event rate, must be applied to normalize the background rate. Just as in the reflected-region mode, any known gamma-ray source or star in the annulus needs to be removed. The ring-background model is most suitable for sources whose extension and position are not known a priori, and any observation mode can be used.

For source detection, one needs to calculate the gamma-ray event excess beyond the background rate from the source direction, and also the significance of the excess compared to the background. After the application of the MSW/MSL cuts, all events that are retained within the θ^2 cut are defined as ON events, N_{ON}. In order to calculate the excess N_{EX}, one needs to find the contamination in the ON source region of the OFF events N_{OFF}. N_{OFF} is calculated from one of the background region models explained previously. The background estimation model also furnishes

the normalization parameter of the source to background events α. In essence, α is the ratio of the effective exposure over observing time and area of the source region to background region. One can then derive the excess as

$$N_{EX} = N_{ON} - \alpha N_{OFF} \tag{2.9}$$

α changes according to the background estimation model employed. In the case of the reflected-region and ring-background models, the source and background region are at different positions in the field of view, and therefore α will need to depend on the *acceptance* of the camera. The acceptance is defined as the relative ratio of the gamma-ray events detected at a certain point in the camera compared to the total amount of events detected. In the reflected-region model, since the background regions are all at the same distance from the center of the field of view, the exposure is the same and α is just the inverse of the number of reflected regions

$$\alpha = \frac{1}{N_{tel}}. \tag{2.10}$$

In the case for the ring-background model, the acceptance needs to be taken into account, since the annulus of the ring-background model isn't symmetric with respect to the camera center. α is then defined as the integrated acceptance of the source region to the integrated acceptance of the background region

$$\alpha = \frac{\int_{ON} \eta(r) dA}{\int_{OFF} \eta(r) dA}, \tag{2.11}$$

where $\eta(r)$ is the acceptance at the radial distance r from the camera center. With the definition of α one can calculate the significance of the detection with the formula [35]

$$S = \sqrt{2} \left\{ N_{ON} \ln \left[\frac{1+\alpha}{\alpha} \left(\frac{N_{ON}}{N_{ON} + N_{OFF}} \right) \right] + \right.$$
$$\left. + N_{OFF} \ln \left[(1+\alpha) \left(\frac{N_{OFF}}{N_{ON} + N_{OFF}} \right) \right] \right\}^{1/2}. \tag{2.12}$$

The gamma-ray source rate R_γ can then be calculated as

$$R_\gamma = \frac{N_{ON} - \alpha N_{OFF}}{\tau} \pm \frac{\sqrt{N_{ON} - \alpha^2 N_{OFF}}}{\tau}, \tag{2.13}$$

where τ is the total dead time corrected exposure.

3. Multi-Wavelength Astronomy

While most of the effort of my research has been centered on the search for high-energy and very-high-energy emission from X-ray binaries, the multi-wavelength component has been a crucial and supportive addition to help pinpoint for signatures that may suggest higher forms of radiation emission. The instruments involved in my research have been vital for the investigations of the astronomical community for many years now. With the exception of the Rossi X-ray Timing Experiment (RXTE), all of these astronomical instruments are still operational and gathering new data to further our knowledge of the universe. The principle characteristics of these instruments is described in the following paragraphs.

3.1 Fermi/LAT

The Fermi Gamma-ray Space Telescope (Fermi) mission was launched in orbit on 11 June, 2008 on a Delta II Heavy launch vehicle by NASA and has been since securing data in all-sky survey mode since 4 August, 2008. It carries on board two scientific instruments: the *Gamma-ray Burst Monitor* (GBM) and the *Large Area Telescope* (LAT), which is the primary instrument on board the Fermi satellite.

The LAT instrument was designed and built by an international collaboration with hardware and software contributions from members from France, Japan, Sweden, Italy and the United States. The LAT is a wide field-of-view, high-energy gamma-ray telescope which covers the energy range from 20 MeV to 300 GeV. The primary observing mode of the LAT is the "scanning mode", in which the normal to the front of the instrument on alternate orbits points +35° from the zenith direction toward the pole of the orbit and then -35° from the zenith on the following orbit. This allows the LAT instrument to cover uniformly the sky after two orbits. At around 525 km in

Figure 3.1.: The Fermi Gamma-ray Space Telescope (Fermi) mission. Image Credit: NASA/DOE/Fermi LAT Collaboration.

elevation and at 25.5° in inclination, one orbit for Fermi corresponds to about three hours.

High-energy gamma-ray photons cannot be reflected or refracted, but are converted into a e^+e^- pair in the pair-conversion telescope. The LAT measures the electron and positron tracks from incident gamma-ray photons which result from pair-conversion in the converter-tracker, and determines the energy of the gamma ray from the electron-positron shower that develops in the calorimeter.

The converter-tracker (Figure 3.2) is composed of 16 planes of high-Z material (tungsten), with position-sensitive detectors that record the passage of the particles, and therefore are able to reconstruct the tracks of the particles that are produced by pair-conversion. One of the most complex compromises in the LAT design was the balance between the requirement for thin converters, to produce good PSFs at low energies where the PSF has a $\sim 1/E$ dependency on multiple scattering, and
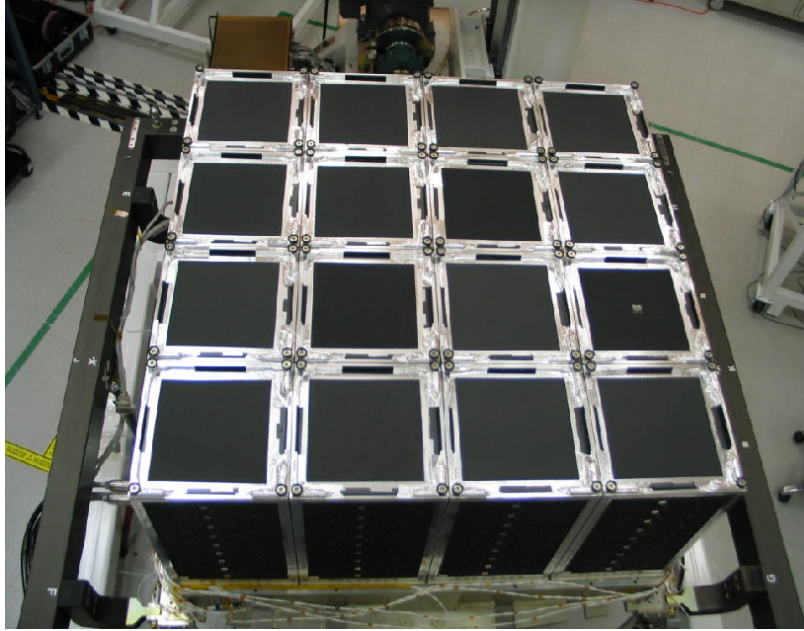
Figure 3.2.: Completed tracker array before integration with the anti-coincidence detector [36].

converter material to maximize the effective area at higher energies. This goal was accomplished by dividing the tracker into two sections, a "front" and "back" which respectively have thin (0.03 radiation lengths) and thick converters (~ 6 times thicker) to achieve the desired goal.

Each calorimeter module has 96 CsI(Tl) crystals, with each crystal of dimensions 2.7 cm×2.0 cm×32.6 cm. Each crystal is optically isolated and arranged horizontally in 8 layers of 12 crystals, with a total depth of the calorimeter of 8.6 radiation lengths. Each calorimeter module is displace by 90° one to another. Each CsI crystal provides three spatial coordinates: two coordinates for the physical position of the crystal in the calorimeter and a third which calculates the light yield asymmetry at the ends of the longer dimensions of the crystal. This arrangement allows for accurate reconstruction of the shower direction and determination of its spatial image (see Figure 3.3).
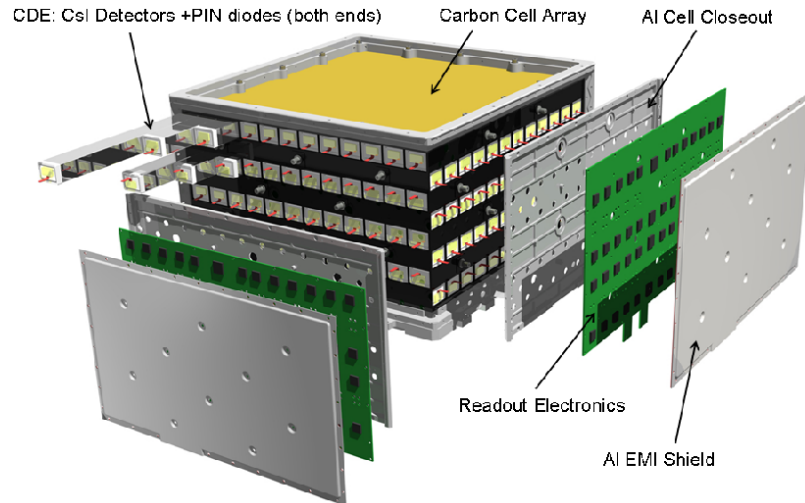
Figure 3.3.: Schematic view of the LAT calorimeter module. The 96 CsI(Tl) crystal elements are disposed in eight layer, rotated 90° one to another. The total calorimeter radiation depth is 8.6 radiation lengths [36].

The anti-coincident detector's main function is to provide charge particle background rejection, most of which is caused by background cosmic rays. Therefore its main requirement is to be able to discern and reject charge particle with maximum efficiency. The anti-coincident detector can provide at least an efficiency of 99.97% for detection of singly charged particles entering the field of view, averaged over the anti-coincident detector on the LAT. The anti-coincident detector covers the tracker array, and a programmable trigger and data acquisition system uses the signals from the trigger, calorimeter and anti-coincident subsystem to form a trigger. The onboard processing system is optimally devise to reject cosmic-ray background events while retaining the maximum possible number of gamma-ray photons, by the reconstruction of the e^+e^- pair paths in the tracker array.

The total aspect ratio of the Fermi/LAT tracker (the height to width ratio) is 0.4. This guarantees a large field of view and makes certain that almost all pair-conversion events that start in the tracker will end up in the calorimeter for the

Table 3.1: Summary of the Fermi/LAT Main Parameter Values

Parameter	Value or Range
Energy range	20 MeV – 300 GeV
Effective area at normal incidence[a]	9,500 cm^2
Energy resolution (equivalent Gaussian 1σ):	
100 MeV – 1 GeV (on axis)	9%–15%
1 GeV – 10 GeV (on axis)	8%–9%
10 GeV – 300 GeV (on-axis)	8.5%–18%
>10 GeV (>60° incidence)	≤6%
Single photon angular resolution (space angle)	
on-axis, 68% containment radius:	
>10 GeV	≤0.15°
1 GeV	0.6°
100 MeV	3.5°
on-axis, 95% containment radius	$< 3 \times \theta_{68\%}$
off-axis containment radius at 55°	$< 1.7\times$ on-axis value
Field of View (FoV)	2.4 sr
Timing accuracy	< 10 μsec
Event readout time (dead time)	26.5 μsec
Point source location determination[b]	$< 0.5'$
Point source sensitivity (>100 MeV)[c]	3×10^{-9} ph cm^{-2} s^{-1}

[a]Maximum (as function of energy) effective area at normal incidence. Includes inefficiencies necessary to achieve required background rejection. Effective area peak is typically in the 1 to 10 GeV range.
[b]High latitude source of 10^{-7} cm^{-2} s^{-1} flux at >100 MeV with a photon spectral index of –2.0 above a flat background and assuming no spectral cut-off at high energy; 1σ radius; 1-year survey.
[c]For a steady source after 1 year sky survey, assuming a high-latitude diffuse flux of 1.5×10^{-5} cm^{-2} s^{-1} sr^{-1} (>100 MeV) and a photon spectral index of –2.1, with no spectral cut-off.
[d]The values are taken from [36].

energy determination. Table 3.1 show a summary of the main characteristics of the Fermi/LAT instrument [36].

3.2 AGILE

The space mission AGILE (Astro-rivelatore Gamma a Immagini LEggero - Light Imager for Gamma-ray Astrophysics) is a satellite of the Italian Space Agency (ASI) dedicated to the study of the high-energy gamma-ray universe. The main scientific goal of the AGILE program is to provide excellent imaging capability both in the 30
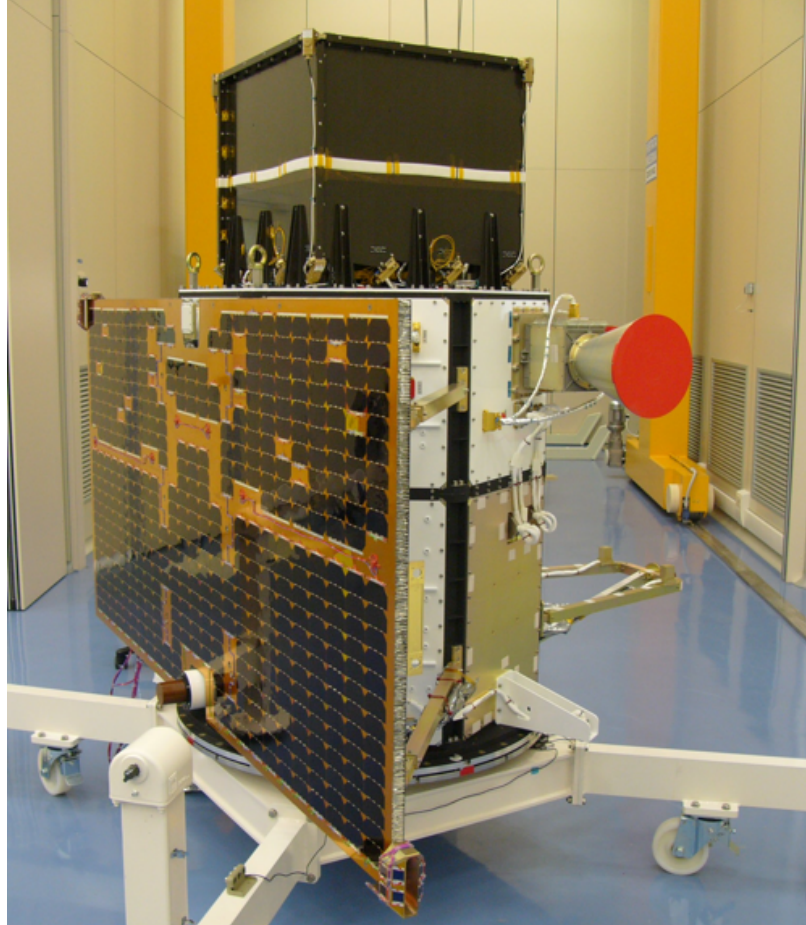
Figure 3.4.: The AGILE satellite before launch [37].

MeV-50 GeV and in the 18-60 keV energy bands with a very large field of view. The satellite was launched from the Sriharikota base on 23 April, 2007. The instrument is very compact and light ($\sim$120 kg), and aimed for the detection of new transients and for the monitoring of gamma-ray sources with a large field of view. The total satellite mass stands at $\sim$350 kg.

AGILE is composed of three detectors combined into one integrated instrument. The instrument consists in the Gamma-Ray Imaging Detector (GRID), the Hard X-Ray Imager (Super-AGILE) and the Burst-Mode Mini-Calorimeter, which is part of the GRID but capable of independently detecting GRBs and other transients in the 350 keV-100 MeV range. The integrated instrument is surrounded by an anti-

Table 3.2: Properties of the AGILE Instruments

Gamma-Ray Imaging Detector (GRID)	
Energy range	30 MeV – 50 GeV
Field of view	~ 2.5 sr
Flux sensitivity ($E > 100$ MeV, 5σ in 10^6 s)	3×10^{-7} (ph cm^{-2} s^{-1})
Angular resolution at 100 MeV (68% cont. radius)	$3.5°$
Angular resolution at 400 MeV (68% cont. radius)	$1.2°$
Source location accuracy (high Gal. lat., 90% C.L.)	$\sim 15'$
Energy resolution (at 400 MeV)	$\Delta E/E \sim 1$
Absolute time resolution	$\sim 2\,\mu$s
Deadtime	$\sim 100 - 200\,\mu$s
Hard X–ray Imaging Detector (Super-AGILE)	
Energy range	$18 - 60$ keV
Single (1-dim.) detector FOV (FW at zero sens.)	$107° \times 68°$
Combined (2-dim.) detector FOV (FW at zero sens.)	$68° \times 68°$
Sensitivity (18-60 keV, 5σ in 1 day)	~ 15 mCrab
Angular resolution (pixel size)	$6'$
Source location accuracy (S/N~ 10)	~ 1-$2'$
Energy resolution (FWHM)	$\Delta E \sim 8$ keV
Absolute time resolution	$\sim 2\,\mu$s
Mini-Calorimeter	
Energy range	$0.35 - 50$ MeV
Energy resolution (at 1.3 MeV)	13% FWHM
Absolute time resolution	$\sim 3\,\mu$s
Deadtime (for each of the 30 CsI bars)	$\sim 20\,\mu$s

All values are taken from [38].

coincidence system of plastic scintillators for the rejection of background charged particles.

The GRID is sensitive to the energy range 30 MeV-50 GeV, and consists of a Silicon-Tungsten Tracker, a Cesium Iodide Calorimeter and an Anti-coincidence system. It possesses a very fine spatial resolution and a very small dead-time for gamma-ray detection ($\lesssim 200\mu$s). The GRID is designed for an angular resolution of $\sim 15'$, a large field of view (~ 2.5 sr) and a sensitivity similar to that of EGRET for sources

that are within a 10-20° off-axis angle, and better for sources at larger off-axis angles. More properties of the GRID and other instruments can be viewed in Table 3.2.

Super-AGILE is an imager placed on top of the gamma-ray detector and is sensitive to the 18-60 keV band. Its angular resolution is 6′ and possesses a good sensitivity of ~10-15 mCrab on-axis for a 1-day integration. This gives AGILE the capability of simultaneous gamma-ray and hard X-ray source detection, with arcminute positioning and on-board GRB/transient alert capacity [37].

3.3 RXTE

Figure 3.5.: The Rossi X-ray Timing Explorer Mission. Artist credit: NASA. Image courtesy of the RXTE Collaboration.

The Rossi X-ray Timing Explorer (RXTE) mission observed the time structure of high-energy astrophysical objects such as black holes, neutron stars and X-ray pulsars. RXTE was named after the Italian scientist Bruno Rossi, who made major contributions in the fields of cosmic rays and particle physics. RXTE was launched in a low-Earth orbit on 30 December, 1995 by a NASA Delta rocket and was withdrawn

from service on 5 January, 2012, after 16 years of major discoveries on these extreme objects. As of 2012, RXTE-related refereed publications count more than 2000, and RXTE-related Ph.D thesis number count is over 90. The RXTE has three main instruments on board: the Proportional Counter Array (PCA), the High-Energy X-ray Timing Experiment (HEXTE) and the All Sky Monitor (ASM). The PCA and the ASM were the instruments that were used in my research.

3.3.1   RXTE/PCA

The PCA was designed to cover an energy range of 2.0–60.0 keV and consists of five, nearly identical, large-area xenon proportional counter units (PCUs). The field of view is about $1° \times 1°$. Each PCU has an area of ~ 1300 cm^2, for a total effective area of 6500 cm^2. The PCA main instrument properties are listed in the Table 3.3 [39].

Table 3.3: Proportional Counter Array Instrumental Properties

Properties	Values
Energy range:	2–60 keV
Energy resolution:	$< 18\%$ @ 6 keV
Time resolution:	1 μs
Spatial resolution:	collimator with 1° FWHM
Detectors:	5 proportional counters
Collecting area:	6500 cm^2
Layers:	1 Propane veto;
	3 Xenon, each split into two;
	1 Xenon veto layer
Sensitivity:	0.1 mCrab
Background:	2 mCrab

Table values from RXTE Guest Observer Facility Web Site `http://heasarc.gsfc.nasa.gov/docs/xte/PCA.html`.

3.3.2 RXTE/ASM

The All-sky Monitor is composed of three wide-angle shadow cameras containing proportional counters with a total collecting area of 90 cm^2. The main properties of the ASM are listed in the Table 3.4. The ASM was built by the Center for Space Research (CSR), currently the MIT Kavli Institute, at MIT [40].

Table 3.4: All-Sky Monitor Instrumental Properties

Properties	Values
Energy range:	2–12 keV
Time resolution:	80% of the sky every 90 minutes
Spatial resolution:	$3' \times 15'$
Number of shadow cameras:	3, each with 6×90 degrees FOV
Collecting area:	90 cm^2
Detector:	Xenon proportional counter, position-sensitive
Sensitivity:	30 mCrab

Table values from RXTE Guest Observer Facility Web Site `http://heasarc.gsfc.nasa.gov/docs/xte/ASM.html`.

Table 3.5: RXTE Experiment Data System Instrument Modes

Transparent mode, using 1, 2, or 3 EAs
Event mode, using 1 or 2 EAs
Binned mode (time and/or energy)
Burst catcher mode
Fourier transform mode
Pulsar fold mode
Autocorrelation mode
Arrival time differences histogram mode

Table values from RXTE Guest Observer Facility Web Site `http://heasarc.gsfc.nasa.gov/docs/xte/EDS.html`.

The events that are detected by the PCA and ASM are processed on board by the Experiment Data System (EDS) before being forwarded to the telemetry stream. The EDS consists of eight Event Analyzers (EA), of which six are committed to the PCA

and two to the ASM. Each EA possesses an Intel 80286 processor with associated memory. The EAs can be programmed autonomously to deal with incoming events from the instruments in any of the modes listed in the Table 3.5.

3.4   Swift
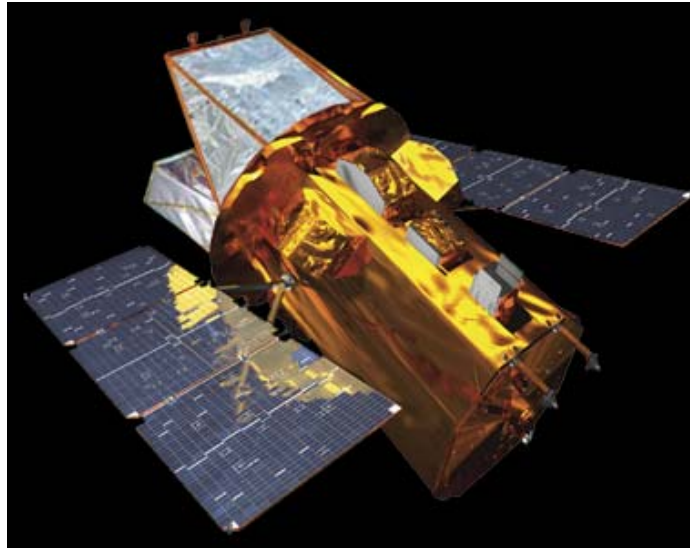
Figure 3.6.: The Swift Gamma-Ray Burst Mission. Artist credit: NASA. Image courtesy of the Swift Gamma-Ray Burst Mission Collaboration.

The Swift Gamma-Ray Burst Mission, commonly known as Swift, consists in a multi-wavelength observatory for the study of gamma-ray bursts (GRBs). Its three instruments, the Burst Alert Telescope (BAT), the X-ray Telescope (XRT) and the Ultraviolet/Optical Telescope (UVOT), coexist to observe GRBs and their afterglows in the gamma-ray, X-ray, UV and optical bands. It was launched into orbit on 20 November, 2004 on a Delta II rocket, and is managed by an international consortium of members from the United States, the United Kingdom and Italy.
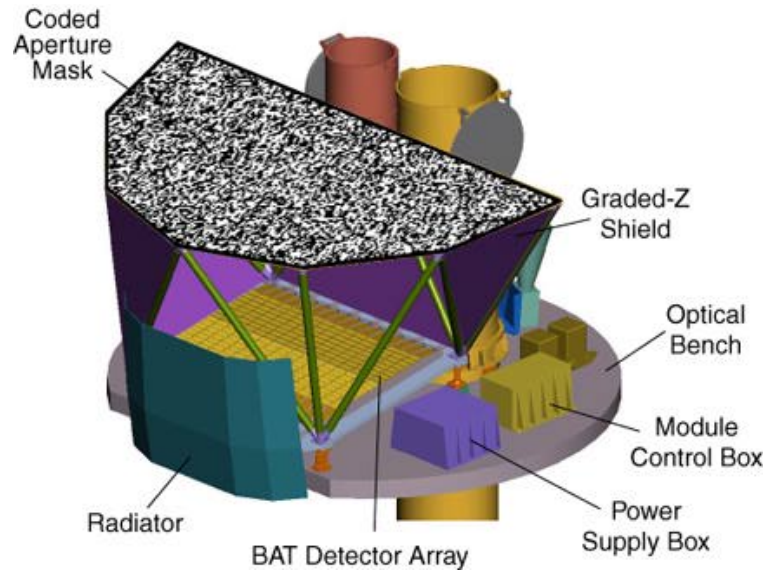
Figure 3.7.: Cut-away drawing of the Burst Alert Telescope (BAT). Image courtesy of Swift Gamma-Ray Burst Mission Collaboration.

3.4.1 Swift/BAT

The BAT is designed to cover the prompt emission from GRBs over the whole sky. With a large field of view (1.4 sr) and a quick slew time, it can detect the position of GRBs in the sky with an accuracy of 1-4′ in 15 seconds. The BAT uses a coded-aperture mask composed of $\sim$ 54,000 lead tiles, of dimensions $5 \times 5 \times 1$ mm, which are mounted on a 5 cm thick composite honeycomb panel and placed 1 meter above the detector plane. The 12×0.6 m sensitive area of the BAT detector plane is formed by 32,768 pieces of $4 \times 4 \times 2$ mm CdZnTe (CZT). Groups of 128 detector elements are collected into 8×16 arrays, each one of which is connected to 128-channel readout Application Specific Integrated Circuits (ASICs). The detector modules, which contain each two such arrays, are further grouped in blocks of eight. The hierarchical structure, together with the coded-aperture technique, allows the BAT the possibility of losing individual pixels, individual detector modules and even whole blocks without losing the ability to detect GRBs and determine positions [41].

Table 3.6: Burst Alert Telescope Instrument Properties

Property	Description
Aperture	Coded mask
Detecting Area	5240 cm^2
Detector	CdZnTe
Detector Operation	Photon counting
Field of View	1.4 sr (partially-coded)
Detection Elements	256 modules of 128 elements
Detector Size	4 mm $\times$ 4 mm $\times$ 2mm
Telescope PSF	17′
Energy Range	15-150 keV
Energy Resolution	∼7 keV

Table values from Swift Gamma-Ray Burst Mission Web Site
`http://swift.gsfc.nasa.gov/about_swift/bat_desc.html`.
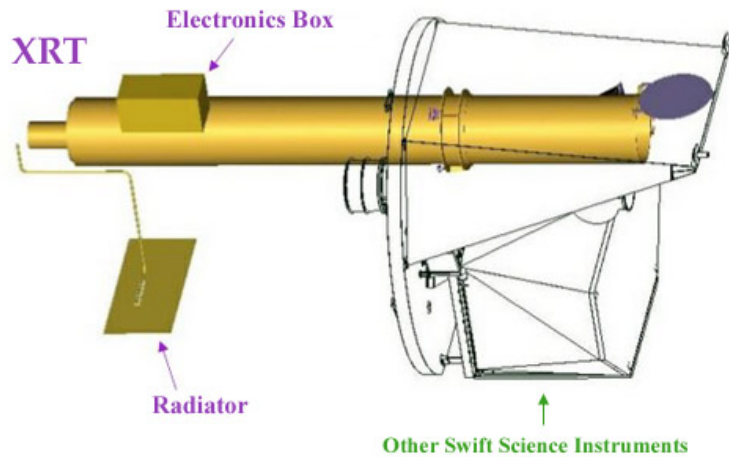
Figure 3.8.: Schematic diagram of the Swift/XRT. Image credit: Swift Gamma-Ray Burst Mission Collaboration.

3.4.2 Swift/XRT

The Swift/XRT is composed of a grazing incidence Wolter Type I X-ray telescope with 12 nested mirrors, which are made to focus on single MOS charge-coupled device (CCD), similar to those on the XMM-Newton EPIC MOS cameras. It has an effective

Table 3.7: X-Ray Telescope Instrument Properties

Property	Description
Telescope	JET-X Wolter I
Focal Length	3.5 m
Effective Area	110 cm^2 @ 1.5 keV
Telescope PSF	18 arcsec HPD @ 1.5 keV
Detector	EEV CCD-22, 600 × 600 pixels
Detector Operation	Imaging, Timing, and Photon-counting
Detection Element	40 × 40 micron pixels
Pixel Scale	2.36″/pixel
Energy Range	0.2-10 keV
Energy Resolution	∼140 eV @ 6 keV
Sensitivity	2×10^{-14} erg cm^{-2}s^{-1} in 10^4 seconds

Table values from Swift Gamma-Ray Burst Mission Web Site `http://swift.gsfc.nasa.gov/about_swift/xrt_desc.html`.

area of 110 cm^2, $23.6' \times 23.6'$ field of view, $18''$ resolution and a 0.2-10 keV energy range. The X-ray telescope can acquire fluxes, perform spectral analysis and produce light curves of GRBs and their afterglow, covering a dynamic range that spans over seven order of magnitude.

3.5   MAXI

The Monitor of All-sky X-ray Image (MAXI) experiment is devised to continuously survey X-ray sources and their variabilities on the International Space Station (ISS). Located at the Equipment Exchange Unit (EER) site on the Japanese Experiment Module - Exposed Facility (JEF), MAXI is made up of a pair of highly sensitive X-ray detectors, the Gas Slit Camera (GSC) and the Solid-state Slit Camera (SSC) [42].

Every 96 minutes, MAXI scans almost the entire sky. On the ISS, MAXI has been observing the in X rays since August of 2009. It was envisioned for a mission life time of more than two years. The detection sensitivity is about 20 mCrab (at the 5σ level) for one orbit, 2-3 mCrab for one day and 1 mCrab for one week, reaching a source limit of 0.2 mCrab in the one-year observation.

Figure 3.9.: View of MAXI on the Japanese Experiment Module - Exposed Facility (JEF) on the ISS. Image credit: MAXI.

Table 3.8: Properties of MAXI Slit Cameras

	GSC: Gas Slit Camera	SSC: Solid-state Slit Camera
X-ray detector	12 pieces of one-dimensional PSPC; $Xe + CO_2$ 1%	32 chips of X-ray CCD; 1 square inch, 1024×1024 pixels
X-ray energy range	2-30 keV	0.5-12 keV
Total detection area	5350 cm^2	200 cm^2
Energy resolution	18% (5.9 keV)	$\leq$150 eV (5.9 keV)
Field of view*	$1.5°\times160°$	$1.5°\times90°$
Slit area for camera unit	20.1 cm^2	1.35 cm^2
Detector position resolution	1 mm	0.025 mm (pixel size)
Localization accuracy	0.1°	0.1°
Absolute time resolution	0.1 ms (minimum)	5.8s (nominal)
Weight‡	160 kg	11 kg

* FWHM $\times$ Full-FoV

† MAXI total weight: 520 kg

‡ GSC consists of 6 camera units, where each unit consists of two PCs. SSC consists of two camera units, SSC-Z and SSC-H.

The values are taken from [42].

3.6 PAIRITel

The Peters Automated Infrared Imaging Telescope (PAIRITel) is an automated 1.3m telescope which is located on Mt. Hopkins in Arizona. The telescope contains the Near-Infrared Camera and Multi-Object Spectrometer (NICMOS3) arrays, which

Figure 3.10.: Mt. Hopkins 2MASS 1.3-Meter Telescope. Photo by Rae Stiening.

were previously employed in the Two Micron All-Sky Survey (2MASS) project [43], to simultaneously view the near-infrared (NIR) J, H, and K_s (1.2, 1.6, and 2.2μm, respectively) bands. PAIRITel resolution is 1.2 arcsec pixel^{-1} (2 arcmin FoV). PAIRI-Tel was designed be to an automated, queue-based observatory. Its prime objective is to be able to rapidly respond to targets of opportunity (ToOs), such as gamma-ray burst (GRB) alerts from space-based satellites [44].

3.7 AMI-LA

The *Arcminute Microkelvin Imager* (AMI) is made up of a pair of interferometer arrays, called respectively the Small Array (SA) and Large Array (LA), operating on 6 different frequency channels spanning from 13.9 to 18.2 GHz, with a 4.3 MHz bandwidth, situated in Cambridge, UK. The telescope is primarily aimed at the Sunyaev-Zeldovich imaging of clusters of galaxies. The Large Array is used for ob-

Figure 3.11.: Arcminute Microkelvin Imager Large Array (AMI-LA). Image credit: AMI Consortium.

servations on angular scales of $\approx 30''$ and declinations angles $> -20°$, and possesses a flux sensitivity of 3 mJy s$^{1/2}$. All eight 12.8-meter diameter Cassegrain antennas of the LA are in a close, two-dimensional array, in an approximately eastwest linear direction, with a baseline spanning ~ 120 meters [45]. For our study, we take advantage of the large data set on Cygnus X-3 provided by the AMI-LA[1].

---

[1] http://www.mrao.cam.ac.uk/~guy/cx3/

Table 3.9: AMI Technical Information

	Small Array	Large Array
Number of antennas	10	8
Antenna diameter	3.7 m	12.8 m
Antenna efficiency	75%	67%
Antenna mount	Equatorial	Equatorial
Baseline lengths	5 to 20 m	18 to 110 m
Primary beam (15.7 GHz)	$20.1'$	$5.5'$
Synthesized beam	$\approx 3'$	$\approx 30''$
Polarization measured	Stokes I + Q	Stokes I + Q
Flux sensitivity	30 mJy s$^{-1/2}$	3 mJy s$^{-1/2}$
Declination range	$> -15°$	$> -20°$

Information is from the Cavendish Laboratory Astrophysics Group public web site
`http://www.mrao.cam.ac.uk/facilities/ami/ami-technical-information/`

4. X-Ray Binaries

4.1 Introduction

In very general terms, X-ray binaries (XRBs) can be defined as systems that are composed of a compact object, either a neutron star or a black hole, and of an optical companion star. These are considered as closed systems, due to the transfer of matter from the companion star to the compact object. By optical companion, it is understood that nuclear burning is still occurring inside the companion star. There are a few hundred XRBs within our galaxy and in the neighboring galaxies [46].

To better distinguish their physical properties, XRBs are divided into high-mass X-ray binaries (HMXBs) and low-mass X-ray binaries (LMXBs), a distinction that refers to the optically visible companion star [47]. In HMXB, the optical companion is a Be star ($M \geq 5M_\odot$) or OB supergiant ($M \geq 15M_\odot$), with usually long orbital periods (tens of days or more) and eccentric orbits of the primary star. Mass transfer is by accretion from the circumstellar equatorial disk of the secondary star or by stellar wind from the supergiant, which may lose up to 10^{-5} $M_\odot$ yr^{-1}.

In the case of LMXB, the low-mass companion star can be a late-type main-sequence star, an A-type star or a F-G-type sub-giant. The companion star mass varies from several solar masses to less than one solar mass. LMXB systems usually possess shorter orbital periods (from less than an hour to tens of days) and undergo mass transfer by Roche lobe overflow, which fuels an optically thick accretion disk which is responsible for the high X-ray luminosity [48].

Accretion is a process that regards the gradual accumulation of matter from the companion star onto the compact object. Since the matter from the companion star possesses angular momentum, it cannot fall directly on the compact object and therefore forms a disk-like structure around the compact object. As the matter falls

into the extremely deep gravitational well of the compact object, it is accelerated to very high velocities. The viscosity of the inner disk layers heats the disk and predominantly causes the radiation in the X-ray band [49].

The luminosity class further divides HMXBs into Be/XRBs, when the optical star is a dwarf, sub-giant or giant OB star (luminosity class III, IV, V) and supergiants XRBs (SG/XRBs), if they contain a luminosity class I-II star. In Be/XRBs, the optical companion is a Be star and the compact object is a neutron star. Be stars are non-supergiant, fast-rotating B-type and luminosity class III-IV stars which present emission lines, which is the reason for the addition of the "e" in their spectral-type designation. The emission lines are attributed to the equatorial disk, which is formed from matter expelled from the rapidly-rotating Be star.

During periastron, the neutron star passes close to the disk, which causes massive accretion onto the compact object. The conversion of kinetic energy into thermal energy is the cause of the radiation in the X-rays. In systems with large eccentric orbits, a transient Roche lobe overflow may occur during the periastron passage when a large fraction of the Be star's disk is thought to be accreted. This is the condition that is believed to occur in 1A 0535+262 during the periastron passages [50].

4.2   Gamma-Ray Emission Models for X-Ray Binaries

Gamma-ray binaries are XRBs that display non-thermal emission from radio to high energy (HE, >100 MeV) and very high energy (VHE, >100 GeV) gamma rays, with the greater part of their energy released in the MeV to TeV range [18]. Currently as of 2013, five are the gamma-ray binaries that are known to emit at TeV energies. These are LS I +61°303 [51], LS 5039 [52], PSR B1259–63 [53], HESS J0632+057 [54] and 1FGL J1018.6 [55]. Of these binaries, LS I +61°303 [56], LS 5039 [57], PSR B1259–63 [58] and 1FGL J1018.6 [59] are also GeV emitters. Gamma-ray emission has also been observed in microquasars (Cygnus X-3 [60], and possibly Cygnus X-1 [61,62]), the colliding wind binary η Car [63], the symbiotic bi-

nary V407 Cyg [64] and dozens of millisecond pulsars in binaries. All of the gamma-ray binaries detected are HMXBs, which is in itself an interesting circumstance. The non-thermal gamma-ray emission has been observed to be modulated with the orbital period.

While gamma-ray emission seems to be a characteristic of HMXBs [18], a distinct class of gamma-ray pulsars in LMXBs has been discovered as well. The pulsars in these systems are old pulsars that have been spun-up to millisecond rotation periods by the accretion of mass from their stellar companion [65]. The accretion phase turns off once the rotation becomes fast enough and the pulsar wind suppresses the accretion of matter from the companion star. In certain situations, the pulsar wind may be strong enough to ablate the surface of its low-mass companion ($\ll 0.1 M_\odot$), while other binary systems with more massive stellar companions ($\gtrsim 0.1 M_\odot$) may present stellar winds sufficiently strong to overcome the pulsar winds. Both systems produce bow shocks, and are respectively called *black widows* and *redbacks*. Fermi/LAT has observed gamma-ray emission in a dozen of black widows and redbacks [66].

The nature of gamma-ray emission from these binary systems is currently a subject of interest and debate in the gamma-ray astronomy community. Two different scenarios have been proposed to account for the non-thermal emission from gamma-ray binaries: the microquasar emission model [67], and the pulsar binary emission model [68]. In the first case, the particle acceleration in the jets of microquasars is likely responsible for the up-scattering of the ambient photons. In the second scenario, gamma-ray emission occurs by up-scattering of photons from the particle acceleration in the shocked regions of the pulsar and stellar winds.

Gamma-ray binaries may also be important for the study of stellar evolution, since they could represent the early stage of formation of HMXBs. The theory on the formation of HMXBs containing neutron stars predicts an initial stage of interaction between pulsars and stellar companions of early spectral type [69]. The X-ray emission from these system is not envisioned to be particularly strong in the early stages of formation, and may not be recognized as X-ray sources. The second Fermi/LAT
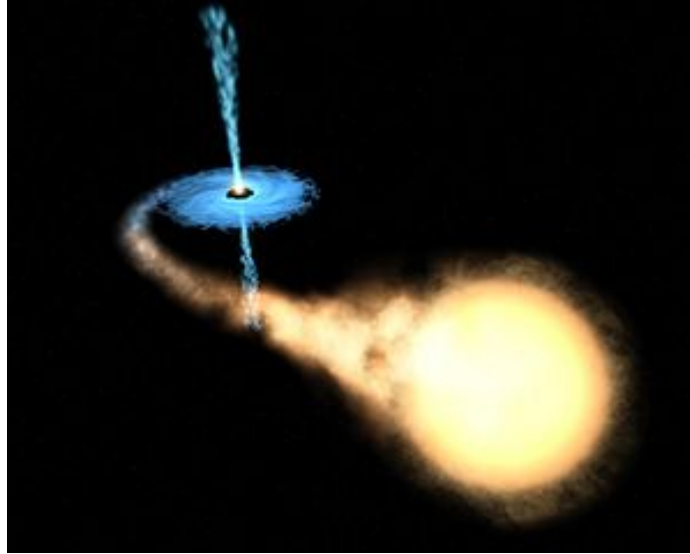
Figure 4.1.: In a binary system, a black hole strips matter from the companion star, creating an accretion disk and relativistic jets. This is similar to what occurs in quasars, but on scales millions of times smaller [71].

catalog of gamma-ray sources contains 1873 sources, of which 575 are not known to have a confirmed counterpart at other wavelengths and could in potential be gamma-ray binaries [70]. Therefore, gamma-ray binaries may be more plentiful than imagined, and many might await discovery.

4.2.1 Microquasar Emission Model

Microquasars are XRBs that possess relativistic jets, and can be very bright in the X rays [72]. These systems are powered by accretion of matter from the companion star onto the compact object. Microquasars have acquired this name because they are miniature versions of quasars ("quasi-stellar radio sources"). These are the nuclei of very energetic and distant galaxies harboring supermassive black holes, and are able to produce in a region as big as the solar system the luminosities of 100 galaxies like our own. The mass of the central black hole in quasars is typically several million
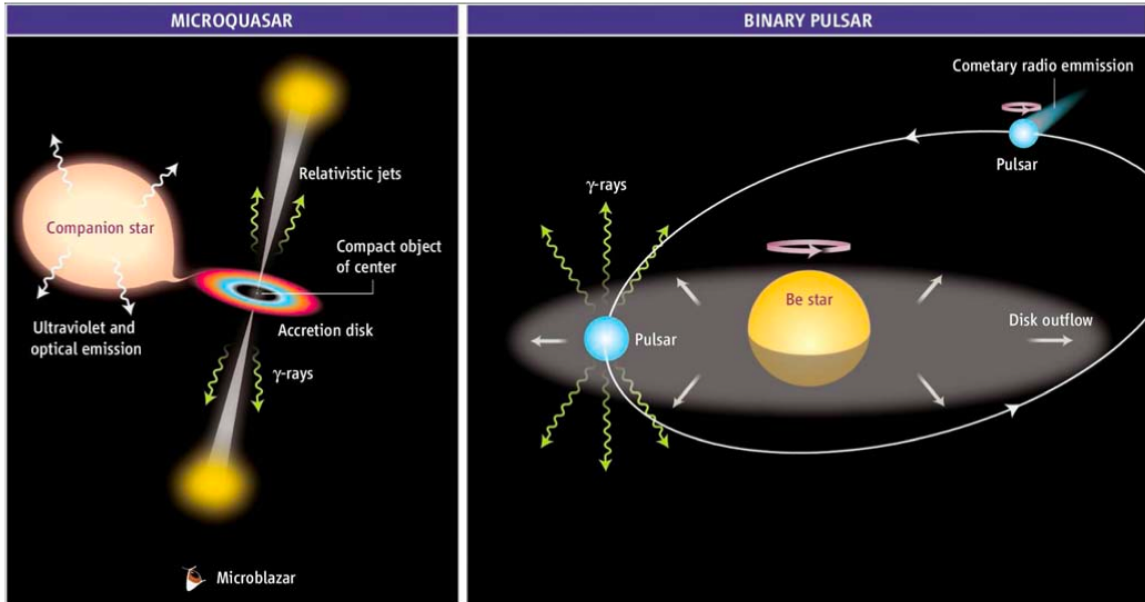
Figure 4.2.: Schematic view of a microquasar and of a pulsar-wind gamma-ray binary [71].

times the mass of the compact object at the heart of a microquasar, hence the use of the prefix "micro" in microquasar.

The proof of the existence of relativistic jets in microquasars, following the observations of the low-mass black-hole XRB GRS 1915+105 [72], allowed for the speculation that the particle energy in the microquasar jet could be comparable to that in the AGN jet, making microquasars strong candidates for gamma-ray emission [73]. The microquasar jet model for the generation of VHE emission seemed a natural consequence, since VHE emission is seen in blazars. This idea had been made stronger by observations showing that the kinetic power in microquasar jets may be greater than $10^{39}\,\mathrm{erg\,s^{-1}}$, which is higher than their radiative power [74].

Non-thermal emission processes in microquasars are mainly considered to be of two different origins: *leptonic* and *hadronic*, due to the different type of particles involved in the sources. In the case of leptonic emission in microquasars, jets with very energetic electrons can produce TeV gamma-ray emission by the up-scattering
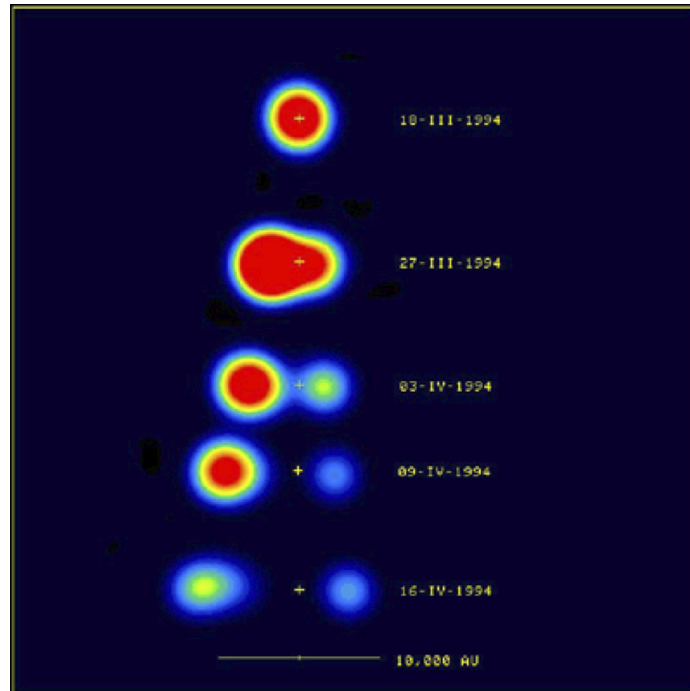
Figure 4.3.: The sequence of images of GRS 1915+105 shows the temporal evolution at radio wavelengths (3.6 cm) of a pair of plasma clouds ejected from the black hole surroundings at 98% of the speed of the light [72].

of external photons, mainly from the disk, the companion star or the interstellar medium (ISM), through inverse Comptonization. Re-acceleration of electrons in the shocks of the extended lobes, formed by the deceleration of the jets in the ISM, can cause X-ray synchrotron emission and possibly TeV emission by inverse Compton scattering of CMB photons by the accelerated electrons [75].

In the case of hadronic emission, one can imagine pp interactions between the protons in the jet and the protons from the stellar wind of the companion star. In early-type stars, the stellar winds can release as much as $10^{-5}\,M_\odot \mathrm{yr}^{-1}$, where the terminal velocities of the stellar wind can reach $\sim 10^3\ \mathrm{km\ s}^{-1}$ and have high densities. In the case of a strong shock by the jet with the stellar wind, between the compact object and the star where the ram pressure of the wind could completely balance the jet pressure, the particles from the jet could be isotropized and re-accelerated.

Through pp interactions, a gamma-ray source could be visible from the subsequent π^0-decays, photomeson and photodisintegration processes. The emission, typically at the level of $\sim 10^{32-33}$ erg s^{-1} at energies above 1 TeV, is mostly isotropic, but could be dependent upon absorption processes occurring within the systems, mainly from $\gamma\gamma$ pair absorption.

For the hadronic emission scenario, the extreme conditions required for the emitting region would have strong consequences for the physics of jets and their close environment [76]. Hadronic models envision production of neutrinos, and some high-mass microquasars, for certain values of distance and integration times, might be detectable sources with neutrino detectors such as ICECUBE.

4.2.2   Pulsar Binary Emission Model

For the pulsar wind interaction scenario, the slowing rotation of a young pulsar provides the stable energy for the relativistic particle winds by means of its rotational energy. In the shock between the pulsar winds and the winds from the companion star, the power can be radiated at different frequencies with efficiencies depending on the physical parameters of the shock region. Compton-scattering of relativistic electrons from the pulsar on the photons from the primary star is probably the most likely mechanism of production of X-ray to gamma-ray emission. The pulsar-wind model requires neutron stars young enough to furnish large spin-down energies [68].

In this context, LS I +61°303 is somewhat similar to the gamma-ray binary PSR B1263-59. Of the gamma-ray binaries, only PSR B1263-59 is a system known to contain a radio pulsar, with a spin period of 47.76 ms and spin-down luminosity of $\dot{E}_R \sim 8 \times 10^{35}$ erg s^{-1} [77]. Recent observations at radio wavelengths suggest the idea that LS I +61°303 may be a gamma-ray pulsar rather than a microquasar [78]. VLBA images of the radio emission in LS I +61°303 reveal a relativistic wind from the compact object that changes shape with the orbital phase. Radio emission elongated along one direction with position angle dependent on orbital phase and a repeatable
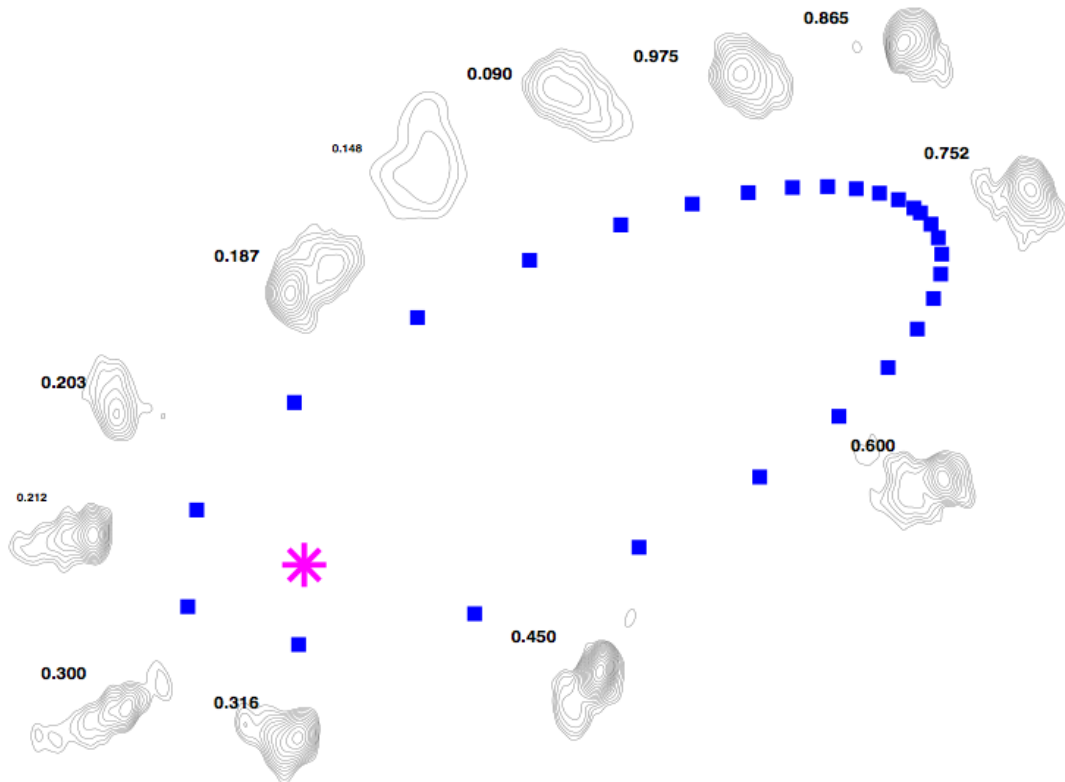
Figure 4.4.: Orbital phase dependence of the radio profile in LS I +61°303. The cometary tail can be seen pointing away from the Be star around periastron. The radio profiles becomes more compact, and therefore brighter, on the near side ($\phi \sim 0.5$) of the orbit compared to the far side ($\phi \sim 0.0$) [78].

shape over the orbits is a natural behavior in a binary PWN scenario. However in the microquasar scenario, the jet direction is not expected to change with orbital phase.

The physical processes responsible for high energy emission are generic to both microquasars and pulsar binaries, and differ in the locations of the particles, the flow in which they are placed and the dominant radiation field that is present. Even with this in mind, it becomes difficult to discern signatures for each scenario. The discovery of pulsations would be decisive proof for the pulsar-wind scenario in gamma-ray binaries. On the other hand, the mass of the compact object exceeding the $3M_\odot$

limit would rule out the pulsar interpretation. The detection of VHE emission from confirmed black hole X-ray binaries, such as Cygnus X-1 or GRS 1915+105, would furnish strong observational support for the gamma-ray emission in the microquasar model. In the absence of a "smoking gun" situation, indirect evidence for each model must be gathered. In favor of the pulsar binary model, there is to say that the high energy gamma-ray emission, as seen in gamma-ray binaries, resembles the spectral shape of pulsars, and pulsars and pulsar-wind nebulae (PWN) are the most common class of galactic sources in the HE and VHE energy band. As in the case for LS I +61°303 [78], high resolution radio images would be able to identify clearly whether the high-energy particles that trigger the VHE emission emanate as pulsar winds or as highly collimated microquasar jets.

5. Multi-Wavelength Observations of 1A 0535+262

5.1 Observations & Data Reduction

My first major project involved the X-ray to very-high-energy data analysis and interpretation of the December 2009 major X-ray outburst from the Be/X-ray binary system 1A 0535+262. The system consists of a pulsar of period 103 s in an eccentric orbit (e = 0.47) around an O9.7-B0 IIIe star. The orbital period is 111 days [79]. Major X-ray outbursts have observed from the source since its discovery during a major outburst in 1975 [80]. X-ray observations of 1A 0535+262 may suggest the formation of a transient accretion disk during giant outbursts [81], which might be the cause of the approximate 5-year reoccurrences of the X-ray outbursts. This work was presented at the 217th Winter AAS meeting Seattle, WA (2011) [82]. The details of the study can be viewed in the paper Acciari et al. (2011) [83].

5.1.1 VERITAS

VERITAS observed 1A 0535+262 for a total of 30 hours. After the application of quality-selection criteria, which removed data taken during bad weather or affected by hardware-related problems, 23 hours 40 minutes remained. For some observations only three telescopes were operational (missing telescope 4 on 24 December, 2009 and 10 February, 2010), leading to a moderately reduced sensitivity during these periods. The triggering criterion (a counting rate of >0.1 counts s^{-1} reported by the Swift/BAT instrument) for observations of flaring X-ray binaries with VERITAS was fulfilled on 5 December, 2009 [84]. Observations started on 9 December, 2009, shortly after the beginning of the giant flare. They were delayed by one day due to very bright moonlight conditions. The observation covered most of the flare, included the

apastron phase, and continued for almost 90 days until the following periastron phase. Table 6.1 shows the daily observation log, including weather condition, elevation range and moonlight condition. Figure 5.1 (right) shows the relative orbit of 1A 0535+262 around the Be companion star, with the VERITAS observations relative to the orbital phase during the X-ray outburst.

The analysis steps consist of calibration, image cleaning, second-moment parameterization of the recorded images [20], reconstruction of shower direction and impact parameter using stereoscopic methods (see e.g. [85]), gamma-ray/hadron separation and the generation of sky maps. More details of the general VERITAS analysis can be viewed in the Section 2.3. Images in at least three cameras were required; additional cuts on the shape of the event images and direction of the primary particles were used to reject the far more numerous background events. These cuts were optimized for a 5% Crab Nebula flux source. The energy threshold after analysis cuts was 220 GeV at a 10° zenith angle and 450 GeV at a 40° zenith angle and the systematic error on the energy estimation of the primary gamma rays was about 20%. The data were taken in wobble mode [86], wherein the object was positioned at a fixed offset of 0.5° in one of four directions from the camera center. The search region for photons from the putative gamma-ray source was defined by a 0.1° radius circle centered on the position of the Be star in 1A 0535+262 [87]. The background in the source region was estimated from the same field of view using the ring-background model with a ring size of 0.5° (mean radius) and a ring width of 0.1° [88]. In order to reduce systematic errors in the background estimation, regions around stars with B magnitudes brighter than 6 were excluded.

5.1.2   Fermi/LAT

For this work we used data from LAT observations of 1A 0535+262 that were conducted between 30 November, 2009 and 22 February, 2010. We used the Fermi Science Tools v9r15p2 software analysis package to reduce the data and followed the

Table 5.1.   VERITAS Observation Log for 1A 0535+262

Date	Observation Time (min)	Elevation Range	N_{tel}	Observing Conditions
2009/12/06	20	$78^o - 80^o$	4	moon 80% illuminated
2009/12/07	40	$58^o - 65^o$	4	bad weather, moon 70% illuminated
2009/12/09	38	$83^o - 85^o$	4	moon 48% illuminated
2009/12/10	176	$48^o - 84^o$	4	moon 37% illuminated
2009/12/11	52	$56^o - 80^o$	4	-
2009/12/12	40	$62^o - 65^o$	4	-
2009/12/15	40	$53^o - 56^o$	4	-
2009/12/16	60	$65^o - 74^o$	4	-
2009/12/17	60	$68^o - 75^o$	4	-
2009/12/18	60	$75^o - 82^o$	4	-
2009/12/19	60	$61^o - 69^o$	4	-
2009/12/20	60	$61^o - 70^o$	4	-
2009/12/21	80	$67^o - 81^o$	4	bad weather
2009/12/24	60	$59^o - 68^o$	3	-
2009/12/25	60	$49^o - 58^o$	4	-
2009/12/26	40	$55^o - 57^o$	4	-
2010/01/05	37	$76^o - 80^o$	4	-
2010/01/07	60	$69^o - 76^o$	4	-
2010/01/09	43	$80^o - 85^o$	4	bad weather
2010/01/11	8	$68^o - 70^o$	4	-
2010/01/12	60	$70^o - 78^o$	4	-
2010/01/14	38	$71^o - 76^o$	4	-
2010/01/16	60	$73^o - 81^o$	4	-
2010/01/17	60	$57^o - 65^o$	4	-
2010/02/05	12	$82^o - 83^o$	4	-
2010/02/07	20	$77^o - 80^o$	4	-
2010/02/08	40	$54^o - 62^o$	4	-
2010/02/10	37	$60^o - 71^o$	3/4	-
2010/02/12	60	$79^o - 84^o$	4	-
2010/02/16	60	$70^o - 79^o$	4	-
2010/02/18	60	$72^o - 82^o$	4	moon 89% illuminated
2010/02/20	60	$75^o - 83^o$	4	moon 98% illuminated

Note. — Data taken in bad weather or under very bright moonlight conditions ($> 50\%$ illumination) have been excluded from the data analysis. The column N_{tel} contains the number of working telescopes, from 3 to 4.
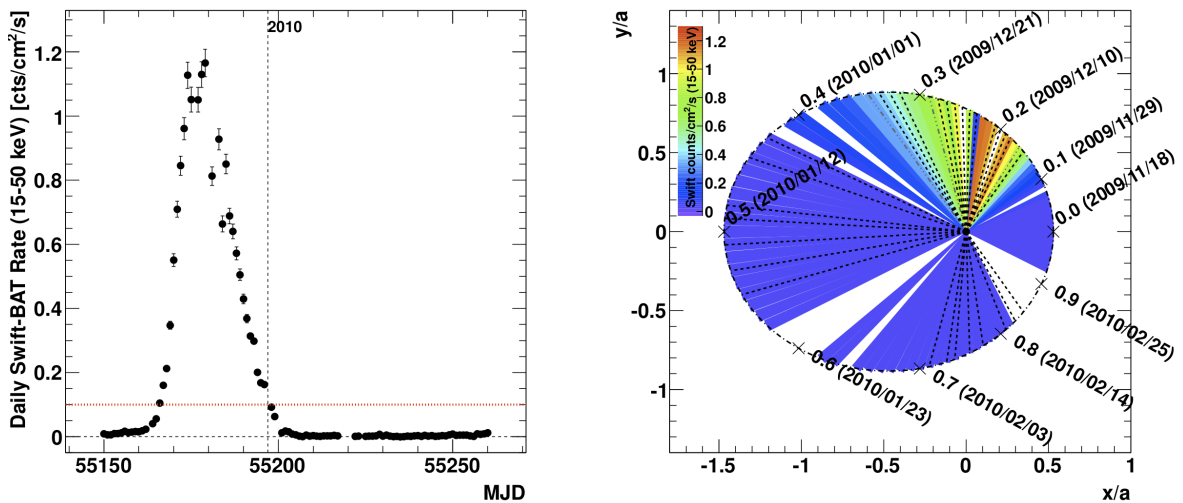
Figure 5.1.: Left: Swift/BAT counting rate vs time in the 15-50 keV energy range. The horizontal line at 0.1 cts/cm^2/s indicates the trigger threshold for observations with VERITAS. Right: Relative orbit of the neutron star around the Be star. The primary star lies in the focus of the ellipse (0,0) and the axis units are multiples of the semi-major axis of the orbit. Note that the inclination of the system is unknown. Indicated in colors is the Swift/BAT counting rate in the 15-50 keV energy range for the orbit starting in November 2009. The dashed lines indicate nights with VERITAS observations, covering the flare, apastron, and periods close to periastron. Orbital parameters after [79].

event selection recommendations from the Fermi Science Support Center[1]. Briefly, we selected photons from the Pass 6 diffuse class events, those that have the highest probability of being gamma rays, with the `gtselect` tool. In order to avoid contamination from Earth albedo photons, time periods when the region around 1A 0535+262 was observed at zenith angles greater than 105° were eliminated from further analysis. We also limited the spectral range to above 200 MeV to reduce contamination by the galactic diffuse gamma-ray background.

---

[1] http://fermi.gsfc.nasa.gov/ssc/data/analysis/scitools/

At low energies, the point spread function (PSF) of the LAT is quite large, so it was necessary to deal with contamination by potential sources in the vicinity of 1A 0535+262. For this reason, a circular region of interest (RoI), centered on 1A 0535+262, was chosen with a radius of 8.5°. We chose a source region of radius 17°, also centered on 1A 0535+262, that encompasses the supernova remnant IC 443, which is 9.5° from 1A 0535+262, and the Geminga pulsar, which is 15.3° away. Both of these sources are known GeV-TeV gamma-ray emitters. IC 443 and Geminga were modeled as described by [89] and [90], respectively. All sources in the 11-month Fermi/LAT catalog [91] inside the source region were considered. The catalog consists of data acquired from 4 August 2008 to 4 July 2009, which in the case of 1A 0535+262 contains data over several orbital periods but before the giant December 2009 outburst. There is no detection for 1A 0535+262 in the catalog. 1A 0535+262 is modeled assuming a fixed spectral index of 2.1 while the normalization is left as a free parameter. The sources were assumed to have a power-law spectrum, which was derived from the fluxes in the Fermi/LAT catalog.

Two differences from the 11-month catalog were encountered during the analysis. First, the source 1FGL J0623.5+3330 possessed a test statistic (TS) value ten times higher than that reported in the Fermi catalog (see [92] for further information on the test statistic). To account for such variability, we left both the normalization and spectral index free. Second, an unidentified source was also found at the position RA 74.12° and Dec 26.99° with a TS value of 68, and it was included in the source model. The spectral parameters were allowed to vary during the fit for sources that lie within the RoI but were fixed for those outside of the RoI (but still inside of the source region). An improvement to the source model fit was achieved when IC 443, which is in the source region, was allowed to vary with free model parameters. Besides discrete sources, contamination by the diffuse background was also taken into account. The galactic and extragalactic backgrounds were represented with *gll_iem_v02.fit* and with a power-law model of index 4.09, respectively. The instrument response function (IRF) used in this analysis is IRF P6_V3_DIFFUSE.

5.1.3 Swift/XRT

For the VERITAS observation of the X-ray binary 1A 0535+262, the XRT was employed to survey the soft X-ray emission over the course of the major X-ray outburst in December, 2009. Triggered by alerts from the BAT, 1A 0535+262 was observed with the XRT between 7 and 27 December, 2009. Table 5.2 provides a summary of the observations, while Figure 5.1 (left) reproduces the hard X-ray light profile during the major outburst. Due to the brightness of the source, the Windowed Timing (WT) mode [93] was adopted to minimize the effects of photon pile-up. The XRT data were reduced and analyzed with FTOOLS in the HEASOFT package version 6.5.[2] For each observation, initial event filtering and selection was carried out using the `xrtpipeline` script, with standard quality cuts, and only events with grades 0-2 were selected as good events. Source counts were extracted, with `xselect`, from a 20×60 pixel rectangular box centered on 1A 0535+262, while background counts were taken from a rectangular region of the same size outside of the source region. An exposure map was generated with `xrtexpomap` and was used to correct for bad columns. Finally, source and background spectra were constructed. The spectra were grouped to contain a minimum of 100 counts per bin and a 1% systematic error was added to the data [94]. To facilitate subsequent spectral analyses, an ancillary response file (`arf`) was produced with `xrtmkarf`, to go along with the adopted response matrix (*swxwt0to2s0_20010101v011.rmf*).

Even in the Windowed Mode, event pile-up was significant in some observations. For instance, near the peak of the outburst (on 8 December, 2009), the pile-up of photons reached about 11%. Therefore, the effects need to be properly accounted for. We adopted a procedure similar to that of [95] to correct the pile-up effects. Briefly, for each observation, we constructed an X-ray spectrum by excluding a central region of the source. We varied the size of the exclusion box until the spectrum was stabilized

---

[2]`http://heasarc.gsfc.nasa.gov/docs/software/lheasoft/`

Table 5.2.   Swift/XRT Observation Log for 1A 0535+262

Obs ID	Start (UT; 2009)	End (UT; 2009)	Exposure Time (sec)	Count Rate[a] (cts s^{-1})
Rising portion of X-ray flare (MJD 55166.4 – 55177.6)				
00035066002	2009-12-07 00:25:13	2009-12-08 00:30:00	981	195
00035066005	2009-12-08 22:46:41	2009-12-08 23:03:21	995	227
00035066006	2009-12-09 16:08:26	2009-12-09 16:28:00	1154	239
00035066007	2009-12-10 10:09:54	2009-12-10 16:28:00	983	234
00035066008	2009-12-11 00:33:44	2009-12-11 00:51:00	985	246
00035066009	2009-12-12 00:42:28	2009-12-12 00:59:00	977	151
Falling portion of X-ray flare (MJD 55178.4 – 55193.6)				
00035066010	2009-12-13 00:46:28	2009-12-13 01:03:00	972	228
00035066011	2009-12-14 00:47:31	2009-12-14 01:04:00	962	242
00035066012	2009-12-15 00:52:43	2009-12-15 01:11:00	1083	242
00035066013	2009-12-16 00:40:25	2009-12-16 00:58:00	1050	240
00035066014	2009-12-18 00:50:32	2009-12-18 01:07:00	943	200
00035066015	2009-12-19 01:16:47	2009-12-19 01:33:00	968	177
00035066017	2009-12-21 01:11:21	2009-12-21 01:28:00	992	182
00035066018	2009-12-22 09:13:48	2009-12-22 09:35:00	1252	163
00035066020	2009-12-23 09:26:21	2009-12-23 09:45:00	1105	145
00035066021	2009-12-24 09:24:36	2009-12-24 09:42:00	1029	133
00035066022	2009-12-25 08:11:28	2009-12-25 08:31:00	1123	98
00035066023	2009-12-26 08:14:49	2009-12-26 08:35:00	1199	109
00035066024	2009-12-27 08:21:56	2009-12-27 08:41:00	1137	103

[a]Background-subtracted count rates in the 0.6–10.0 keV band. They are not pile-up corrected.

(based on the results of spectral fitting). After the procedure, the remaining pile-up effects on the spectrum are expected to be minimal.

5.1.4   RXTE/PCA

Besides the ASM, RXTE carries two pointed instruments: the *Proportional Counter Array* (PCA) and the *High Energy X-ray Timing Experiment* (HEXTE). For this

work only data from the PCA were employed. Operational constraints often require that some of the PCUs be turned off, but PCU 2 was always in operation for our observations during the outburst.

1A 0535+262 was observed by RXTE between 4 December, 2009 and 4 January, 2010. Table 5.3 shows an observation log. We reduced the data using FTOOLS in the HEASOFT package (version 6.5)[3]. The PCA has numerous data modes, and multiple modes are usually employed in an observation. For this work, however, we only used the *Standard 2* data. For a given observation, we first filtered data by following the standard procedure[4], which resulted in a list of good time intervals (GTIs). We then simulated background events for the observation by using the latest background model (*pca_bkgd_cmbrightvle_eMv20051128.mdl*) that is appropriate for bright sources. Using the GTIs, we proceeded to make a spectrum for PCU 2 by using data from only the first xenon layer (which is most accurately calibrated), which limits the spectral coverage to below 25–30 keV. Since few counts were detected at higher energies, the impact of the reduced spectral coverage was very minimal. The selected energy range is below the range where 1A 0535+262 produces cyclotron lines, which are due to the first and second harmonic cyclotron absorption at ~ 45 keV and ~ 100 keV [96,97]. We repeated the steps to derive a corresponding background spectrum for PCU 2 from the simulated events. We added 1% systematic uncertainty to the spectra for subsequent spectral modeling to account for the uncertainty in the instrumental response [98].

5.2 Results

5.2.1 VERITAS

Analysis results for the combined VERITAS data set can be found in Table 5.4. Figure 5.2 shows the region of the sky around 1A 0535+262 as seen by VERITAS.

---

[3]http://heasarc.gsfc.nasa.gov/docs/software/lheasoft/
[4]See the online RXTE Cook Book at:
http://heasarc.gsfc.nasa.gov/docs/xte/recipes/cook_book.html

Table 5.3.   RXTE/PCA Observation Log for 1A 0535+262

Event ID	Start Time (UT)	Stop Time (UT)	Exposure Time (sec)
Rising portion of X-ray flare (MJD 55166.4 – 55177.6)			
94323-04-01-01	2009-12-04 10:27:12	2009-12-04 11:23:44	2448
94323-04-01-00	2009-12-05 16:14:24	2009-12-05 17:58:40	3152
94323-04-01-02	2009-12-06 12:36:32	2009-12-06 13:46:56	3200
94323-04-01-03	2009-12-07 13:45:20	2009-12-07 14:57:36	3232
94323-04-01-04	2009-12-08 14:45:36	2009-12-08 15:55:28	2896
94323-04-01-05	2009-12-09 17:25:20	2009-12-09 18:48:32	3120
94323-04-01-06	2009-12-10 16:55:12	2009-12-10 21:27:28	9952
94323-04-02-00	2009-12-11 11:57:20	2009-12-11 12:59:28	2832
94323-04-02-01	2009-12-12 13:04:16	2009-12-12 14:33:36	2944
Falling portion of X-ray flare (MJD 55178.4 – 55193.6)			
94323-04-02-02	2009-12-13 07:55:12	2009-12-13 08:42:40	2064
94323-04-02-04	2009-12-14 18:29:20	2009-12-14 19:41:36	3376
94323-05-01-00	2009-12-15 14:36:16	2009-12-15 16:05:36	3392
94323-05-01-01	2009-12-16 11:22:24	2009-12-16 12:28:32	3328
94323-05-01-02	2009-12-17 15:14:24	2009-12-17 16:46:40	3392
94323-05-02-03	2009-12-18 14:50:24	2009-12-18 16:30:40	3328
94323-05-02-00	2009-12-19 09:22:24	2009-12-19 13:03:28	6864
94323-05-02-06	2009-12-19 14:25:20	2009-12-19 17:27:28	6720
94323-05-02-04	2009-12-20 12:26:24	2009-12-20 15:35:28	6624
94323-05-02-01	2009-12-21 07:46:24	2009-12-21 10:25:36	4528
94323-05-02-02	2009-12-23 11:03:12	2009-12-23 15:54:40	9920
94323-05-02-05	2009-12-24 10:59:40	2009-12-24 14:50:40	7664
94323-05-03-00	2009-12-25 15:27:28	2009-12-25 16:32:48	2704
94323-05-03-01	2009-12-26 11:26:24	2009-12-26 16:03:44	9072
94323-05-03-02	2009-12-27 14:29:36	2009-12-27 15:34:40	9920
94323-05-03-03	2009-12-28 17:19:28	2009-12-28 19:32:32	3328
Apastron (MJD 55199.4 – 55216.6)			
94323-05-04-00	2010-01-02 01:51:12	2010-01-02 03:31:28	2832
94323-05-04-01	2010-01-04 00:58:24	2010-01-04 02:15:28	3136
94323-05-04-02	2010-01-07 02:36:16	2010-01-07 03:56:32	3008
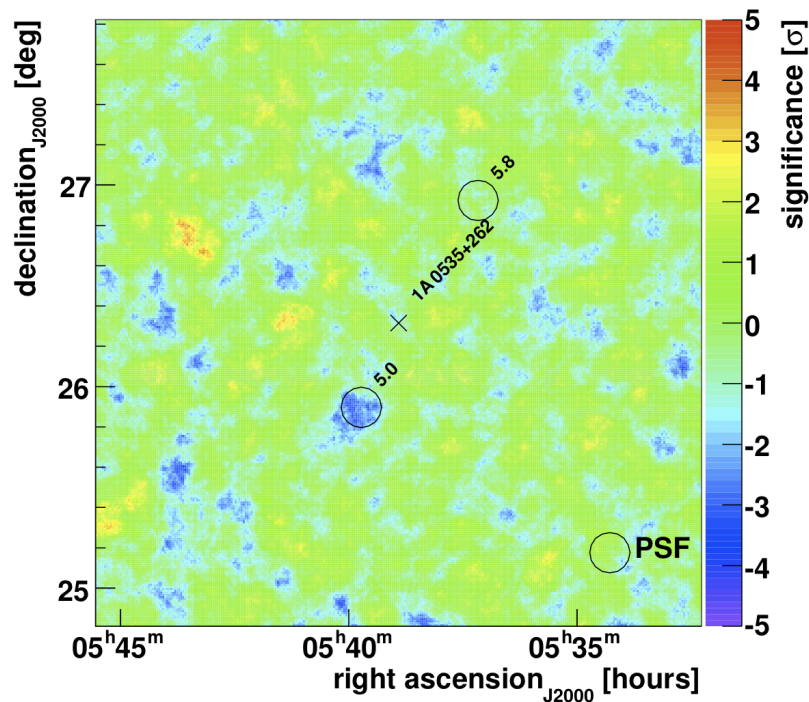
Figure 5.2.: VERITAS significance map of the region around 1A 0535+262 in equatorial coordinates for the period MJD 57166-55250. The location of 1A 0535+262 is indicated by a black cross at the center. Also shown are regions excluded from the background calculation due to bright stars. The numbers beside the excluded regions indicate the B magnitude of these stars. The circle at the bottom right indicates the angular resolution of the VERITAS observations.

No evidence for VHE gamma rays has been found. The flux upper limit at the 99% confidence level [99] assuming a power-law-like source spectrum with a spectral index of $\Gamma = 2.5$ is $F(> 0.3 \text{ TeV}) < 0.5 \times 10^{-12}$ ph cm^{-2} s^{-1} (about 0.4% of the flux of the Crab Nebula above 0.3 TeV).

The data were arranged in different periods, as gamma-ray production and absorption is expected to vary with orbital movement and flaring state. The four periods are: rising portion and falling portion of the giant flare, apastron and periastron. No VHE emission has been detected in any of these periods; upper limits between 0.9

Table 5.4.   VERITAS Analysis Results for 1A 0535+262

Period	MJD Range	Observation Time (min)	Elevation Range	On Events	Off Events	alpha	Excess Events	Significance (σ)	Flux Upper Limit (10^{-12} cm^{-2} s^{-1})
All	57166 − 55249	1420	48º − 85º	86	801	0.13	-15.8	-1.5	0.5
Rising portion	55166 − 55178	305	48º − 85º	19	184	0.13	-4.5	-0.9	1.3
Falling portion	55178 − 55193	501	49º − 78º	33	343	0.13	-10.7	-1.6	0.9
Apastron	55199 − 55216	323	57º − 81º	16	161	0.13	-4.5	-1.0	1.0
Periastron	55230 − 55249	289	54º − 85º	18	113	0.13	3.7	0.9	2.0

Note. — Upper limits (E> 0.3 TeV) are given at 99% confidence level (after [99]). Significances are calculated using equation (17) from [35].

Table 5.5.   Fermi/LAT Analysis Results for 1A 0535+262

Period	MJD Range	Exposure Time (sec)	Significance[a] (TS)	Flux Upper Limit[b] (10^{-8} cm^{-2} s^{-1})
All	55165.9 − 55249.1	3125089	0.0	1.9
Rising portion of X-ray flare	55165.9 − 55177.6	429518	0.0	6.4
Falling portion of X-ray flare	55178.4 − 55193.6	515688	0.3	9.8
Apastron	55199.4 − 55216.6	725252	0.0	6.8
Periastron	55230.4 − 55249.6	667580	0.0	5.0

[a]The definition of the test statistic is given by equation (20) of [92].

[b]The upper limits are given at the 99% confidence level, for photon energies above 0.2 GeV.

and 2.0% of the flux of the Crab Nebula (> 0.3 TeV) have been derived. For details, see Table 5.4.

5.2.2   Fermi/LAT

A search for HE gamma-ray emission from 1A 0535+262 was performed for a period that spans the onset of the X-ray outburst to the successive apastron of the

pulsar (30 November, 2009 – 22 February, 2010). No significant gamma-ray excess was seen for the same time intervals used for the VERITAS data analysis. We derived a flux upper limit of $F(> 0.2 \text{ GeV}) < 1.9 \times 10^{-8}$ ph cm^{-2} s^{-1} at the 99% confidence level. To facilitate a comparison with theoretical models, we also derived flux upper limits for different periods of the X-ray outburst (rising and decaying portions) and around apastron and periastron passages. The results are summarized in Table 5.5.

5.2.3 Swift/XRT

The XRT spectrum for each time interval was modeled in XSPEC version 12.6.0k. We used response matrix file (`rmf`) v011, along with the `arf` that we made. During spectral fitting, we limited the energy range to 0.6-10.0 keV, to avoid complicated calibration issues at the lower energies. We should note the presence of two absorption features, at 1.8 and 2.2 keV, respectively, which are probably of instrumental origin as they lie near the Si K and Au M edges.[5]. They were modeled with inverted Gaussians at fixed energies in the spectral modeling.

We fitted the spectra with a model that consists of a blackbody and a power law, both of which are absorbed by foreground matter in the interstellar medium. Good fits were achieved in all cases. The results are shown in Table 5.6. Spectral hardening during the rising phase of the X-ray outburst is apparent. The reverse trend is noticeable during the decaying phase. We note that the rising phase corresponds to orbital phases 0.11–0.21 and the decaying phase to orbital phases 0.22–0.36.

5.2.4 RXTE/PCA

Similarly, we modeled the PCA spectra in XSPEC. We limited the energy range to >3 keV, to avoid calibration issues at lower energies. Due to the lack of sensitivity at low energies, for each observation we fixed the hydrogen column density N_H to $3.0 \times$

---

[5]http://heasarc.gsfc.nasa.gov/docs/heasarc/caldb/swift/docs/xrt/
SWIFT-XRT-CALDB-09_v14.pdf

Table 5.6.   Swift/XRT Spectral Results for 1A 0535+262

Obs ID	N_H $(10^{22}$ cm$^{-2})$	kT_{bb} (keV)	N_{bb}[a]	Γ	N_Γ[b]	χ^2_ν/ν
Rising portion of X-ray flare (MJD 55166.4 – 55177.6)						
00035066002	$0.3^{+0.1}_{-0.1}$	$2.2^{+0.2}_{-0.3}$	$0.2^{+0.1}_{-0.1}$	$0.9^{+0.4}_{-0.2}$	$0.2^{+0.1}_{-0.1}$	1.04/536
00035066005	$0.3^{+0.1}_{-0.1}$	$2.2^{+0.1}_{-0.1}$	$0.3^{+0.1}_{-0.1}$	$1.2^{+0.4}_{-0.3}$	$0.7^{+0.2}_{-0.1}$	1.05/513
00035066006	$0.3^{+0.1}_{-0.1}$	$2.4^{+0.2}_{-0.3}$	$0.2^{+0.1}_{-0.1}$	$1.0^{+0.2}_{-0.2}$	$1.0^{+0.2}_{-0.2}$	1.06/540
00035066007	$0.8^{+0.4}_{-0.3}$	$2.3^{+0.4}_{-0.7}$	$0.2^{+0.2}_{-0.2}$	$0.8^{+0.4}_{-0.3}$	$1.0^{+0.2}_{-0.2}$	1.19/545
00035066008	$0.3^{+0.1}_{-0.1}$	$2.4^{+0.6}_{-1.3}$	$0.2^{+0.3}_{-0.1}$	$0.6^{+0.5}_{-0.2}$	$1.0^{+0.2}_{-0.2}$	1.13/513
00035066009	$0.3^{+0.2}_{-0.1}$	$2.2^{+0.5}_{-0.4}$	$0.2^{+0.2}_{-0.1}$	$0.6^{+0.4}_{-0.2}$	$0.9^{+0.3}_{-0.2}$	1.10/526
Falling portion of X-ray flare (MJD 55178.4 – 55193.6)						
00035066010	$0.1^{+0.2}_{-0.1}$	$2.0^{+0.3}_{-0.3}$	$0.2^{+0.1}_{-0.1}$	$0.7^{+0.6}_{-0.3}$	$0.6^{+0.4}_{-0.2}$	1.11/330
00035066011	$0.2^{+0.4}_{-0.1}$	$2.5^{+0.5}_{-0.9}$	$0.2^{+0.3}_{-0.1}$	$0.7^{+0.8}_{-0.5}$	$0.9^{+0.7}_{-0.4}$	1.05/488
00035066012	$0.2^{+0.1}_{-0.1}$	$2.2^{+0.1}_{-0.2}$	$0.4^{+0.1}_{-0.1}$	$1.1^{+0.3}_{-0.4}$	$0.8^{+0.3}_{-0.2}$	1.01/517
00035066013	$0.3^{+0.2}_{-0.1}$	$2.2^{+0.1}_{-0.2}$	$0.3^{+0.1}_{-0.1}$	$1.1^{+0.4}_{-0.3}$	$0.9^{+0.5}_{-0.2}$	1.07/550
00035066014	$0.5^{+0.2}_{-0.2}$	$2.4^{+0.1}_{-0.1}$	$0.38^{+0.03}_{-0.06}$	$1.8^{+0.6}_{-0.6}$	$1.4^{+1.0}_{-0.6}$	0.99/491
00035066015	$0.4^{+0.2}_{-0.1}$	$2.0^{+0.1}_{-0.1}$	$0.19^{+0.03}_{-0.04}$	$1.6^{+0.5}_{-0.4}$	$1.0^{+0.6}_{-0.3}$	1.07/506
00035066017	$0.4^{+0.1}_{-0.1}$	$2.1^{+0.1}_{-0.2}$	$0.2^{+0.1}_{-0.1}$	$1.2^{+0.5}_{-0.4}$	$0.9^{+0.2}_{-0.4}$	0.97/528
00035066018	$0.3^{+0.1}_{-0.1}$	$2.1^{+0.2}_{-0.3}$	$0.1^{+0.1}_{-0.1}$	$0.9^{+0.4}_{-0.2}$	$0.7^{+0.2}_{-0.1}$	1.13/547
00035066020	$0.5^{+0.3}_{-0.2}$	$2.2^{+0.1}_{-0.3}$	$0.16^{+0.04}_{-0.07}$	$1.4^{+0.7}_{-0.5}$	$0.8^{+0.7}_{-0.3}$	1.15/361
00035066021	$0.2^{+0.2}_{-0.1}$	$1.8^{+0.8}_{-0.2}$	$0.09^{+0.03}_{-0.02}$	$0.9^{+0.4}_{-0.3}$	$0.3^{+0.2}_{-0.1}$	1.05/369
00035066022	$0.2^{+0.1}_{-0.1}$	$1.7^{+0.1}_{-0.1}$	$0.07^{+0.02}_{-0.01}$	$1.1^{+0.5}_{-0.3}$	$0.2^{+0.1}_{-0.1}$	0.90/407
00035066023	$1.0^{+0.1}_{-0.1}$	$1.7^{+0.2}_{-0.1}$	$0.06^{+0.01}_{-0.01}$	$0.7^{+0.2}_{-0.2}$	$0.20^{+0.07}_{-0.04}$	1.02/489
00035066024	$0.2^{+0.3}_{-0.2}$	$1.7^{+0.1}_{-0.1}$	$0.07^{+0.03}_{-0.01}$	$0.7^{+0.4}_{-0.1}$	$0.3^{+0.3}_{-0.1}$	1.13/333

Note. — The columns are: hydrogen column density (N_H), blackbody temperature (T_{bb}), blackbody normalization (N_{bb}), photon index (Γ), power-law normalization (N_Γ), reduced χ^2_ν and degrees of freedom ν.

[a]In units of erg s^{-1} kpc^{-2}

[b]In units of ph cm^{-2}s^{-1}keV^{-1}

10^{21} cm^{-2}, which is fairly representative of the values derived from the Swift/XRT observation (see Table 5.6). We found that the simple model that had worked well for the Swift/XRT spectra could no longer satisfactorily fit the PCA spectra. Examining the residuals, we noted the presence of a broad feature between 6 and 7 keV, which is likely caused by calibration uncertainty near the Xe L edge, although it could also be partially attributable to a K$_\alpha$ line of neutral or ionized iron. We modeled it with a Gaussian and will not discuss it further. More interestingly, we found that we could achieve good fits to the PCA spectra by introducing a high-energy cut-off.

The roll-over of the spectrum at high energies seems to suggest a physical origin of the hard X-ray emission in thermal inverse Compton scattering. The broad spectral coverage of the RXTE/PCA allows modeling of the X-ray spectrum with a more physical model. We replaced the empirical power law (with a high-energy cut-off) with the *comptt* model in XSPEC. Table 5.7 summarizes the results. The fits are all excellent. Due to the lack of sensitivity of the PCA at low energies, however, the seed photon temperatures (kT_s) is not well constrained. This also affects other parameters, such as the normalization of *comptt*, because of the coupling between the spectral components.

5.2.5   Joint Swift/RXTE Analysis for 1A 0535+262

Ideally we would combine both the Swift/XRT and RXTE/PCA data to constrain all spectral components. Unfortunately there were no simultaneous observations, but there were many sets of observations from both satellites which occurred within the timescale of a day. The average energy flux would vary around $\sim$1 keV cm^{-2} s^{-1} per day during the maximum X-ray outburst. We attempted to model these pairs of Swift/XRT and RXTE/PCA observations jointly, with the understanding that the source could have varied spectrally between the two. To account for possible discrepancy in the overall throughput between the XRT and PCA, we introduced a

Table 5.7.   RXTE/PCA Spectral Results for 1A 0535+262

Observation ID	kT_{bb} (keV)	N_{bb}[a]	kT_s (keV)	kT_e (keV)	τ	N_{comp}	χ^2_ν/ν
Rising portion of X-ray flare (MJD 55166.4 – 55177.6)							
94323-04-01-01	$2.0^{+0.3}_{-0.2}$	$0.03^{+0.01}_{-0.01}$	$0.4^{+0.2}_{-0.4}$	$6.3^{+0.3}_{-0.2}$	$8.1^{+0.6}_{-0.5}$	$0.4^{+0.7}_{-0.4}$	0.41/40
94323-04-01-00	$2.3^{+0.8}_{-0.3}$	$0.04^{+0.02}_{-0.01}$	$0.3^{+0.4}_{-0.3}$	$6.5^{+0.6}_{-0.2}$	$7.9^{+0.6}_{-0.7}$	$0.7^{+1.1}_{-0.2}$	0.23/40
94323-04-01-02	$2.8^{+1.2}_{-0.6}$	$0.07^{+0.11}_{-0.02}$	$0.6^{+1.1}_{-0.6}$	$6.7^{+1.8}_{-0.4}$	$7.7^{+0.9}_{-1.6}$	$0.6^{+1.4}_{-0.1}$	0.22/40
94323-04-01-03	$2.3^{+0.6}_{-0.3}$	$0.08^{+0.03}_{-0.01}$	$0.3^{+0.4}_{-0.3}$	$6.5^{+0.5}_{-0.2}$	$8.6^{+0.7}_{-0.7}$	$1.0^{+1.3}_{-0.2}$	0.23/40
94323-04-01-04	$2.3^{+0.6}_{-0.2}$	$0.09^{+0.02}_{-0.01}$	$0.3^{+0.3}_{-0.3}$	$6.5^{+0.4}_{-0.2}$	$9.0^{+0.8}_{-0.8}$	$1.0^{+1.3}_{-0.1}$	0.28/40
94323-04-01-05	$2.2^{+0.4}_{-0.2}$	$0.09^{+0.01}_{-0.02}$	$0.4^{+0.3}_{-0.4}$	$6.4^{+0.3}_{-0.2}$	$9.3^{+0.7}_{-0.7}$	$1.2^{+1.3}_{-0.1}$	0.16/40
94323-04-01-06	$2.2^{+0.4}_{-0.2}$	$0.09^{+0.01}_{-0.02}$	$0.4^{+0.2}_{-0.4}$	$6.4^{+0.3}_{-0.2}$	$9.3^{+0.7}_{-0.7}$	$1.1^{+1.2}_{-0.1}$	0.16/40
94323-04-02-00	$2.3^{+0.4}_{-0.2}$	$0.09^{+0.02}_{-0.02}$	$0.4^{+0.2}_{-0.4}$	$6.5^{+0.3}_{-0.2}$	$9.1^{+0.7}_{-0.7}$	$1.1^{+1.4}_{-0.1}$	0.25/40
94323-04-02-01	$2.4^{+0.7}_{-0.3}$	$0.10^{+0.04}_{-0.02}$	$0.4^{+0.2}_{-0.4}$	$6.5^{+0.5}_{-0.2}$	$9.0^{+0.7}_{-0.8}$	$1.2^{+1.5}_{-0.2}$	0.22/40
Falling portion of X-ray flare (MJD 55178.4 – 55193.6)							
94323-04-02-02	$2.3^{+0.5}_{-0.2}$	$0.10^{+0.02}_{-0.02}$	$0.4^{+0.2}_{-0.4}$	$6.5^{+0.3}_{-0.2}$	$9.3^{+0.7}_{-0.7}$	$1.2^{+1.4}_{-0.1}$	0.25/40
94323-04-02-04	$2.3^{+0.5}_{-0.2}$	$1.10^{+0.02}_{-0.02}$	$0.4^{+0.2}_{-0.4}$	$6.5^{+0.4}_{-0.2}$	$9.2^{+0.7}_{-0.7}$	$1.2^{+1.4}_{-0.2}$	0.26/40
94323-05-01-00	$2.2^{+0.4}_{-0.2}$	$0.09^{+0.01}_{-0.01}$	$0.4^{+0.2}_{-0.4}$	$6.4^{+0.3}_{-0.2}$	$9.4^{+0.7}_{-0.7}$	$1.1^{+1.3}_{-0.1}$	0.22/40
94323-05-01-01	$2.2^{+0.6}_{-0.2}$	$0.08^{+0.01}_{-0.01}$	$0.4^{+0.2}_{-0.4}$	$6.4^{+0.3}_{-0.2}$	$9.2^{+0.6}_{-0.8}$	$1.1^{+1.3}_{-0.1}$	0.24/40
94323-05-01-02	$2.3^{+0.6}_{-0.3}$	$0.08^{+0.02}_{-0.01}$	$0.4^{+0.3}_{-0.4}$	$6.4^{+0.4}_{-0.2}$	$9.1^{+0.8}_{-0.8}$	$1.1^{+1.3}_{-0.1}$	0.24/40
94323-05-02-03	$2.2^{+0.4}_{-0.2}$	$0.07^{+0.01}_{-0.01}$	$0.4^{+0.2}_{-0.4}$	$6.4^{+0.3}_{-0.2}$	$9.2^{+0.7}_{-0.7}$	$0.9^{+1.2}_{-0.1}$	0.22/40
94323-05-02-00	$2.2^{+0.4}_{-0.2}$	$0.07^{+0.10}_{-0.01}$	$0.4^{+0.3}_{-0.4}$	$6.4^{+0.3}_{-0.2}$	$9.0^{+0.7}_{-0.6}$	$0.9^{+1.1}_{-0.1}$	0.15/40
94323-05-02-06	$2.2^{+0.6}_{-0.2}$	$0.06^{+0.01}_{-0.01}$	$0.4^{+0.3}_{-0.4}$	$6.4^{+0.3}_{-0.2}$	$8.9^{+0.7}_{-0.6}$	$0.9^{+1.2}_{-0.1}$	0.20/40
94323-05-02-04	$2.1^{+0.5}_{-0.2}$	$0.05^{+0.01}_{-0.01}$	$0.3^{+0.4}_{-0.3}$	$6.4^{+0.3}_{-0.2}$	$8.9^{+0.7}_{-0.7}$	$0.9^{+1.1}_{-0.1}$	0.17/40
94323-05-02-01	$2.1^{+0.4}_{-0.2}$	$0.05^{+0.01}_{-0.01}$	$0.4^{+0.3}_{-0.4}$	$6.4^{+0.3}_{-0.2}$	$8.9^{+0.6}_{-0.5}$	$0.8^{+1.0}_{-0.1}$	0.14/40
94323-05-02-02	$2.1^{+0.5}_{-0.2}$	$0.04^{+0.08}_{-0.07}$	$0.3^{+0.3}_{-0.3}$	$6.4^{+0.3}_{-0.2}$	$8.4^{+0.6}_{-0.5}$	$0.7^{+1.0}_{-0.1}$	0.15/40
94323-05-02-05	$2.1^{+0.4}_{-0.2}$	$0.03^{+0.01}_{-0.01}$	$0.4^{+0.3}_{-0.4}$	$6.4^{+0.3}_{-0.2}$	$8.4^{+0.6}_{-0.5}$	$0.6^{+0.9}_{-0.1}$	0.17/40
94323-05-03-00	$2.1^{+0.5}_{-0.2}$	$0.03^{+0.01}_{-0.01}$	$0.3^{+0.4}_{-0.3}$	$6.4^{+0.3}_{-0.2}$	$8.4^{+0.7}_{-0.6}$	$0.6^{+0.9}_{-0.1}$	0.30/40
94323-05-03-01	$2.0^{+0.3}_{-0.1}$	$0.03^{+0.01}_{-0.01}$	$0.4^{+0.2}_{-0.4}$	$6.2^{+0.2}_{-0.1}$	$8.5^{+0.5}_{-0.5}$	$0.44^{+0.73}_{-0.04}$	0.20/40
94323-05-03-02	$2.0^{+0.4}_{-0.2}$	$0.01^{+0.01}_{-0.01}$	$0.4^{+0.3}_{-0.4}$	$6.2^{+0.3}_{-0.2}$	$8.3^{+0.7}_{-0.5}$	$0.4^{+0.6}_{-0.1}$	0.20/40
94323-05-03-03	$2.0^{+0.4}_{-0.2}$	$0.02^{+0.01}_{-0.01}$	$0.3^{+0.4}_{-0.3}$	$6.1^{+0.3}_{-0.2}$	$8.2^{+0.7}_{-0.6}$	$0.4^{+0.6}_{-0.1}$	0.20/40
Apastron (MJD 55199.4 – 55216.6)							
94323-05-04-00	$1.9^{+0.4}_{-0.2}$	$0.007^{+0.002}_{-0.002}$	$0.4^{+0.2}_{-0.4}$	$6.3^{+0.4}_{-0.2}$	$6.9^{+0.5}_{-0.5}$	$0.15^{+0.43}_{-0.02}$	0.61/40
94323-05-04-01	$1.8^{+0.7}_{-0.2}$	$0.004^{+0.002}_{-0.001}$	$0.4^{+0.3}_{-0.4}$	$6.4^{+0.7}_{-0.4}$	$6.3^{+0.6}_{-0.7}$	$0.09^{+0.13}_{-0.02}$	0.61/40
94323-05-04-02	$2.6^{+1.2}_{-1.0}$	$0.002^{+0.001}_{-0.001}$	$0.6^{+0.1}_{-0.6}$	$3.4^{+2.3}_{-1.2}$	$3.6^{+1.7}_{-2.5}$	$0.2^{+0.1}_{-0.2}$	0.67/40

Note. — The parameters for the Compton component are: seed photon temperature (T_s), electron temperature (T_e), optical depth (τ), and normalization (N_{comp}). The geometry parameter is frozen at 0.8, and N_H is fixed at 0.3×10^{22} cm^{-2}.

[a]In units of erg s^{-1} kpc^{-2}

multiplicative constant to the models. We fixed the constant to unity for the XRT but let it float for the PCA.

We experimented with several physical models to gain further insights into the origin of the observed spectral roll-over at high energies, including thermal Comptonization (*comptt*), thermal Bremsstrahlung (*bremss*), and non-thermal synchrotron (*srcut*), in combination with other spectral components that were used in the modeling of the Swift/XRT and RXTE/PCA data (mainly at lower energies). We were not able to find any acceptable fits when we tied all of the physical parameters in the model for the Swift/XRT and RXTE/PCA observations, but when we untied the blackbody parameters (i.e., let them vary independently for the Swift/XRT and RXTE/PCA observations), we obtained a good fit only with the thermal Comptonization model (for hard X-ray emission). This is perhaps an indication that the source did indeed vary significantly between the two observations and seems to indicate that the hard X rays are likely of thermal origin. Figure 5.3 shows an example (for the rising portion; see Table 5.8) of the fits and residuals for cases where the blackbody parameters are tied and untied, respectively. The results are summarized in Table 5.8.

5.3 Summary & Discussion

We present observations at X-ray and gamma-ray energies of the Be/pulsar binary 1A 0535+262 during its 2009 giant outburst. The results can be summarized as follows:

1. There is no evidence for VHE or HE emission from 1A 0535+262 in the VERITAS and Fermi/LAT observations during the giant outburst and during the subsequent apastron and periastron passages;

2. The X-ray spectra measured with the Swift/XRT and RXTE/PCA are best fitted with a model that consists of blackbody and Comptonized emission from thermal electrons at temperatures of approximately 2 keV and 6 keV, respectively.
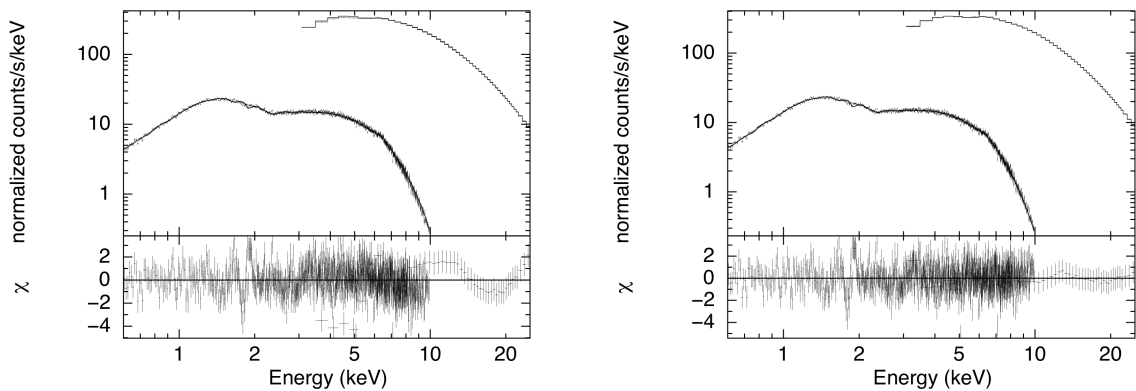
Figure 5.3.: Joint Swift/XRT and RXTE/PCA spectral modeling of 1A 0535+262 for the rising portion of the X-ray outburst. The upper panel shows the Swift/XRT data (lower curve) and the RXTE/PCA data (upper curve), and the lower panel shows the residuals of the fit. Left: A fit to the data with a model that consists of blackbody radiation and thermal Comptonization, with all physical parameters tied for the XRT and PCA data sets. Note a significant pattern in the residuals of the fit (shown in the bottom panel) in the PCA band. Right: A fit to the data with the same model but with the blackbody temperature and normalization untied between the two data sets.

The optically-thick emission may originate from the accretion disk around the neutron star and perhaps also from the "hot spot" on the neutron star surface. The optical depths for the Compton component are ~10 (see Table 5.8). This emission component may be associated with, e.g., a warm layer of the accretion disk or with the accretion column above the "hot spot".

The non-detection of 1A 0535+262 at VHE and HE wavelengths may indicate that there is no significant non-thermal particle population in the system. This would imply a thermal origin of the X-ray emission, as opposed to a non-thermal leptonic model, in which X-ray emission is the result of synchrotron radiation from non-thermal electrons. A thermal origin is also supported by the fact that 1A 0535+262

has not been detected at radio wavelengths [100, 101], which also suggests the lack of non-thermal electrons, as well as by the OSSE/CGRO observation of the source that saw no significant non-thermal component [102].

The upper limits derived from VERITAS observations correspond to a luminosity of $< 0.5 - 1.5 \times 10^{33}$ erg s^{-1} (see Table 5.4), assuming a distance to 1A 0535+262 of 2 kpc. Applying the Cheng and Ruderman mechanism to the source, Orellana et al. (2007) derived a gamma-ray luminosity of about 10^{33} erg s^{-1} at 0.3 TeV at the end of giant outbursts [103], which is very close to our upper limits. The Fermi/LAT flux upper limit over the whole orbit (see Table 5.5) is already below the theoretical flux prediction of 3.8×10^{-8} ph cm^{-2} s^{-1}, which was derived by extrapolating the result of [103] to the Fermi/LAT energy range. Therefore, our results begin to place severe constraints on hadronic models as well. We note that the upper limits correspond only to a tiny fraction of the Eddington luminosity of the system. In comparison, the X-ray luminosity of 1A 0535+262 can reach about 10% of the Eddington luminosity.

One of the main interests in 1A 0535+262 stems from the previous EGRET gamma-ray source detection before the February 1994 major X-ray outburst peak. There is no Fermi detection for the EGRET source 3EG J0542+2160, and a 99% confidence level flux upper limit at the source location (RA 85.69°, Dec 26.17°) produces a value of F(> 0.2GeV)$< 3.5 \times 10^{-8}$ ph cm^2 s^{-1} (test statistic TS is 1.0), for the same source model settings and energy range used for 1A 0535+262 over the whole orbital period. 1FGL J0538.6+2717, the closest catalog source to 1A 0535+262, is 0.98° away and doesn't overlap with the 95% confidence level location radius of 3EG J0542+2610.

The lack of detectable gamma-ray emission may also be attributed to the attenuation of gamma rays via pair production, because of the presence of a strong radiation field in the binary system at both optical and X-ray wavelengths. The VHE gamma rays should be attenuated mainly by IR photons from the companion (Oe) star and are thus expected to be modulated by the orbital motion [104]. However, quantifying the effects of attenuation is complicated by dramatic changes in the accretion rate

that are associated with the giant outburst, since the accretion process could also be a source of IR photons and, more importantly, could power the VHE gamma-ray production. In other words, there is significant degeneracy in the production and attenuation of VHE gamma rays. It is worth noting that the secondary electrons (and positrons) from the pair production process could be a source of gamma rays at MeV–GeV energies [104]. The HE gamma rays can be similarly attenuated, mainly by soft X-ray photons. We therefore do not expect to detect such gamma rays near the peak of the X-ray outburst. However, the fact that 1A 0535+262 is not detected with the Fermi/LAT when the attenuation of HE photons is not expected to be significant seems to indicate a genuine lack of gamma-ray production.

Our results seem to suggest that 1A 0535+262 is inherently different from those Be X-ray binaries that have been detected at GeV–TeV energies, including PSR B1259–63 and LS I +61°303, in terms of gamma-ray production. Physically, while the nature of the compact object in LS I +61°303 is still uncertain, PSR B1259–63 contains a rapidly rotating pulsar with a much lower spin period than 1A 0535+262. These two systems present more extreme physical conditions than 1A 0535+262, but equally extreme physical conditions exists in systems which are also undetected in gamma rays. The environmental conditions which lead to gamma-ray production in binary systems remain poorly defined. To more meaningfully constrain theoretical models on gamma-ray production in 1A 0535+262, we would probably need to lower the VHE gamma-ray upper limits by an order of magnitude. This source represents the archetype of the class of Be binary systems which exhibit giant outbursts and the VHE observations were the best we could hope to get in terms of coverage and exposure. The source will be a good target for the next-generation ground-based gamma-ray observatories.

Table 5.8: Joint Swift/RXTE Spectral Fits for 1A 0535+262

	N_H	kT_{bb}	$N_{bb}{}^\dagger$	kT_{bb}	$N_{bb}{}^\dagger$	kT_s	kT_e	τ	N_{comp}	χ^2_ν/ν
	$10^{22}\,\mathrm{cm}^{-2}$	(keV)		(keV)		(keV)	(keV)			
		Swift		RXTE						
Rising portion	$0.34^{+0.01}_{-0.02}$	$1.95^{+0.06}_{-0.07}$	$0.27^{+0.01}_{-0.03}$	$2.02^{+0.16}_{-0.12}$	$0.08^{+0.02}_{-0.02}$	$0.11^{+0.05}_{-0.11}$	$6.3^{+0.2}_{-0.1}$	$9.5^{+0.6}_{-0.5}$	$1.20^{+0.83}_{-0.10}$	$1.18/851$
	$0.33^{+0.01}_{-0.01}$		$1.65^{+0.03}_{-0.03}\ddagger$	$0.168^{+0.007}_{-0.006}\ddagger$		$0.132^{+0.04}_{-0.13}$	$5.87^{+0.07}_{-0.07}$	$12.31^{+0.2}_{-0.6}$	$1.6^{+0.7}_{-0.1}$	$1.44/853$
Falling portion	$0.33^{+0.01}_{-0.01}$	$1.94^{+0.05}_{-0.04}$	$0.118^{+0.006}_{-0.006}$	$2.33^{+0.58}_{-0.26}$	$0.017^{+0.203}_{-0.004}$	$0.06^{+0.18}_{-0.06}$	$6.5^{+0.3}_{-0.2}$	$8.0^{+0.4}_{-0.5}$	$0.5^{+0.3}_{-0.1}$	$1.32/881$
	$0.24^{+0.03}_{-0.03}$		$1.49^{+0.02}_{-0.02}\ddagger$	$0.071^{+0.002}_{-0.002}\ddagger$		$0.23^{+0.04}_{-0.04}$	$5.67^{+0.05}_{-0.05}$	$12.70^{+0.3}_{-0.4}$	$0.52^{+0.02}_{-0.02}$	$1.78/877$

Note.

— The blackbody component is shown for Swift/XRT and RXTE/PCA data separately. The parameters for the Compton component are: seed photon temperature (T_s), electron temperature (T_e), optical depth (τ), and normalization (N_{comp}). The geometry parameter is frozen at 0.8.

$\dagger$In units of erg s^{-1} kpc^{-2}

$\ddagger$The blackbody temperature kT_{bb} and normalization parameter N_{bb}, respectively, are tied between the Swift and RXTE data.

6. VERITAS Observations of Cygnus X-3

6.1 Observations & Data Reduction

The greater part of my research has been focused on the microquasar Cygnus X-3. This source has had a central role in the history of high-energy astrophysics, and still sparkles the interest of many astrophysicists. For many years, VERITAS has been involved in a monitoring program of Cygnus X-3. My work on Cygnus X-3 has been first of all dedicated to the TeV gamma-ray observations, and in a second moment to the correlations of the very-high-energy and high-energy emission with the other wavelengths. The details of the study can be viewed in the paper Archambault et al.(2013) [105]. I will describe the research in the following paragraphs.

6.1.1 Introduction

Cygnus X-3 was among the first X-ray sources to be discovered in the early days of X-ray astronomy. It lies in the Galactic plane, at a distance between 7 kpc and 10 kpc [106, 107]. It is a high-mass X-ray binary, with the companion star appearing to show the spectral characteristics of a Wolf-Rayet star [108]. The nature of the compact object is still being debated. Cygnus X-3 is known to produce intense radio flares, making it at times one of the brightest transient Galactic radio sources. The radio flares can last from a few days to several weeks. Relativistic jets have been seen during major flares ($S_\nu > 10$ Jy at 15 GHz) [109, 110], with an inclination to the line of sight of $\lesssim 14°$. This makes Cygnus X-3 analogous to the extragalactic blazars, which constitute a major population of known TeV gamma-ray emitters. With an orbital period of only 4.8 hours, the compact object is thought to be enshrouded in the wind of the Wolf-Rayet star.

Cygnus X-3 has long been a prominent target for gamma-ray observations. Initially, there was contradictory evidence for gamma-ray emission at GeV energies: SAS-2 found a periodic signal [8], while COS-B could not confirm it [9]. Then, numerous claims of detection of Cygnus X-3 were made in the early days of ground-based gamma-ray experiments, spanning the TeV to PeV energy range (see discussions by [33] and [111]). The claims were subsequently disputed by a critical analysis of the observations [112]. In subsequent years, Cygnus X-3 was observed with more sensitive ground-based instruments, including Whipple [113], CASA-MIA [114], HEGRA [115], and MAGIC [116], but was not detected. At GeV energies, EGRET/CGRO found a gamma-ray source (2EG J2033+4112) that was consistent with the position of Cygnus X-3 (although the position error circle was quite large), but with no evidence for orbital modulation [117]. The source has now been detected at GeV energies, with high confidence, independently with AGILE [118] and Fermi LAT [60]. Moreover, the orbital modulation of the gamma-ray emission has also been seen [60].

In X-ray binaries, gamma rays may be produced by Compton upscattering of photons, either from the companion star or the accretion disk or both, by relativistic electrons accelerated in the jets of a stellar-mass black hole or in the shocked wind of a pulsar. Detailed models have been constructed for gamma-ray production and attenuation in the jets. In the case of Cygnus X-3, the close proximity ($R_d \approx 3 \times 10^{11}$ cm), high temperature ($T_* \sim 10^5$ K), and high luminosity ($L_* \sim 10^{39}$ erg s^{-1}) of the Wolf-Rayet star may result in the efficient Compton upscattering of stellar photons to produce gamma rays, as well as in the attenuation of the gamma rays via $\gamma\gamma$ pair production [119]. Whether Cygnus X-3 appears as a TeV gamma-ray emitter would depend on the competition between the production and attenuation processes. Theoretically, certain circumstances would favor TeV emission. These typically involve emitting regions at large perpendicular distances ($H \gtrsim 10 R_d$) from the orbital plane and orbital phases around the inferior conjunction [119]. At lower (GeV) energies, the attenuation optical depth is much reduced, so the observed orbital modulation may be mainly associated with the production process [119, 120]. Alternatively, gamma

rays may also be produced by the decay products (π^0) of pp collisions during interactions between the relativistic protons in the jets and the cold protons of the dense anisotropic stellar wind of the Wolf-Rayet star [121].

Cygnus X-3 is a persistent radio source. Its radio flux may vary by four orders of magnitude. Based on the long-term monitoring of the source with the Green Bank Interferometer (GBI), four radio states were identified [122]: quiescent state (60-140 mJy), minor flaring state ($\lesssim 1$ Jy), quenched state ($\lesssim 30$ mJy), and intermediate/major flaring state (>1 Jy). The major flaring state seems to follow the quenched state. The radio emission was subsequently found to be correlated with the hard X-ray emission [123]. The correlation is complex and varies with the state that the source is in: it is negative (anti-correlation) in the quiescent state but turns positive in the major flaring and quenched states. No apparent correlation has been observed in the minor flaring state. The radio emission is also correlated with the soft X-ray emission in certain states [124]. This is expected because it is known that the soft and hard X-ray fluxes of Cygnus X-3 are generally (but not always) anti-correlated [124, 125]. Based on the correlated radio/X-ray properties of the source, Szostek et al. (2008) refined and expanded the definitions of the states [126]. The new radio/X-ray states are now referred to as the *quiescent, minor-flaring, suppressed, quenched, major-flaring* and *post-flaring* states.

The AGILE and Fermi-LAT observations have shown that the gamma-ray emission from Cygnus X-3 is not steady but episodic. A careful examination of the gamma-ray activities of the source has revealed that gamma-ray production appears to be associated with transitions into or out of the radio *quenched* state [127]. During a transition, the X-ray spectrum of the source becomes dominated by a soft X-ray component (with only a weak power-law component) as its radio flux goes down. For this reason, these time periods are now also referred to as the hypersoft state [127]. As such, the line between the hypersoft state and *quenched* state is not always very clear in practice. Observationally, the hypersoft state is associated with major radio flares and, sometimes, the formation of jets [127]. The latter might be the site of

gamma-ray production. This signifies the importance of the hypersoft state to our understanding of Cygnus X-3 as a gamma-ray emitter. Unfortunately, the hypersoft state is very short in duration (lasting for $\lesssim$ 4-5 days), compared with other states, so it is often challenging to catch it with sensitive instruments of small field of view.

In this work, we carried out a systematic search for gamma rays from Cygnus X-3 at TeV energies with the Very Energetic Radiation Imaging Telescope Array System (VERITAS). The availability of the contemporaneous radio/X-ray observations of the source made it possible to extend the search to individual radio/X-ray states, particularly to the hypersoft state.

6.1.2   VERITAS

For this work, we used data from observations conducted between 11 June, 2007 and 28 November, 2011. The observations were conducted under varying weather and other conditions. The design of VERITAS also allows observations to be conducted under partial moonlight. In many of those cases, the triggering threshold needs to be raised, which leads to a higher energy threshold. The triggering threshold is raised by increasing the voltages in the camera photomultiplier tubes, which mitigates the night sky background fluctuations caused by the moonlight. We carefully examined the data and included all of the observations which we believe can lead to reliable results. The total exposure time amounts to about 44 hours. More detailed information on the observations is shown in Table 6.1.

Table 6.1.   Summary of VERITAS Observations for Cygnus X-3

MJD	Calendar Date	X-ray State	Observing Time (min)	Elevation Range	N_{tel}
54262	2007/06/11	Minor flaring	20	$65^o - 69^o$	3
54263	2007/06/12	Minor flaring	40	$70^o - 77^o$	3
54264	2007/06/13	Minor flaring	119.5	$62^o - 80^o$	3
54265	2007/06/14	Minor flaring	80	$72^o - 80^o$	3
54266	2007/06/15	Minor flaring	40	$72^o - 78^o$	3
54626	2008/06/09	Quenched	40	$76^o - 80^o$	4
54627	2008/06/10	Quenched	40	$76^o - 80^o$	4
54628	2008/06/11	Quenched	20	$80^o - 81^o$	4
54731	2008/09/22	Suppressed	20	$76^o - 78^o$	4
54774	2008/11/04	Quenched	20	$59^o - 63^o$	4
54786	2008/11/16	Major flaring	60	$59^o - 72^o$	4
54789	2008/11/19	Quenched	60	$64^o - 68^o$	4
54794	2008/11/24	Quenched	40	$54^o - 60^o$	4
54800	2008/11/30	Quenched	20	$54^o - 58^o$	3
54804	2008/12/04	Hypersoft[a]	20	$53^o - 56^o$	4
55126	2009/10/22	Quiescent	20	$74^o - 76^o$	4
55127	2009/10/23	Quiescent	36	$67^o - 74^o$	4
55128	2009/10/24	Quiescent	77	$59^o - 79^o$	4
55129	2009/10/25	Quiescent	40	$65^o - 74^o$	4
55155	2009/11/20	Quiescent	20	$59^o - 62^o$	3
55156	2009/11/21	Quiescent	40	$56^o - 64^o$	4
55157	2009/11/22	Quiescent	20	$56^o - 59^o$	4
55158	2009/11/23	Quiescent	16	$64^o - 67^o$	4
55382	2010/07/05	Minor flaring	20	$72^o - 76^o$	4
55384	2010/07/07	Minor flaring	4	$80^o - 80^o$	4
55481	2010/10/12	Quiescent	40	$75^o - 80^o$	4
55482	2010/10/13	Quiescent	40	$69^o - 77^o$	4
55648	2011/03/28	Major flaring	20	$42^o - 46^o$	4
55649	2011/03/29	Major flaring	20	$42^o - 46^o$	3
55650	2011/03/30	Major flaring	20	$43^o - 48^o$	4
55651	2011/03/31	Major flaring	28	$45^o - 51^o$	3
55652	2011/04/01	Major flaring	20	$42^o - 46^o$	3
55653	2011/04/02	Major flaring	20	$42^o - 46^o$	4
55654	2011/04/03	Major flaring	15	$48^o - 50^o$	4
55655	2011/04/04	Major flaring	20	$48^o - 50^o$	4

Table 6.1 (cont'd)

MJD	Calendar Date	X-ray State	Observing Time (min)	Elevation Range	N_{tel}
55656	2011/04/05	Major flaring	20	$48^o - 52^o$	4
55658	2011/04/07	Minor flaring	8	$52^o - 53^o$	3
55659	2011/04/08	Minor flaring	23	$50^o - 53^o$	4
55662	2011/04/11	Minor flaring	6	$55^o - 56^o$	3
55707	2011/05/26	Minor flaring	20	$72^o - 74^o$	4
55708	2011/05/27	Minor flaring	20	$60^o - 64^o$	4
55709	2011/05/28	Minor flaring	96	$65^o - 80^o$	4
55710	2011/05/29	Minor flaring	52	$70^o - 77^o$	3/4[b]
55713	2011/06/01	Minor flaring	20	$59^o - 62^o$	4
55715	2011/06/03	Minor flaring	40	$77^o - 80^o$	4
55716	2011/06/04	Minor flaring	20	$70^o - 74^o$	4
55717	2011/06/05	Minor flaring	20	$79^o - 81^o$	4
55720	2011/06/08	Minor flaring	20	$76^o - 78^o$	4
55721	2011/06/09	Minor flaring	10	$74^o - 75^o$	4
55733	2011/06/21	Minor flaring	14	$45^o - 48^o$	4
55734	2011/06/22	Minor flaring	10	$64^o - 68^o$	4
55735	2011/06/23	Minor flaring	46	$59^o - 69^o$	4
55736	2011/06/24	Minor flaring	84	$74^o - 80^o$	4
55737	2011/06/25	Minor flaring	40	$69^o - 73^o$	4
55738	2011/06/26	Quiescent	59.5	$74^o - 80^o$	4
55739	2011/06/27	Quiescent	95	$71^o - 80^o$	4
55740	2011/06/28	Quiescent	30	$76^o - 80^o$	3
55743	2011/07/01	Quiescent	20	$76^o - 80^o$	4
55744	2011/07/02	Quiescent	20	$76^o - 78^o$	4
55830	2011/09/26	Quiescent	80	$78^o - 80^o$	3/4[b]
55833	2011/09/29	Quiescent	48	$74^o - 80^o$	4
55834	2011/09/30	Quiescent	52	$64^o - 79^o$	3/4[b]
55835	2011/10/01	Quiescent	43.5	$66^o - 75^o$	4
55850	2011/10/16	Quiescent	28	$74^o - 80^o$	4
55851	2011/10/17	Quiescent	80	$72^o - 80^o$	4
55852	2011/10/18	Quiescent	71	$68^o - 80^o$	4
55853	2011/10/19	Quiescent	51	$70^o - 79^o$	4
55854	2011/10/20	Quiescent	111	$70^o - 79^o$	4
55855	2011/10/21	Quiescent	20	$58^o - 60^o$	4
55858	2011/10/24	Quiescent	20	$59^o - 61^o$	4

Table 6.1 (cont'd)

MJD	Calendar Date	X-ray State	Observing Time (min)	Elevation Range	N_{tel}
55860	2011/10/26	Quiescent	20	$58^{\circ} - 61^{\circ}$	4
55861	2011/10/27	Quiescent	17	$70^{\circ} - 74^{\circ}$	4
55862	2011/10/28	Quiescent	72	$59^{\circ} - 80^{\circ}$	4
55863	2011/10/29	Quiescent	35	$74^{\circ} - 80^{\circ}$	4
55864	2011/10/30	Quiescent	15	$76^{\circ} - 80^{\circ}$	4
55865	2011/10/31	Quiescent	40	$66^{\circ} - 76^{\circ}$	4
55888	2011/11/23	Quiescent	36	$60^{\circ} - 68^{\circ}$	4
55891	2011/11/26	Quiescent	20	$61^{\circ} - 64^{\circ}$	4
55892	2011/11/27	Quiescent	40	$56^{\circ} - 64^{\circ}$	4
55893	2011/11/28	Quiescent	20	$52^{\circ} - 56^{\circ}$	4

[a]The hypersoft state consists of the data run contained within the quenched state. See text.

[b]One telescope was taken out of the operation during the run.

Note. — The column N_{tel} shows the number of working telescopes.

The reduction of VERITAS data consists of multiple steps, including rejection of substandard data, flat fielding, pedestal subtraction, pulse integration, image cleaning, parameterization of events, stereo reconstruction of shower direction and impact parameter, and gamma-ray/cosmic-ray separation. More details of the VERITAS analysis can be viewed in the Section 2.3. Briefly, the data from each participating telescope are first filtered for bad weather or issues with data acquisition, and are then charge integrated, pedestal subtracted and gain corrected. Each resulting image is cleaned and characterized to derive the moments of the light distributions [20]. The images of the same air shower from all participating telescopes are used to reconstruct the direction and impact parameter of the shower (see e.g. [85]). This step requires characterizable images from three or more telescopes. In addition, to separate the gamma-ray events from the cosmic-ray events, we applied selection criteria (based on the energy and geometry of the events) to the events that survived the previous

steps. The post-selection energy threshold is about 220 GeV at a 10° zenith angle and 450 GeV at a 40° zenith angle, which correspond approximately to the highest and lowest zenith angle of our data set, respectively. More details about VERITAS, the calibration procedure and the analysis technique can be found in [128].

The VERITAS observation set was the product of different observation modes: it was composed of wobble-mode data on Cygnus X-3, wobble-mode data taken on the TeV gamma-ray source TeV J2032+4130 [88], which is $\sim 30'$ from Cygnus X-3, and data from tracking mode on the mid-point position between Cygnus X-3 and TeV J2032+4130. In wobble mode, the telescopes are pointed such that the source is always located at a fixed offset (0.5°), alternately to the north, south, east and west of the camera center, for an unbiased estimation of the FoV background of the source region. In tracking mode, the telescopes were pointed alternatively to the east and west of the mid-point position between Cygnus X-3 and TeV J2032+4130. Due to the mixture of different observing modes, the data analysis used the ring background model [34]. Briefly, the background estimate is derived for a trial source position from an annulus around the source region, which is dependent on the selection criteria. Due to the different offsets of the ring points with respect to the camera center as compared to the source position, a relative event rate, or *acceptance*, correction needs to be applied to normalize the background rate. Any gamma-ray source in the FoV needs to be excluded from the background estimation as well. In our case, we excluded the pixels pointing at bright stars (with B magnitude less than 6) from the background regions. The nearby known TeV gamma-ray source, TeV J2032+4130, was removed from subsequent analyses, to avoid incorrect estimation of the source and background rates of Cygnus X-3 in the analysis.

The data analysis on Cygnus X-3 was performed with selection-criteria parameters based on the energy and geometry configuration of the gamma-ray initiated air showers, and modeled on the Crab Nebula. The selection criteria are optimized for a putative source with either a soft (6.6% Crab at 200 GeV, spectral index: -4), medium (2% Crab at 400 GeV, spectral index: -2.4) or hard (2% Crab at 1 TeV, spec-

tral index: -2.0) spectral index. The selection criteria parameters tend to be looser for softer sources than for harder ones, to allow less event selection restrictions in the analysis. The acceptance correction was consequently generated over the whole data set for soft, medium and hard selection criteria and then applied to partial data sets (e.g., for individual states). For data taken with the initial VERITAS telescope array configuration (prior to August 2009) where telescope 1 (T1) and telescope 4 (T4) were in proximity to one another, all T1 and T4 simultaneous events were removed from analysis if only one other telescope (T2 or T3) was triggered.

6.1.3 Fermi/LAT

The LAT data were processed with the Fermi Science Tools (v9r23p1), following the recommendations on event selection from the Fermi Science Support Center[1]. Briefly, the events that have the highest probability of being gamma rays were selected by means of the Pass 7 V6 (P7_V6) source class event selection cut with the gtselect tool. In order to minimize contamination from Earth albedo photons, the time periods when Cygnus X-3 was observed at zenith angles greater than $100°$ were eliminated from further analysis. The energy range was also limited to the 0.1-100 GeV band.

For background modeling, we included all of the sources in the Fermi Large Area Telescope Second Source (2FGL) Catalog [70] that are in the vicinity of Cygnus X-3. To account for possible intrinsic variability of the sources, we allowed the spectral parameters of the sources in a $5°$-radius region of interest (RoI) to vary in an unbinned maximum likelihood analysis. On the other hand, we froze the spectral parameters of the sources that are outside of the RoI but within a $22°$-radius source region at the 2FGL values. To minimize contamination for a bright nearby pulsar, PSR J2032+4127 (about $30''$ away from Cygnus X-3), following [129], we excluded the times of its peak-pulse emission, based on the pulsar ephemeris[2] [130]. As for

---

[1] `http://fermi.gsfc.nasa.gov/ssc/data/analysis/scitools/`

[2] The pulsar ephemeris for PSR J2032+4127 is available at: `http://www.slac.stanford.edu/~abdo/LATPulsarTimingModels/Latest/J2032+4127/J2032+4127_latest.par`

the Galactic and extragalactic diffuse gamma-ray backgrounds, we adopted the most recent models (*gal_2yearp7v6_v0.fits* and *iso_p7v6source.txt*). We also modeled the emission from the Cygnus Loop region with a template that is provided in the LAT Catalog Data Products. The instrument response function (IRF) used in this work is IRF P7SOURCE_V6.

We derived, from background modeling, the best-fit spectral parameters of the sources in the RoI. We then fixed the parameters for all other sources, as well as the spectral index of Cygnus X-3, and performed another unbinned maximum likelihood analysis, to produce a light curve of Cygnus X-3 over the time period of interest. The statistical significance of each measurement is quantified by a maximum likelihood test statistic (TS; [92]), which corresponds roughly to $\sqrt{TS}\,\sigma$ in Gaussian statistics.

6.1.4   RXTE/ASM, Swift/BAT & MAXI

Contemporaneous X-ray coverages of Cygnus X-3 were provided by the All-sky Monitor (ASM) aboard the *Rossi X-ray Timing Explorer* satellite [40], the Burst Alert Monitor (BAT) aboard the *Swift* satellite [41], and the Monitor of All-sky X-ray Image (MAXI) aboard the International Space Station [42]. The ASM and MAXI cover soft X-ray bands of 1.5–12 keV and 2–20 keV, respectively, while the BAT covers a hard X-ray band of 15–50 keV. For this work, we chose to use the ASM and MAXI data in a narrower (soft) band, to achieve a more accurate characterization of the states [126]. We weighted the measured count rates or fluxes of Cygnus X-3 (by $1/\sigma^2$), which are made publicly available by the instrument teams, and, if necessary, rebinned them to produce daily-averaged light curves.

6.1.5   AMI-LA

At radio wavelengths, Cygnus X-3 is monitored regularly with the *Arcminute Microkelvin Imager-Large Array* (AMI-LA)[3] at the Mullard Radio Astronomy Ob-

---

[3]http://www.mrao.cam.ac.uk/~guy/cx3/

servatory in the UK. The AMI-LA consists of eight 12.8-meter Cassegrain antennas in a 2-dimensional array, with a baseline of ~ 120 meters [45]. It operates in six frequency bands covering the range of 13.9–18.2 GHz. Here, we used the data taken from 26 May, 2008 to 31 December, 2011. Note that no data were taken between 19 June, 2006 and 26 May, 2008, due to the major upgrade of the Ryle Radio Telescope to the AMI-LA. The weighted, daily-averaged light curve was used for this work.

6.2 Results

6.2.1 Blind Searches for TeV Gamma Rays

Using the full VERITAS data set, we found no significant ($> 5\sigma$) excess of TeV gamma rays from Cygnus X-3 with the soft, medium and hard data cuts. The significance was calculated with the modified Eq. (17) of [35], which is generalized for data sets with different source and background regions [131]. The results are summarized in Table 6.2.

To derive a flux upper limit for each observing run, we calculated the total counts in the source region N_{on}, total counts in the background region N_{off}, and a scale factor α, which is defined as the ratio of the areas of the (geometrical or parameter) regions from which source and background counts are derived. The scale factor may be different for different cuts. It may also vary from run to run, because, for instance, a bright star or known gamma source may need to be excluded from the background region in certain wobble configurations. For the analyses of multiple data runs, individual α's were weighted by corresponding background counts and averaged to produce an effective α_{eff} for the runs. To account for varying zenith angle conditions, an average effective area A_{eff} was constructed from individual effective areas for the runs. The flux upper limit was then derived from total N_{on}, total N_{off}, α_{eff}, A_{eff}, and total effective exposure time, with the method of [132].

Table 2 shows the 95% confidence level (C.L.) integral flux upper limits derived with the full VERITAS data set. We chose as the lower limit for flux integration

Table 6.2.   Results from Gamma-Ray Searches for Cygnus X-3

Spectral State	Exposure Time (hours)	Elevation Range	On Events N_{on}	Off Events N_{off}	α_{eff}	Excess Events N_{ex}	Significance (σ)	Energy Threshold (GeV)	Flux Upper Limit $(10^{-12}\mathrm{cm}^{-2}\mathrm{s}^{-1})$
				Soft Cuts					
All	44.70	$42^{\circ} - 81^{\circ}$	17509	125799	0.136	400.3	0.6	182	5.0
Quiescent	23.04	$52^{\circ} - 80^{\circ}$	9046	65596	0.136	124.9	0.3	182	4.6
Minor flaring	13.68	$45^{\circ} - 81^{\circ}$	4032	28865	0.138	48.6	0.6	200	6.1
Suppressed	0.30	$76^{\circ} - 78^{\circ}$	162	1069	0.156	-4.8	-0.4	200	64.6
Quenched	4.24	$54^{\circ} - 81^{\circ}$	2410	16923	0.142	6.9	0.1	200	20.5
Hypersoft[a]	0.30	$53^{\circ} - 63^{\circ}$	180	1360	0.142	-13.1	-0.9	316	29.0
Major flaring	3.44	$42^{\circ} - 72^{\circ}$	1859	13344	0.138	17.5	0.4	316	10.9
				Medium Cuts					
All	44.70	$42^{\circ} - 81^{\circ}$	1200	26176	0.046	-4.1	-0.1	263	0.7
Quiescent	23.04	$52^{\circ} - 80^{\circ}$	654	15268	0.046	-48.3	-1.7	263	0.5
Minor flaring	13.68	$45^{\circ} - 81^{\circ}$	343	6813	0.046	29.6	1.5	288	2.1
Suppressed	0.30	$76^{\circ} - 78^{\circ}$	11	94	0.047	6.6	2.5	288	41.8
Quenched	4.24	$54^{\circ} - 81^{\circ}$	96	2097	0.047	-2.6	-0.1	347	2.5
Hypersoft[a]	0.30	$53^{\circ} - 63^{\circ}$	8	205	0.045	-1.2	-0.4	457	9.0
Major flaring	3.44	$42^{\circ} - 72^{\circ}$	96	1904	0.047	6.5	0.7	550	2.2
				Hard Cuts					
All	44.70	$42^{\circ} - 81^{\circ}$	145	3305	0.045	-3.7	-0.2	603	0.2
Quiescent	23.04	$52^{\circ} - 80^{\circ}$	68	1936	0.045	-19.1	-2.0	603	0.1
Minor flaring	13.68	$45^{\circ} - 81^{\circ}$	46	831	0.046	7.8	1.2	603	0.6
Suppressed	0.30	$76^{\circ} - 78^{\circ}$	1	14	0.045	0.4	0.4	603	10.2
Quenched	4.24	$54^{\circ} - 81^{\circ}$	13	281	0.046	0.1	0.0	871	0.9
Hypersoft[a]	0.30	$53^{\circ} - 63^{\circ}$	3	25	0.042	2.0	1.5	871	9.2
Major flaring	3.44	$42^{\circ} - 72^{\circ}$	17	244	0.047	5.5	1.5	955	1.2

[a]The hypersoft state consists of the data run from 2008/12/04 (MJD 54804) and is a data run subset contained within the quenched state.

Note. — Flux upper limits are given at the 95% C.L, and for each row are calculated from the energy threshold. The column α_{eff} shows the effective scale factor for the background calculation (see § 9.4).
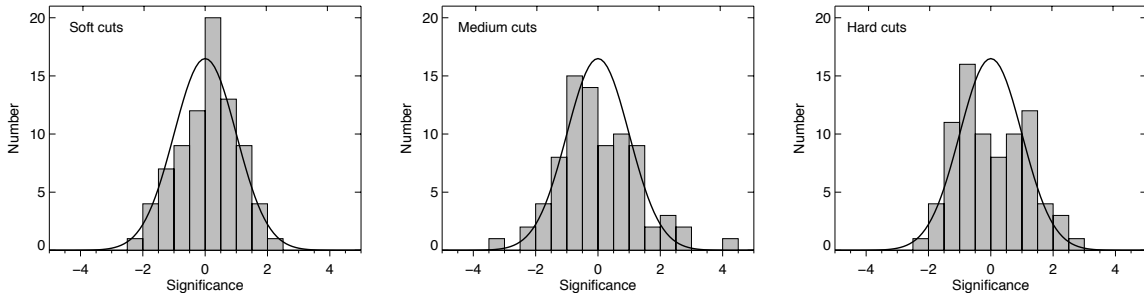
Figure 6.1.: Gaussian significance (in units of σ) distributions for VERITAS nightly searches. The results from different data cuts are shown separately. The Gaussian functions with mean zero and σ one are shown in solid lines.

the energy threshold, which is defined as the energy at which the differential rate of gamma-ray detection as a function of energy reaches its maximum. Different data cuts lead to different energy thresholds (also shown in the table). We should point out that we did not include systematic uncertainties in this or subsequent analyses.

Search for Episodic Emission

We also conducted a blind search for episodic TeV gamma-ray emission from Cygnus X-3. In this case, the VERITAS data runs were grouped on a night-by-night basis. As before, we selected events with the soft, medium and hard cuts, respectively, and followed the same procedure to reduce and analyze the data. Figure 6.1 shows the distribution of the significance of excess for each set of cuts separately. The distributions are consistent with no significant TeV gamma-ray signal from Cygnus X-3 (with the 99% C.L. integral flux upper limits shown in the top panel of Figure 6.4 for individual nights).

Search for Orbital Modulation

Considering that gamma-ray production could be concentrated in certain parts of the binary orbit, we folded the data from all observing runs into 10 phase bins,

using the ephemeris of [133]. When a run spans multiple phase bins, we took care in dividing it so that the events fall in the correct bins. Again, we followed the same procedure to reduce and analyze the runs (or sub-runs) for each phase bin. We found no significant excess over the entire orbit. The 95% C.L. integral flux upper limits (derived with the medium cuts) are shown in Figure 6.2.
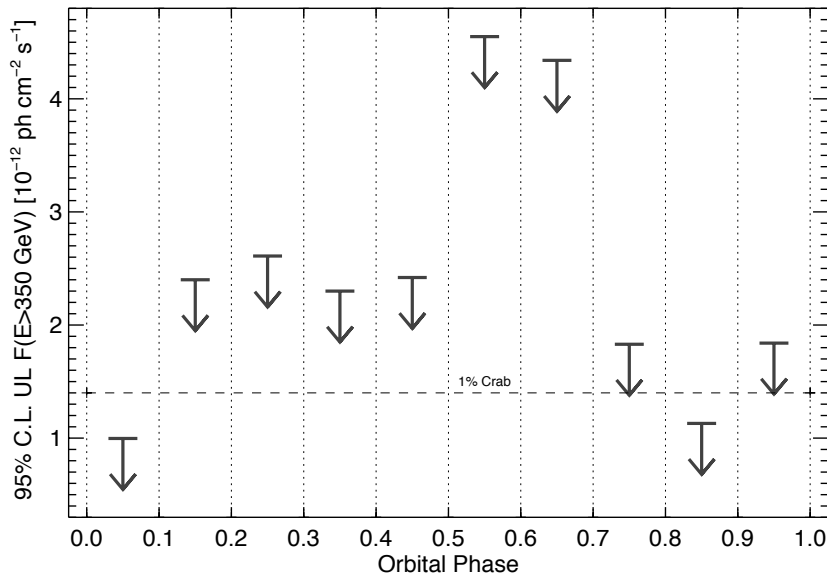
Figure 6.2.: VERITAS phase-folded 95% C.L. integral ($E > 350$ GeV) flux upper limits of Cygnus X-3. For reference, the level of 1% Crab is indicated (in dashed line).

Spectral Constraints

To place constraints on the gamma-ray spectrum of Cygnus X-3 at TeV energies, we also analyzed the data for selected energy ranges. The 95% C.L. integral flux upper limits are given in Table 6.3, and the corresponding differential flux upper limits shown in Figure 6.3. We adopted logarithmic energy binning ($\Delta E/E \sim 30\%$) for this analysis. The bins are coarser than the energy resolution of VERITAS but are sufficiently small to minimize any spectral dependence of the results. Such depen-

Table 6.3.   Flux Upper Limits for Selected Energy Ranges for Cygnus X-3

Energy Range (TeV)	On Events N_{on}	Off Events N_{off}	α_{eff}	Excess Events N_{ex}	Significance (σ)	Flux Upper Limit $(10^{-12}\text{cm}^{-2}\text{s}^{-1})$
0.263-0.342	230	4726	0.046	12.6	0.8	0.5
0.342-0.445	151	3801	0.046	-23.8	-1.9	0.1
0.445-0.578	126	2905	0.046	-7.6	-0.7	0.2
0.578-0.751	102	2229	0.046	-0.5	-0.1	0.2
0.751-0.977	65	1663	0.046	-11.5	-1.3	0.1
0.977-1.269	58	1253	0.046	0.4	0.0	0.2
1.269-1.650	36	1033	0.046	-11.5	-1.7	0.1
1.650-2.145	39	795	0.046	2.4	0.4	0.2
2.145-2.789	25	627	0.046	-3.8	-0.7	0.1
2.789-3.626	20	447	0.046	-0.6	-0.1	0.1
3.626-4.713	14	354	0.046	-2.3	-0.6	0.1

Note. — As for Table 6.2, but for selected energy ranges.

dence may arise from the fact that the effective area is constructed, via Monte-Carlo simulations, with an assumed input spectrum (which, in this case, has a photon index of -2.4) and certain data cuts (which, in this case, are the medium cuts). Above about 5 TeV, the number of events that pass the cuts is so small that the results (not shown) become very uncertain. For comparison, we also plotted the published MAGIC differential flux upper limits [116] in the figure, as well as the extrapolation of the best-fit power-law spectra measured with AGILE and Fermi/LAT.

6.2.2   Targeted Searches for TeV Gamma Rays in Radio/X-Ray States

As mentioned in § 6.1.1, there appears to be evidence for gamma-ray production in Cygnus X-3 only in certain radio/X-ray states. For a more effective search, it is, therefore, important to characterize the states that the source is in. Fortunately, there were extensive X-ray and radio coverages of Cygnus X-3 that were contemporaneous
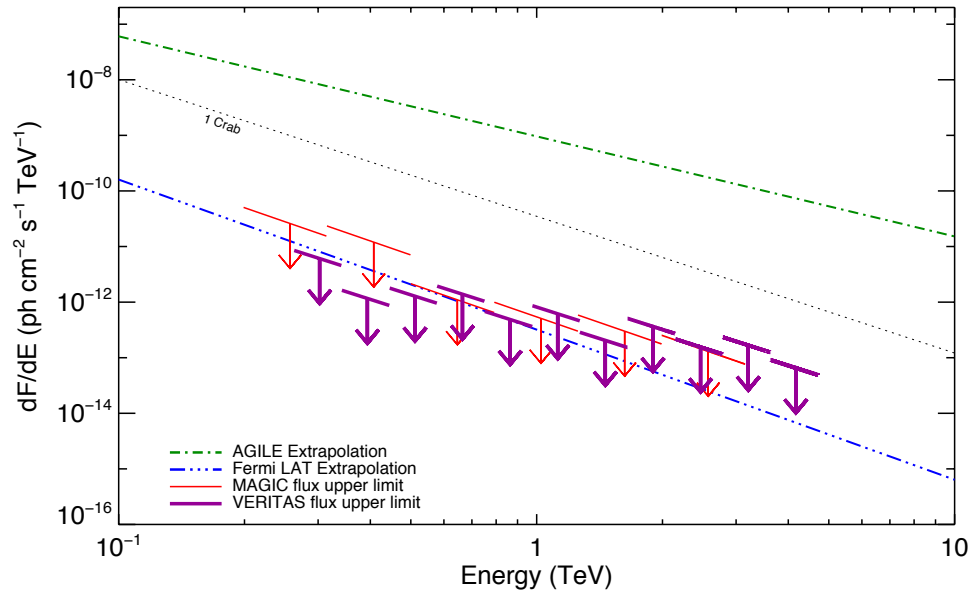
Figure 6.3.: VERITAS 95% C.L. differential flux upper limits of Cygnus X-3. For comparison, the published MAGIC upper limits are shown in (red) thin solid lines. See Figure 1 and Table 2 of [116] for further details concerning the MAGIC results. A nominal spectrum of the Crab Nebula is shown in the (black) dotted line, for reference. The (blue) dot-dot-dot-dashed line and (green) dot-dashed line show the extrapolations of the power-law spectra measured with the Fermi/LAT and AGILE at GeV energies, respectively.

with the VERITAS observations. We used the radio and (soft and hard) X-ray light curves of the source, as shown in Figure 6.4, to distinguish the states, as defined in [126]. We chose to divide the post-flaring state appropriately and merge it into the minor flaring and suppressed states.

It is worth noting a few key features in the multi-wavelength light curves shown in Figure 6.4. First, the anti-correlation between the soft and hard X-ray bands is apparent, comparing the ASM/MAXI and Swift BAT light curves. Second, the quenched state is not easily recognizable based on the radio light curve alone. It is, in fact, more apparent in the hard X-ray light curves, as it is when hard X-ray emission is quenched as well. To be more quantitative, we define the quenched state as the

time when the Swift BAT flux goes below 0.01 cts cm^{-2} s^{-1} (or when the ASM flux goes above 3 cts s^{-1}, as the soft/hard X-ray anti-correlation suggests). Finally, the times of significant detections of Cygnus X-3 at GeV energies (see the Fermi-LAT light curve) do seem to align with the transitions into or out of the quenched state (i.e., the hypersoft state) quite well.

We grouped the VERITAS observing runs based on the radio/X-ray states, and carried out a search for TeV gamma rays from Cygnus X-3 for each of the states. The analysis was made with the soft, medium, and hard cuts. The results are shown separately in Table 6.2. No significant TeV gamma-ray signal was found in any of the searches.

6.3   Discussion

The VERITAS observations of Cygnus X-3 covered the quenched state between 30 October and 13 December, 2008 (MJD 54769 and 54813), when it was detected with AGILE (ATel #1827 [134] and Atel #1848 [135]). Unfortunately, there was only one VERITAS observation in the hypersoft/quenched state on 4 December, 2008. The source was not detected at TeV energies. The derived flux upper limits are not very constraining (see Table 6.2), due to limited VERITAS exposure.

The VERITAS observations also covered the March 2011 quenched state, as well the major flaring state (reaching a radio flux of $\sim$20 Jy) that followed. Due to the low elevation of the source and other observing constraints, VERITAS missed the peak of the radio flare (on 24 March, 2011 or MJD 55644). The source was detected during this episode with the Fermi/LAT [129]. The highest LAT flux occurred on 22 March, 2011, just before the peak of the radio flare. We failed to detect a signal from the source at TeV energies over the period from 28 March to 5 April, 2011.

Based on the entire VERITAS data set, we derived, with the medium cuts, a 95% C.L. integral flux upper limit of 0.7×10^{-12} ph cm^{-2} s^{-1} ($E > 263$ GeV), which is about a factor of three lower than the published MAGIC value ($E > 250$ GeV) [116]. Note
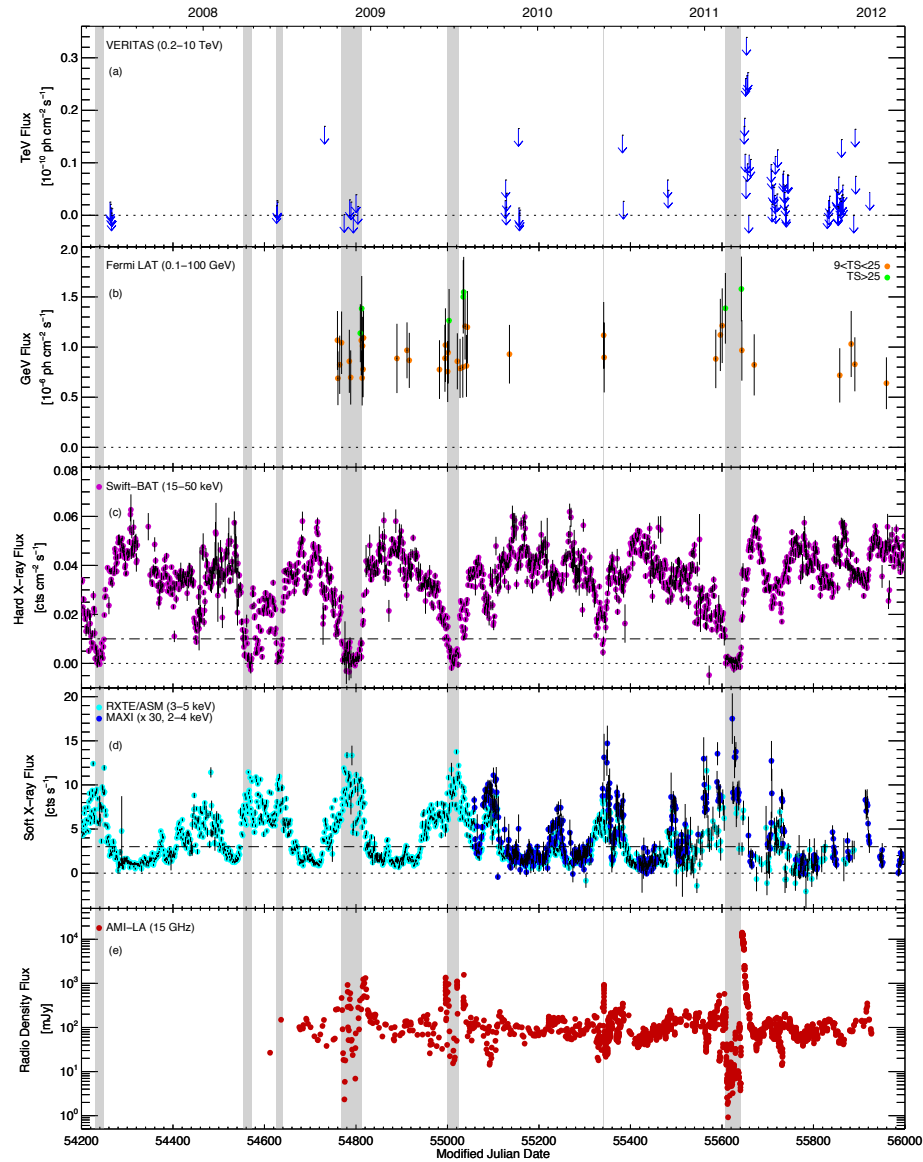
Figure 6.4.: Multiwavelength light curves of Cygnus X-3. Panels (a): TeV gamma ray. The VERITAS 99% C.L. integral ($E > 263$ GeV) flux upper limits are shown for individual nights. (b): GeV gamma ray. The data points are color-coded by the detection significance: moderate significance ($9 < TS < 25$) in orange, and high significance ($TS > 25$) in green. (c): Hard X-ray. (d): Soft X-ray. The ASM 3-5 keV measurements are shown in cyan and the MAXI 2-4 keV measurements in blue. Note that the MAXI flux values have been multiplied by 30 for clarity. (e): Radio. The AMI-LA 15 GHz measurements are shown. The shaded areas indicate the quenched state. The dot-dashed line in (c) and (d) shows roughly the threshold for transition into or out of the quenched state.

that the difference in energy thresholds between the two measurements amounts only to an effect of a few percent. We have also made a direct comparison of the VERITAS and MAGIC constraints on differential fluxes at various energies (see Figure 6.3). Our upper limits are significantly lower than the MAGIC limits at lower energies. It should, however, be noted that we did not consider systematic uncertainties in our analyses, while the MAGIC results include a 30% systematic uncertainty on flux. The VERITAS flux upper limits are compatible with the results of spectral modeling carried out by [136].

If we extrapolate the best-fit Fermi-LAT spectrum of Cygnus X-3 [60] to the VERITAS energy range, following a simple power law, we would expect an integral flux of $F(E > 263\,\text{GeV}) = 1.8\times10^{-12}$ ph cm^{-2} s^{-1}, which is comparable to our 95% C.L. flux upper limit. However, the uncertainties on the Fermi-LAT spectrum make it difficult to conclude that a spectral break or rollover would be required from GeV to TeV energies. The episodic nature of the gamma-ray emission from Cygnus X-3 has made it even more difficult to compare Fermi/LAT and VERITAS measurements. This is illustrated by the fact that the published AGILE spectrum of Cygnus X-3 [118] is higher and harder than the Fermi-LAT spectrum. If we extrapolate the best-fit power law to the AGILE spectrum into the VERITAS energy range, we would obtain an integral flux of $F(E > 263\,\text{GeV}) = 3.5\times10^{-9}$ ph cm^{-2} s^{-1} (with large uncertainties). More sophisticated spectral modeling is required to connect the Fermi/LAT and VERITAS data more physically (e.g., [136]) but it is beyond the scope of this work.

For microquasars, the kinetic power of the jets is of the order of $\sim 10^{38}$ erg s^{-1}, which is comparable to the bolometric luminosity of Cygnus X-3 (assuming a distance of 9 kpc; [124]). Our flux upper limit corresponds to an upper limit on the TeV gamma-ray luminosity $\approx 6 \times 10^{33}$ erg s^{-1}. This implies a maximum gamma-ray conversion efficiency of the order 10^{-4}-10^{-5}. In the context of leptonic models, [119] predicted a gamma-ray luminosity of $\approx 10^{32}$ erg s^{-1} for Cygnus X-3, assuming steady emission. This is discouraging for the current generation of ground-based gamma-ray

facilities, although the episodic nature of GeV gamma-ray emission from the source argues for more patience. In our case, the most interesting radio/X-ray state (i.e., the hypersoft state) has hardly been covered (see Table 6.2). A concerted, multi-wavelength effort to target this state will likely be a more effective (and resource conserving) strategy for moving forward.

7. Multi-Wavelength Observations of Cygnus X-3

In this chapter, I will focus on the multi-wavelength observations of Cygnus X-3, and expose what we think we have learned by confronting the different wavebands, spanning over 14 decades in energy. In addition to the instruments described in the previous chapter, the data from the near-infrared telescope PAIRITel and the Italian gamma-ray satellite AGILE were involved in this part of the Cygnus X-3 project, and are described in the following paragraphs. A description of the main points of my research will be presented in the following paragraphs as well. This work was presented at the conference "X-ray binaries - Celebrating the 50 years since the discovery of Sco X-1", 10-12 July, 2012 in Boston, MA [137].

7.1 Observations & Data Reduction

7.1.1 AGILE

The AGILE data were employed in my research for the multi-wavelength part of the Cygnus X-3 work. The data were reduced by the AGILE team according to the prescriptions described in [138]. The AGILE data were collected over the period from 7 December, 2009 to 8 May, 2011. The duration of the AGILE observations span from 2 to 8 days. While most of the observations are 2-σ flux upper limits, there are some episodic detections (significance $> 3\sigma$) that give support to the idea that gamma-ray emission appears to be associated with transitions into and out of the radio quenched state [127]. The following paragraphs summarize the procedure undertaken for the analysis of the AGILE data.

The data analysis was performed on the pointing-mode data set generated with the No. 3 reprocessing of the AGILE Standard Pipeline, and with the AGILE-GRID

software package version 4 which is publicly available at the ASI Data Center web site[1]. The analysis has been performed with the FM3.119 filter and the employed calibration matrix is version I0023. The events collected during the passage in the South-Atlantic Anomaly (SAA) and the Earth albedo background were consistently rejected. To reduce the particle background contamination, only events flagged as confirmed gamma-ray events were selected. These correspond to G-class events, which possess an on-axis effective area of $\sim$350 cm^2 at 100 MeV.

The multi-source likelihood analysis method [92] was applied iteratively to search for the best position, flux and spectral index of all persistent and transient emission in the Cygnus region. The likelihood ratio T_s is then just the ratio of the maximum likelihood of the two hypotheses, that is the absence and the presence of a source. For the analysis of all flaring episodes, the photon index for Cygnus X-3 was fixed to 2.0, which is consistent with the other AGILE detections reported in [118]. During the analysis, the position parameter of Cygnus X-3 is kept free and constrained with the 95% confidence contour level. The AGILE photon counts, exposure, and galactic background maps were generated with a bin size of $0.3° \times 0.3°$, for energies above 100 MeV, for the calculation of the period-averaged source flux and its evolution. The analysis was completed over a 10° radius region.

The Cygnus region contains several gamma-ray sources that are detected above 100 MeV. In particular, we studied the gamma-ray source that is consistent in position and average flux with the source PSR J2032+4127 (2FGL J2032.2+4126 in the Second Fermi LAT Catalog [91]), that is positioned only 0.4° from Cygnus X-3. For our analysis, we calculated the spectral index at $\alpha = 1.84 \pm 0.2$ and flux at $18 \pm 4 \times 10^{-8}$ph cm^{-2} s^{-1}, respectively. The galactic diffuse gamma-ray and isotropic emissions are taken into consideration in the model as well. More details on the analysis procedure can be found in [138].

---

[1]`http://agile.asdc.asi.it/`

7.1.2 PAIRITel

PAIRITel was employed in the observation of Cygnus X-3 from 4 March to 30 April, 2011 (MJD 55624.541 to 55681.454), for a total of 43 observations. The reduction of the near-infrared photometry data was accomplished with the SExtractor software package[2]. Each of the Cygnus X-3 images consists of a 600×600 array with an integration time of 5-6 minutes per image. These individual images are dithered in order to correct for bad pixels, and mosaics are created by drizzling the images. A constant aperture with a radius of 3.5 pixels with no PSF fitting was used. In PAIRITel, the result of the analysis were re-calibrated from the comparison to a small list of reference stars from the 2MASS catalog, which were within the field of view of Cygnus X-3. The list was used to calculate a magnitude average, called a zero-point magnitude reference, and used to scale the magnitude of Cygnus X-3. For the multi-wavelength plot, we use the K_s band since Cygnus X-3 is least impacted by atmospheric extinction in this band. The K_s magnitudes (2.2 μm) are converted to fluxes (in mJy) in the multi-wavelength plot for easier comparison with the other data.

7.2 Results

We show in Figure 7.1 the multi-wavelength plot of Cygnus X-3 at the time of the early 2011 radio-quenched state and major radio flare that followed the exit from the quenched state. At the exit, AGILE detected gamma-ray emission before the onset of major radio flare and before Fermi/LAT detected gamma-ray emission from Cygnus X-3. This is highlighted in Figure 7.2.

Both detections before the onset of the radio emission support the idea of a *leptonic* model of gamma-ray emission, where gamma rays could derive from the inverse Comptonization of stellar photons by the electrons in the jet, with the subsequent radio emission once the electrons become transparent to their own synchrotron emis-

---

[2]http://www.astromatic.net/software/sextractor

sion. The explanation of the AGILE detection before the Fermi/LAT one could be explained by the greater live time that AGILE possesses compared to Fermi/LAT ($\sim$40% versus $\sim$15%), which would make AGILE more suited for brief outburst events ($\sim$1 day).

From Figure 7.3, we can observe a pair of AGILE detections before the descent into the quenched state. There is one AGILE data point (MJD 55591) that does not overlap with any of the moderately significant Fermi/LAT detections before the quenched state. This could also be explained by the greater live time AGILE possesses over Fermi/LAT and its sensitivity over briefer flaring episodes. It can also be noted that the AGILE detections occur at a harder spectral index ($\Gamma \sim$1.8) than Fermi/LAT ($\Gamma \sim$2.7), for the gamma-ray active states. An explanation could be given by a fast spectral hardening that may have occurred at the peak of the gamma-ray emission, lasting $\sim$1-2 days [136].

In Figure 7.4, we can observe an overlap between the near IR (2.2 μm) emission and the AGILE emission, just before the exit from the quenched state. This overlap is curious since it has also occurred in 2010, and therefore is not an isolated event. The IR emission before the radio emission may be due to cooling electrons, but it is hard to point to the origin of the IR emission, which could come from the disk, jet or Wolf-Rayet star.

A suggestion to the IR behavior is seen in Figure 7.5. The figure depicts the average waveband-centered IR data values for the J (1.26 μm), H (1.60 μm) and K_s (2.22 μm) magnitudes, where the red curve is the average spectrum for flaring radio state, while the blue curve gives the average spectrum for the quiescent radio state. The spectral break may be due to the exhaustion of the electron energy in synchrotron process, but other IR contributions (i.e. dust) are also possible. We would expect the synchrotron contribution to increase from the infrared to the radio band, while for a Wolf-Rayet star the IR contribution would have the opposite behavior. Pinpointing the origin of the IR emission will be the focus of future work on Cygnus X-3.

In Figure 7.6, at the exit from the quenched state, we observe two peaks in the Swift/BAT emission (15-50 keV) which occur during the the decrease of the soft X-ray (1-8 keV) emission, as seen by Swift/XRT. The decrease of the soft X-ray emission is a consequence of the decrease in disk accretion following the major radio flare. These two hard X-ray peaks could be explained as the hard X-ray response to major radio flare, and specifically caused by internal shocks within the jets.

We have observed an abrupt soft X-ray peak in the period before the descent of Cygnus X-3 into the quenched state (Figure 7.7). Since the soft X-ray peak is preceded a moderately significant Fermi/LAT data point, it appears that this may be a first, unsuccessful attempt of Cygnus X-3 to enter the quenched state, and therefore we possibly see a brief occurrence of a hypersoft state before the actual entrance into the quenched state. Hypersoft states are known to be brief ($\lesssim$ 4-5 days), and may also suggest the case for higher emission above the GeV energy range [127].
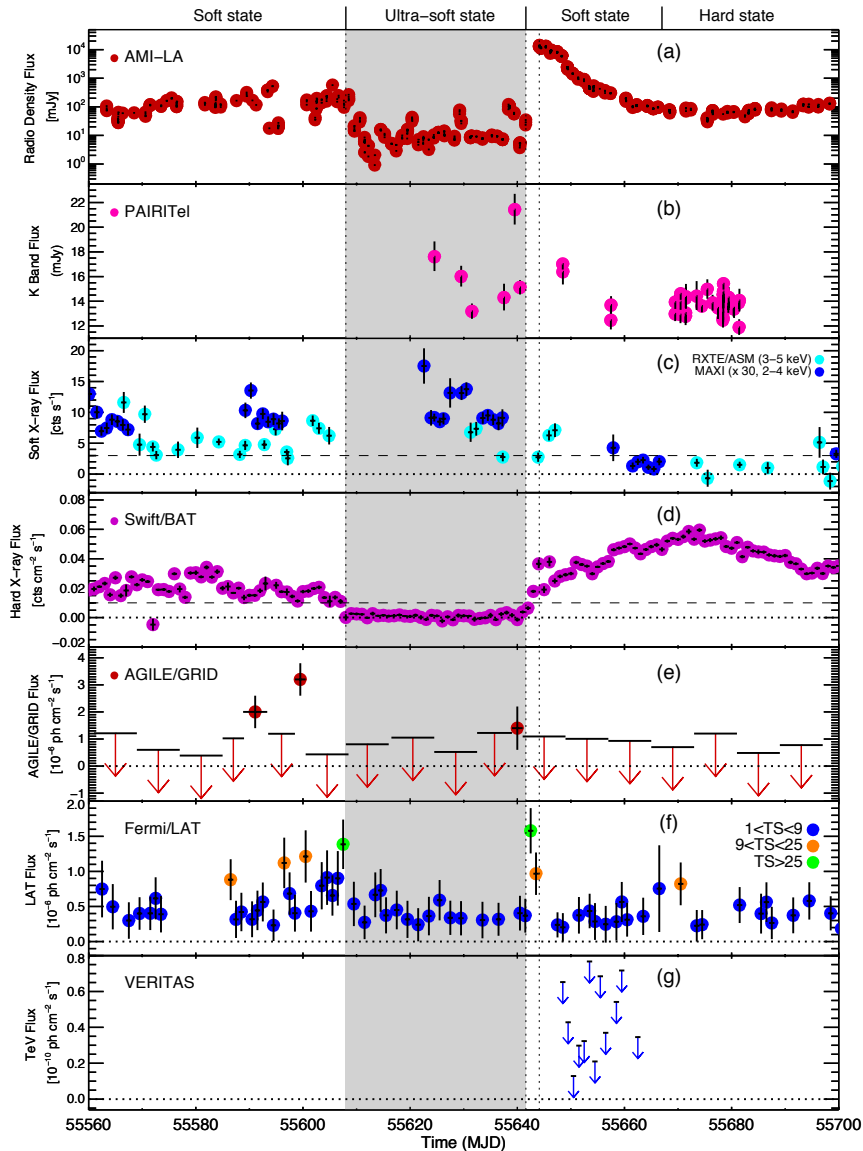
Figure 7.1.: Multi-wavelength plot of Cygnus X-3 at the time of the early 2011 radio-quenched state and major radio flare. (a): Radio. AMI-LA, 15 GHz. (b): Near IR. K_s magnitude measurements (2.2 μm) expressed in mJy. (c): Soft X-ray. The ASM 3-5 keV measurements in cyan and the MAXI 2-4 keV measurements in blue (MAXI flux values multiplied by 30 for clarity). (d): Hard X-ray. (e): AGILE (0.1-3 GeV) gamma ray. (f): LAT (0.1-300 GeV) gamma ray. Data points color-coded by detection significance: low significance ($TS < 9$) in blue, moderate significance ($9 < TS < 25$) in orange, and high significance ($TS > 25$) in green. (g): VERITAS (0.2-10 TeV) gamma ray. VERITAS 99% C.L. integral ($E > 263$ GeV) flux upper limits shown for individual nights.
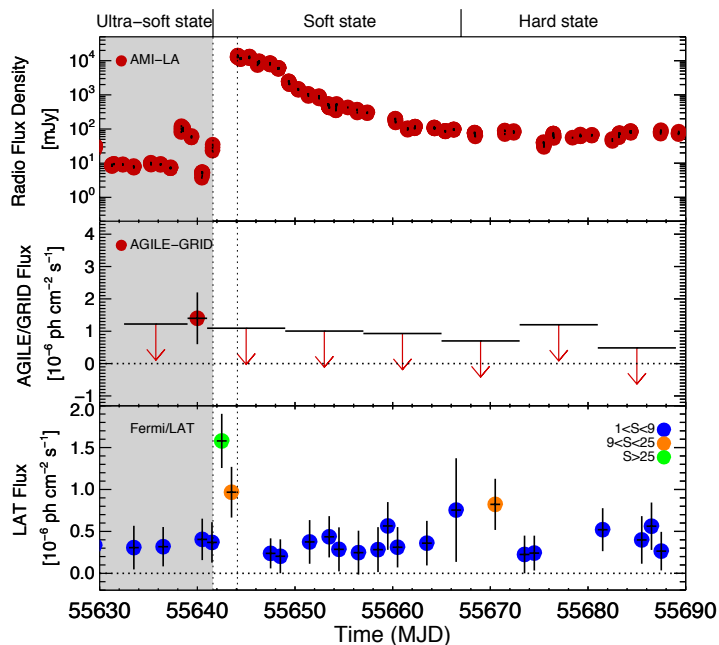
Figure 7.2.: AMI-LA (15 GHz, upper panel), AGILE (0.1-3 GeV, middle panel) and Fermi/LAT (0.1-300 GeV, lower panel), at the exit of the quenched state.
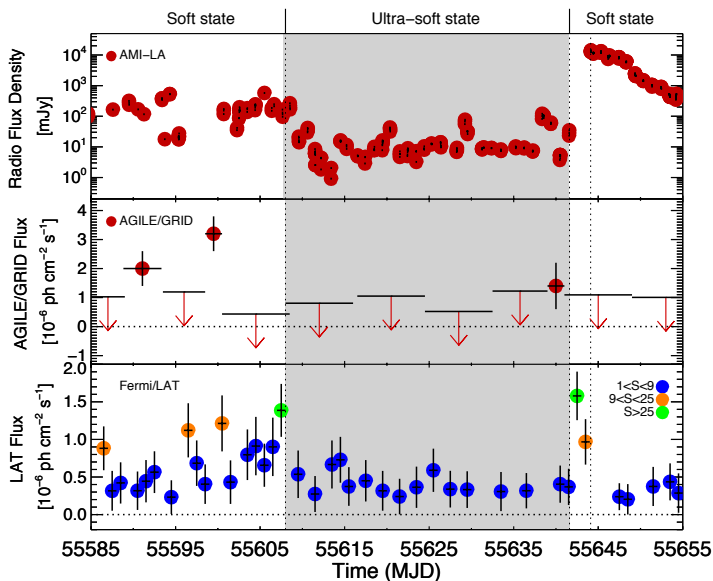
Figure 7.3.: AMI-LA (15 GHz, upper panel), AGILE (0.1-3 GeV, middle panel) and Fermi/LAT (0.1-300 GeV, lower panel). AGILE detections occur before and after the quenched state.
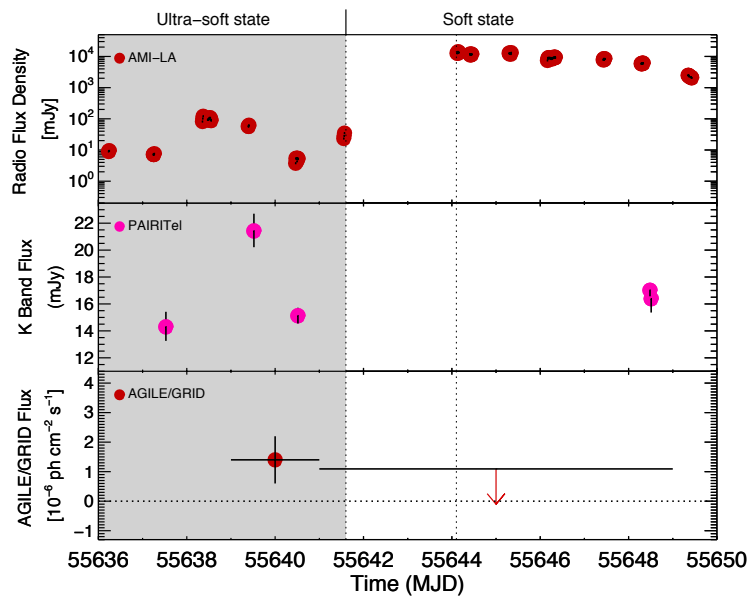
Figure 7.4.: AMI-LA (15 GHz, upper panel), PAIRITel (2.2 μm K Band, middle panel) and AGILE (0.1-3 GeV, lower panel), at the exit of the quenched state. Overlap of AGILE and PAIRITel observations just before the exit from the quenched state.

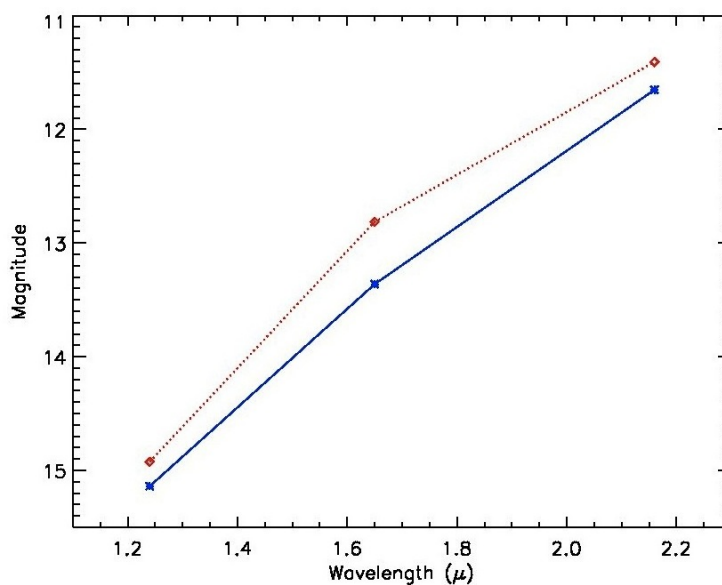Figure 7.5.: Spectral break in the infrared band. Image courtesy of Michael McCollough, from the 8th INTEGRAL Workshop (2010).
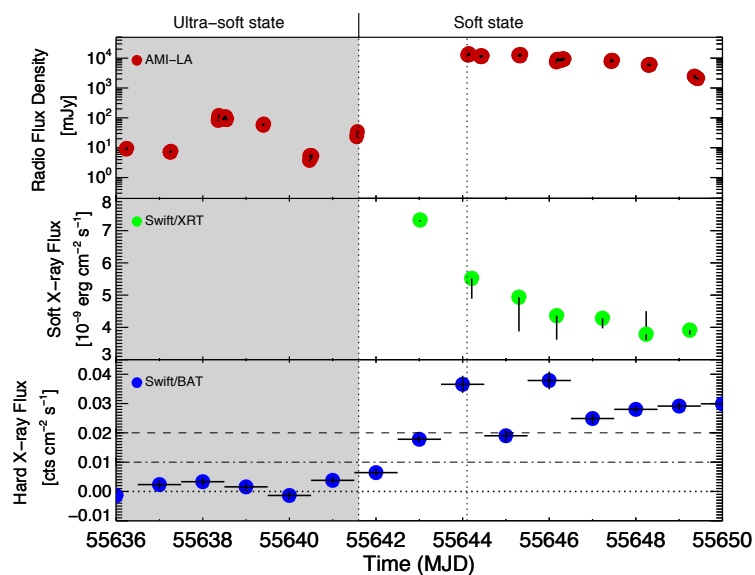
Figure 7.6.: AMI-LA (15 GHz, upper panel), Swift/XRT (1-8 keV, middle panel) and Swift/BAT (15-50 keV, lower panel). Hard X-ray response to major radio flare at the exit of the quenched state.
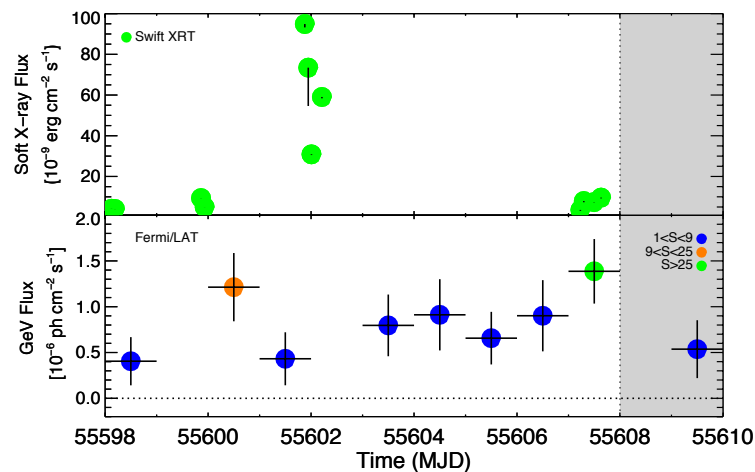

Figure 7.7.: Swift/XRT (upper panel, 1-8 keV) and Fermi/LAT (0.1-300 GeV, lower panel).

8. Multi-Wavelength Observations of Cygnus X-1

I have also been involved in the multi-wavelength campaign of Cygnus X-1, which was observed from radio wavelengths to TeV energies during the soft X-ray state, on 21-26, October, 2011. The instruments involved in the campaign were the VLBA/EVN and AMI-LA (radio), Swift/UVOT (UV), RXTE/ASM, Swift/XRT and MAXI (soft X-ray), Swift/BAT (hard X-ray), Fermi/LAT (GeV) and VERITAS (TeV). The motivation to observe Cygnus X-1 stems from the radio flaring that occurs in the transition between soft and hard X-ray states, since the radio flaring is believed to be linked to the GeV/TeV production [139]. The simultaneous coverage will lead to an accurate characterization of the SED over a broad band permitting detailed studies of the source, and will improve the understanding of the fundamental acceleration processes in accreting compact objects. My work has been primarily on the GeV/TeV observations from Fermi LAT and VERITAS, respectively. These results have been presented at the 219th Winter AAS Meeting in Austin, TX (2012) in the poster session [140].

Cygnus X-1 is one of the brightest X-ray sources known. It is formed by a compact object and the O9.7 Iab supergiant star HDE 226868, with a mass of 19.2 ± 1.9 M$_\odot$. The mass of the compact object is 14.8 ± 1.0 M$_\odot$, which confirms the existence of a black hole [141]. Black-hole binaries are known to exist either in a low/hard or high/soft X-ray emission state. Cygnus X-1 is known to flare in the X-rays on a timescale of months to seconds, while a non-thermal radio jet has been observed as well. Both features classify Cygnus X-1 as a microquasar. The high-energy particles in the radio-emitting jets may well produce gamma rays. A TeV excess of 4.1σ has been observed by the MAGIC Cherenkov telescope, at a position spatially consistent with Cygnus X-1, during a hard X-ray flare taking place in the low/hard state [61]. AGILE (GeV) has reported gamma-ray events at the increase in the soft X-ray emission (ATel #2715 [62]).
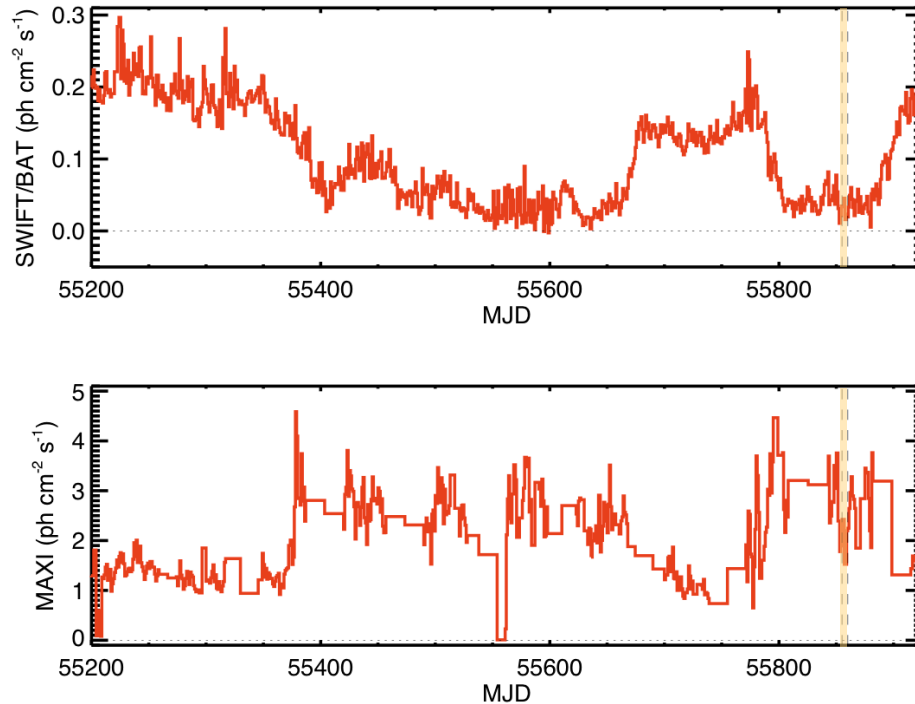
Figure 8.1.: Swift/BAT (15-50 keV, top) and MAXI (2-20 keV, bottom) X-ray light curves of Cygnus X-1. In this figure we can notice the anti-correlation between the hard X-ray with respect to the soft X-ray. The multi-wavelength campaign period is shown in the shaded area on the right.

8.1 Observations & Data Reduction

Observations were undertaken, in conjunction with VBLA/EVN radio, RXTE PCA and Swift XRT/UVOT pointed observations, for a total of 7 hours 12 minutes of quality-assessed data, from 21 to 26 October, 2011. At the 99% confidence level, no TeV emission was detected by VERITAS during the campaign, both for daily observations and for the time-integrated observation. Data from the Fermi/LAT was also analyzed for the same time interval. For the Fermi/LAT, we plot at the 99% confidence level the one-day flux upper limits and marginal detections of Cygnus X-1 during the multi-wavelength campaign span.
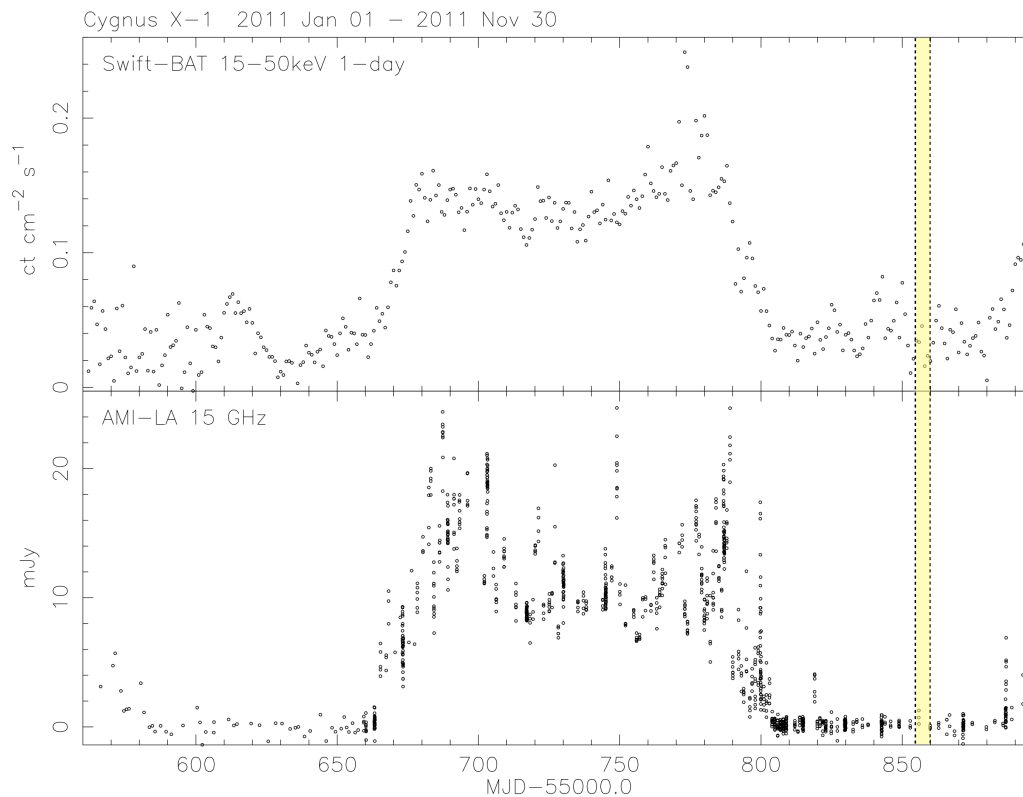
Figure 8.2.: Swift/BAT (15-50 keV, top) and AMI-LA (15 GHz, bottom) X-ray/radio light curves of Cygnus X-1. For 2011, the low activity in the hard X-ray and radio states are visible on both sides of the radio-active/hard X-ray period at the center. The VERITAS multi-wavelength campaign period is visible in the shaded area.

8.1.1   VERITAS

For the reduction of the VERITAS Cygnus X-1 data, the analysis procedure was very similar to the procedure that was used for the Cygnus X-3 data reductions. More details of the general VERITAS analysis can be viewed in the Section 2.3. The moon light was of no concern during the campaign, while weather was an issue for the night of 25 October, 2011. The VERITAS observations were conducted in wobble mode. The selection-criteria parameters for the Cygnus X-1 data analysis were based on the same parameters which were applied in the Cygnus X-3 data analysis. Different selection-criteria parameters, based on energy event hardness, were employed to

Table 8.1: Summary of VERITAS Observations for Cygnus X-1

MJD	Calendar Date	Observing Time (min)	Elevation Range	N_{tel}
55855	2011/10/21	123	$56^{o} - 81^{o}$	4
55856	2011/10/22	32	$55^{o} - 80^{o}$	4
55857	2011/10/23	74	$56^{o} - 71^{o}$	4
55858	2011/10/24	116	$55^{o} - 80^{o}$	4
55859	2011/10/25	20	$56^{o} - 60^{o}$	4
55860	2011/10/26	67	$55^{o} - 69^{o}$	4

Note - The column N_{tel} shows the number of working telescopes.

search for the maximum possible significance of the events. The acceptance correction was calculated and applied in the same manor as in the Cygnus X-3 data reduction. See subsection 6.1.2 of Chapter 7 for more details concerning the data reduction. The one-day VERITAS flux upper limits (99% confidence level, 0.1-10 TeV) of Cygnus X-1 were calculated for the nightly observations. Details of the nightly observations are shown in Table 8.1 and the plot with the VERITAS flux upper limits can be found in Figure 8.3.

8.1.2 Fermi/LAT

The procedure that was utilized for the Fermi LAT data analysis is very similar to the procedure employed for Cygnus X-3 (subsection 6.1.3 of Chapter 7). In the case of background modeling, all of the sources in the Fermi Large Area Telescope Second Source (2FGL) Catalog [70] that were in the vicinity of Cygnus X-1 were used. For the possible intrinsic variability of the sources, the spectral parameters of the sources in a 10°-radius region of interest (RoI) were allowed to vary in an unbinned maximum likelihood analysis. On the other hand, the spectral parameter values of the 2FGL sources outside of the RoI but within a 20°-radius source region were kept fixed. The peak-pulse emission from the bright pulsar PSR J2021+3651 (4.88° from Cygnus
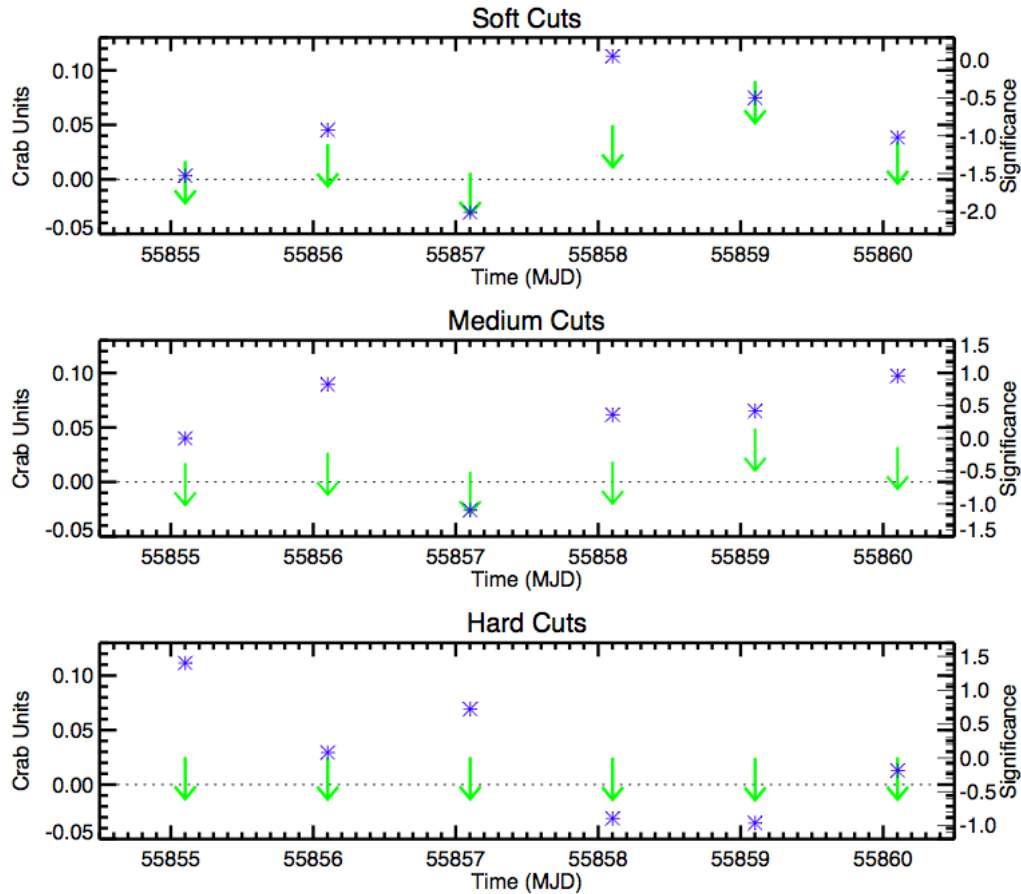
Figure 8.3.: One-day VERITAS flux upper limits (99% confidence level, 0.1-10 TeV) of Cygnus X-1, together with significances of daily observations. Different selection-criteria parameters, based on energy event hardness, were used in the VERITAS plot to search for the maximum significance of the events.

X-1 [142]) were excluded from the analysis, based on the pulsar ephemeris[1]. Peak-pulse emission accounts for 55% of emission in 20% of the phase, due to the narrow peaks. After removal, the remaining data is incremented in photon flux by 25% to account for previous data rejection. As for the Galactic and extragalactic diffuse gamma-ray backgrounds, we adopted the most recent models (*gal_2yearp7v6_v0.fits* and *iso_p7v6source.txt*). We also modeled the emission from the Cygnus Loop region

[1]The pulsar ephemeris for PSR J2021+3651 is available at: `http://www.slac.stanford.edu/~paulr/LATPulsarTimingModels/Latest/J2021+3651/kerr2013-07-15.par`
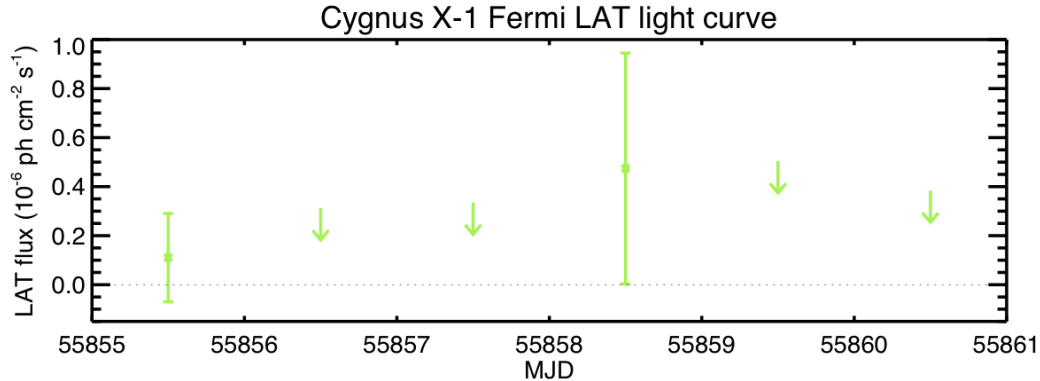
Figure 8.4.: One-day Fermi LAT light curve (0.1-100 GeV) of Cygnus X-1; for intervals when the source was not detected, the arrows show the 99% confidence level flux upper limits. Error bars are at the 1σ level. Two marginal detections result consistent with zero.

with a template that is provided in the LAT Catalog Data Products. The instrument response function (IRF) used in this work is IRF P7SOURCE_V6. The energy range was set from 0.1-100 GeV.

8.2   Results & Discussion

VERITAS has observed Cygnus X-1 over 7 hours and 12 minutes, for a 99% confidence level integral flux upper limit (E>300 GeV) of 1.0% crab. The MAGIC 95% confidence level integral flux upper limit to the steady flux of Cygnus X-1, in the range between 150 GeV and 3 TeV, is of the order of 1%–5% of the Crab Nebula flux, for 40 hours of useful data (September–November 2006). The MAGIC post-trial 4.1σ significance detection, in coincidence with a hard X-ray flare, is reported at 10.6% crab for E>300 GeV (Albert et al. 2007), while the AGILE report of a GeV emission from Cygnus X-1, in the low/hard state (15-16 October, 2009) is stated at an integral flux of 77% crab (0.1-3 GeV), at the 4σ post-trial significance. (Sabatini et al. 2010). Beside this episode, AGILE reports no detection, with a 2σ significance 99% confidence level integral flux upper limit (E>300 GeV) of 1.0% crab. We obtain

0.17σ significance 99% confidence level integral flux upper limit (E>0.1 GeV) of 4.8% crab, over the campaign period. Both these claims highlight the elusive nature of TeV emission, suggesting that the duration of the emission mechanism must be brief, at ~1 day. VERITAS observations correspond to a period when very minor radio activity was seen, as would be expected in the soft X-ray state. A detailed, overall SED of the high/soft X-ray state is expected when the radio, soft and hard X-ray results become available.

9. GeV & TeV Observations of Microquasars

9.1 Introduction

Microquasars have been considered as viable sites of gamma-ray emission, due to their similarities to AGN. The acceleration of particles in the jet with the subsequent inverse-Compton upscattering of ambient photons, during the active states of the microquasar, hold sway as one of the possible scenarios where galactic gamma-ray emission might occur. The competing model for gamma-ray emission in X-ray binaries consists of the shocked pulsar winds of rotation-powered pulsars. A minimum mass of $> 3\,M_\odot$ for the compact object would rule out the pulsar scenario, while pulsations from the compact object would confirm the rotation-powered pulsar interpretation. Evidence for either has proven elusive, so each interpretation has relied on indirect suggestions.

Five are the gamma-ray binaries that have been discovered so far: PSR B1263-59, LS I +61°303, LS 5903, HESS J0632+057 and 1FGL J1018.6-5856. All of these gamma-ray binaries are HMXBs and radio sources, which is uncommon among the greater population of HMXBs. The discovery of elongated radio emission at the milliarcsecond level in LS I +61°303 and LS 5039 prompted the idea of relativistic jets in a microquasar environment. The high-energy (HE; >0.1 GeV) spectra of gamma-ray binaries, with the exception of HESS J0632+057 which isn't detected in the GeV range, consist of a power law with an exponential cutoff, which is a hallmark of pulsars, and used as a criterion for pulsar-candidate identification in Fermi/LAT sources. On the other hand, the orbital variability of the HE GeV spectrum and the X-ray flaring episodes on the timescales of 1-1000 s advocate for the microquasar explanation. A review for both competing models can be view in [18].

9.2   Observations

The wealth of GeV and TeV gamma-ray data at our disposal was readily taken advantage of in the search for possible gamma-ray emission from galactic microquasars. From 2007 to 2009, VERITAS carried out a 150-hour survey of a $15° \times 5°$ area, in Galactic longitude and latitude respectively, of the Cygnus Region of the Galaxy, with a uniform point-source sensitivity (99% C.L.) of $< 4\%$ of the Crab Nebula flux [143]. Within the VERITAS sky survey data, there was only one microquasar with sufficient coverage from which a flux upper limit could be calculated. This is the microquasar Ginga 2023+338 (V 404 Cyg). The observations of the source span the period from 21 to 25 June, 2007 and from 14 to 15 September, 2007, for a total exposure of 111.296 minutes (1.85 hours). See Table 9.1 for the results of the TeV analysis.

On the other hand, due to the constant all-sky coverage provided by Fermi/LAT which covers the entire sky every 3.5 hours, an analysis was performed of the list of black-hole binaries from Table 4.1 of the book "Compact Stellar X-ray Sources", by Lewin & Van der Klis [144]. The list contains many sources that are visible at the latitude of VERITAS, but also sources that are seen from the southern sky as well. The results of this work have been presented at the Workshop on High Energy Galactic Physics at Columbia University, 28-29 May, 2010. See Table 9.2 for the results of the GeV analysis.

9.3   Data Reduction

VERITAS data reduction was performed in a manner very similar to what is described in the previous section (see Subsection 6.1.2 for more details). More details of the general VERITAS analysis can be viewed in the Section 2.3. The analysis on Ginga 2023+338 was performed with selection-criteria parameters optimized for a putative source with a soft spectral index. The selection criteria parameters for soft sources was chosen since these parameters provided the highest significance in the analysis.

On the other hand, the Fermi/LAT analysis was performed with the Fermi Science Tools v9r18p6, except for SS 433 which was analyzed with the version v9r23p1. To accommodate for the possible change in the intrinsic flux of the sources, the spectral parameters of the sources in a 8°-radius region of interest (RoI) around the target were set to vary in an unbinned maximum likelihood analysis, while the spectral parameters of the sources outside of the RoI but within a 13°-radius source region were frozen at their 11-month Fermi Catalog values (0FGL) [145]. In the case of LMC X-3, the unidentified source at the galactic coordinates (J2000) $l°$=277.57 and $b°$=-25.54 was added to the background model. The full 0.1-300 GeV energy range was selected. The Galactic and extragalactic diffuse gamma-ray backgrounds were represented by the *gll_iem_v02* model and by an isotropic component, respectively. The instrument response function (IRF) used in this work is IRF P6_V3_DIFFUSE.

9.4 Results

The Table 9.1 does not claim to be representative of the TeV emissions from the microquasar Ginga 2023+338, since it is limited by the particular low exposure of the VERITAS sky survey observations on the region of the microquasar. The same can be send of the Table 9.2 on microquasar emission in the GeV range, being limited to the period from the beginning of Fermi/LAT observations to mid 2011. Nevertheless, both represent a tentative start on the HE and VHE emission in microquasars.

Table 9.1: Properties of V 404 Cyg & VERITAS Flux Upper Limit

Source	Type	Distance (kpc)	Orbital Period (hours)	Flux Upper Limit[†] (10^{-12} cm^{-2} s^{-1})	Crab Units (%)
Ginga 2023+338 (V404 Cyg)	LMXB, Transient	2.2 - 3.7	155.3	1.4	1.0

[†]Flux upper limits are calculated for $E >$0.3 TeV (99% C.L.).
LMXB - Low-mass X-ray binary.

Table 9.2: Properties of Confirmed Black Hole Binaries & LAT Flux Upper Limits

Source	Type	Distance (kpc)	Orbital Period (hours)	Flux Upper Limit[†] $(10^{-8}\ \text{cm}^{-2}\ \text{s}^{-1})$	Time Interval
GRS 1915+105 (V1487 Aql)	LMXB, Transient	11 - 12	804.0	2.6	2008/08/04 - 2011/05/16
1A0620-00 (V616 Mon)	LMXB, Transient	1.2 ± 0.1	7.8	0.3	2008/08/04 - 2011/05/16
GRO J0422+32 (V518 Per)	LMXB, Transient	11	9.2	0.5	2008/08/04 - 2011/05/16
GRS 1009-45 (MM Vel)	LMXB, Transient	5.0 ± 1.3	6.8	0.8	2008/08/04 - 2011/05/16
Ginga 1124-684 (GU Mus)	LMXB, Transient	5.0 ± 1.3	10.4	1.9	2008/08/04 - 2011/05/16
LMC X-3	HMXB, Persistent	50.0 ± 2.3	40.9	2.6	2008/08/04 - 2011/05/16
Ginga 2000+251 (QZ Vul)	LMXB, Transient	2.7 ± 0.7	8.3	0.9	2008/08/04 - 2011/05/16
3A 1705-25 (V2107 Oph)	LMXB, Transient	8 ± 2	12.5	0.6	2008/08/04 - 2011/05/16
XTE J1859+226 (V406 Vul)	LMXB, Transient	11	9.2	3.6	2008/08/04 - 2011/05/20
XTE J1819+254 (V4641 Sgr)	LMXB, Transient	7.4 ± 12.3	67.6	1.3	2008/08/04 - 2011/05/23
XTE J1118+480 (KV UMa)	LMXB, Transient	1.8 ± 0.5	4.1	0.5	2008/08/04 - 2011/05/26
SS 433 (V1343 Aql)	HMXB, Transient	5	312	2.1	2008/08/04 - 2011/06/10
Cygnus X-1 (V1357 Cyg)	HMXB, Persistent	2.0 ± 0.1	134.4	1.3	2008/08/04 - 2010/03/26
Ginga 2023+338 (V404 Cyg)	LMXB, Transient	2.2 - 3.7	155.3	10.3	2008/08/04 - 2010/03/20
GRO J1655-40 (V1033 Sco)	LMXB, Transient	3.2 ± 0.2	62.9	2.1	2008/08/04 - 2010/03/20

[†]Flux upper limits are calculated for $E > 0.1$ GeV (99% C.L.).
LMXB - Low-mass X-ray binary
HMXB - High-mass X-ray binary

9.5 Discussion

Several are the consideration that stem from the previous results. Microquasars may emit high-energy radiation in certain gamma-ray active states, such as the case for the gamma-ray emission in Cygnus X-3 in the hypersoft state. Cygnus X-3 has shown evidence for persistent gamma-ray emission in the Fermi/LAT energy range, over periods of ~10 days. There is also evidence for some new episodes of transient gamma-ray emission in Cygnus X-3 that have previously gone undetected [146]. A valid plan of attack for detection of GeV emission from microquasars may come from limiting the analysis to periods where the conditions for emission may be more favorable.

Of the five gamma-ray binaries that are currently known, all are HMXBs. Gamma-ray emission has been observed from Cygnus X-3 and possibly from Cygnus X-1, and both are HMXBs. A massive and luminous stellar companion may be a necessary requirement for gamma-ray emission in binary systems. It has also be noted that the gamma-ray emission is strongly dependent on the orbital phase. This characteristic has been observed in PSR B1263-59, LS I +61°303, and Cygnus X-3 in the gamma-ray active state.

The flux upper limits in the list can start to place some constraints on gamma-ray emission from microquasars, since even a non-detection can be helpful in some cases. The recent results on Cygnus X-1 in the 0.1-10 GeV energy range have shown a 4σ flux upper limit on the gamma-ray emission in the hard X-ray state. Even though an upper limit, this starts to place a strong constraint on the Compton emission of the steady radio jet which is present in that state [147]. Flux upper limit results from other microquasars such as GRS 1915+105 and GX 339-4 has also been reported in the literature as well [146].

With a total of almost 5-years worth of Fermi/LAT data, the Pass7 IRF and new data analysis tools (v9r31p1), and with the selection of appropriate source states, it may very well be that these sources may still reveal some unexpected gamma-ray

emission. The sources of the list could still possess weak steady GeV emission, and may also reveal themselves in episodes of transient emission. There is still much that we can discover with the current instruments at our disposal about microquasars.

10. Summary

The investigation of situations in X-ray binaries where gamma-ray emission could occur has given us a picture of the processes of high-energy emission and very-high-energy emission that is puzzling and complex, to say the least. Clearly, the situations of extreme X-ray outbursts in X-ray binaries are not all equivalent. 1A 0535+262 has shown us the even in the case of a major X-ray outburst, gamma-ray emission is not a guaranteed outcome. There are cases of X-ray binaries, such as GRS 1915+105, that have persistent, extreme physical conditions of accretion and jet emission, but that do not lead to gamma-ray emission that we can detect with the instruments currently in our possession. As for the case of Cygnus X-3, which is a known GeV source, the case for persistent very-high-energy emission seems to be beyond the reach of the current class of ground-based IACTs. The conditions for episodic emission though can still make the case to persist in the observations of Cygnus X-3 and sources similar to this famous microquasar. Many are the conditions that we need to take into account for these types of systems for the possible production of gamma rays: the geometry (e.g. jet and disk orientation), the absorption processes such as pair production and the energetics which involve the accelerations of particles along the magnetic field of the jet.

LIST OF REFERENCES

LIST OF REFERENCES

[1] Philip Morrison. On gamma-ray astronomy. *Il nuovo cimento*, 7(6):858–865, 1958.

[2] V. Schönfelder. The history of gamma-ray astronomy. *Astronomische Nachrichten*, 323:524–529, July 2002.

[3] K. Pinkau. History of gamma-ray telescopes and astronomy. *Experimental Astronomy*, 25:157–171, August 2009.

[4] G. Cocconi. An air shower telescope and the detection of 10^{12} eV photon sources. In *International Cosmic Ray Conference*, volume 2 of *International Cosmic Ray Conference*, page 309, 1960.

[5] J. E. Grindlay. Monte Carlo calculations of nuclear cascades and associated Cerenkov radiation in extensive air showers. Phys. Rev. D, 11:517–522, February 1975.

[6] T. C. Weekes et al. Observation of TeV gamma rays from the Crab nebula using the atmospheric Cerenkov imaging technique. ApJ, 342:379–395, July 1989.

[7] T. C. Weekes. TeV Gamma-ray Astronomy: The Story So Far. In F. A. Aharonian, W. Hofmann, and F. Rieger, editors, *American Institute of Physics Conference Series*, volume 1085 of *American Institute of Physics Conference Series*, pages 3–17, December 2008.

[8] R. C. Lamb et al. Observation of gamma rays with a 4.8 hour periodicity from Cygnus X-3. ApJ, 212:L63–L66, March 1977.

[9] K. Bennett, G. Bignami, W. Hermsen, H. A. Mayer-Hasselwander, J. A. Paul, and L. Scarsi. Search for gamma-ray emission with a 4.8 H periodicity from Cygnus X-3. A&A, 59:273, July 1977.

[10] A. Daum et al. First results on the performance of the HEGRA IACT array. *Astroparticle Physics*, 8:1–11, December 1997.

[11] J.A Hinton. The status of the HESS project. *New Astronomy Reviews*, 48(5-6):331–337, 2004. 2nd VERITAS Symposium on the Astrophysics of Extragalactic Sources.

[12] J. Aleksić et al. Performance of the MAGIC stereo system obtained with Crab Nebula data. *Astroparticle Physics*, 35:435–448, February 2012.

[13] J. Kildea et al. The Whipple Observatory 10 m gamma-ray telescope, 1997 2006. *Astroparticle Physics*, 28:182–195, October 2007.

[14] D. Kieda. Status of the VERITAS Upgrade. In *International Cosmic Ray Conference*, volume 9 of *International Cosmic Ray Conference*, page 14, 2011.

[15] J. Holder et al. VERITAS: Status and Highlights. In *Proc. of the 32nd Int. Cosmic Ray Conf., Vol. 12, 137, Beijing, China*, International Cosmic Ray Conference, 2013.

[16] G. B. Rybicki and A. P. Lightman. *Radiative Processes in Astrophysics*. June 1986.

[17] C. D. Dermer and G. Menon. *High Energy Radiation from Black Holes: Gamma Rays, Cosmic Rays, and Neutrinos*. 2009.

[18] G. Dubus. Gamma-ray binaries and related systems. A&A Rev., 21:64, August 2013.

[19] J. V. Jelley and N. A. Porter. Čerenkov Radiation from the Night Sky, and its Application to γ-Ray Astronomy. QJRAS, 4:275, September 1963.

[20] A. M. Hillas. Cerenkov light images of EAS produced by primary gamma. In F. C. Jones, editor, *International Cosmic Ray Conference*, volume 3 of *International Cosmic Ray Conference*, pages 445–448, August 1985.

[21] P. T. Reynolds et al. Survey of candidate gamma-ray sources at TeV energies using a high-resolution Cerenkov imaging system - 1988-1991. ApJ, 404:206–218, February 1993.

[22] P. Cogan. *Nanosecond Sampling of Atmospheric Cherenkov Radiation Applied to TeV Gamma-Ray Observations of Blazars with VERITAS*. PhD thesis, University College Dublin, 2006.

[23] John M. Davies and Eugene S. Cotton. Design of the quartermaster solar furnace. *Solar Energy*, 1(23):16 – 22, 1957. The Proceedings of the Solar Furnace Symposium.

[24] E. Roache, R. Irvin, J. S. Perkins, and et al. Mirror Facets for the VERITAS Telescopes. In *International Cosmic Ray Conference*, volume 3 of *International Cosmic Ray Conference*, pages 1397–1400, 2008.

[25] A. McCann, D. Hanna, J. Kildea, and M. McCutcheon. A new mirror alignment system for the VERITAS telescopes. *Astroparticle Physics*, 32:325–329, January 2010.

[26] D. Kieda. The Gamma Ray Detection sensitivity of the upgraded VERITAS Observatory. In *Proc. 33nd ICRC, Rio de Janeiro, Brazil*, International Cosmic Ray Conference, 2013. To be published.

[27] J. Hall, V. V. Vassiliev, D. B. Kieda, J. Moses, T. Nagai, and J. Smith. Veritas CFDs. In *International Cosmic Ray Conference*, volume 5 of *International Cosmic Ray Conference*, page 2851, July 2003.

[28] B. Zitzer. The VERITAS Upgraded Telescope-Level Trigger Systems: Technical Details and Performance Characterization. In *Proc. 33nd ICRC, Rio de Janeiro, Brazil*, International Cosmic Ray Conference, 2013. To be published.

[29] J. T. Anderson et al. Commissioning and performance of a fast level-2 trigger system at VERITAS. In *Real Time Conference (RT), 2012 18th IEEE-NPSS*, pages 1–5, 2012.

[30] A. Weinstein. The VERITAS Trigger System. In *International Cosmic Ray Conference*, volume 3 of *International Cosmic Ray Conference*, pages 1539–1542, 2008.

[31] J. Holder. Exploiting VERITAS Timing Information. In *International Cosmic Ray Conference*, volume 5 of *International Cosmic Ray Conference*, page 383, 2005.

[32] P. Cogan. VEGAS, the VERITAS Gamma-ray Analysis Suite. In *International Cosmic Ray Conference*, volume 3 of *International Cosmic Ray Conference*, pages 1385–1388, 2008.

[33] R. A. Ong. Very high-energy gamma-ray astronomy. Phys. Rep., 305:93–202, 1998.

[34] D. Berge, S. Funk, and J. Hinton. Background modelling in very-high-energy γ-ray astronomy. A&A, 466:1219–1229, May 2007.

[35] T.-P. Li and Y.-Q. Ma. Analysis methods for results in gamma-ray astronomy. ApJ, 272:317–324, September 1983.

[36] W. B. Atwood et al. The Large Area Telescope on the Fermi Gamma-Ray Space Telescope Mission. ApJ, 697:1071–1102, June 2009.

[37] M. Tavani et al. The AGILE space mission. *Nuclear Instruments and Methods in Physics Research A*, 588:52–62, April 2008.

[38] M. Tavani et al. The AGILE Mission. A&A, 502:995–1013, August 2009.

[39] K. Jahoda et al. In-orbit performance and calibration of the Rossi X-ray Timing Explorer (RXTE) Proportional Counter Array (PCA). In O. H. Siegmund and M. A. Gummin, editors, *Society of Photo-Optical Instrumentation Engineers (SPIE) Conference Series*, volume 2808 of *Society of Photo-Optical Instrumentation Engineers (SPIE) Conference Series*, pages 59–70, October 1996.

[40] A. M. Levine et al. First Results from the All-Sky Monitor on the Rossi X-Ray Timing Explorer. ApJ, 469:L33, September 1996.

[41] S. D. Barthelmy et al. The Burst Alert Telescope (BAT) on the SWIFT Midex Mission. Space Sci. Rev., 120:143–164, October 2005.

[42] M. Matsuoka et al. The MAXI Mission on the ISS: Science and Instruments for Monitoring All-Sky X-Ray Images. PASJ, 61:999–, October 2009.

[43] M. F. Skrutskie et al. The Two Micron All Sky Survey (2MASS). AJ, 131:1163–1183, February 2006.

[44] J. S. Bloom et al. Autonomous Observing and Control Systems for PAIRITel, a 1.3m Infrared Imaging Telescope. In C. Gabriel, C. Arviset, D. Ponz, and S. Enrique, editors, *Astronomical Data Analysis Software and Systems XV*, volume 351 of *Astronomical Society of the Pacific Conference Series*, page 751, July 2006.

[45] J. T. L. Zwart et al. (AMI Consortium). The Arcminute Microkelvin Imager. MNRAS, 391:1545–1558, December 2008.

[46] W. H. G. Lewin, J. van Paradijs, and E. P. J. van den Heuvel. *X-ray Binaries.* January 1997.

[47] Q. Z. Liu, J. van Paradijs, and E. P. J. van den Heuvel. Catalogue of high-mass X-ray binaries in the Galaxy (4th edition). A&A, 455:1165–1168, September 2006.

[48] Q. Z. Liu, J. van Paradijs, and E. P. J. van den Heuvel. A catalogue of low-mass X-ray binaries in the Galaxy, LMC, and SMC (Fourth edition). A&A, 469:807–810, July 2007.

[49] N. I. Shakura and R. A. Sunyaev. Black holes in binary systems. Observational appearance. A&A, 24:337–355, 1973.

[50] L. Stella, N. E. White, and R. Rosner. Intermittent stellar wind accretion and the long-term activity of Population I binary systems containing an X-ray pulsar. ApJ, 308:669–679, September 1986.

[51] J. Albert et al. Variable Very-High-Energy Gamma-Ray Emission from the Microquasar LS I +61 303. *Science*, 312:1771–1773, June 2006.

[52] F. Aharonian et al. 3.9 day orbital modulation in the TeV γ-ray flux and spectrum from the X-ray binary LS 5039. A&A, 460:743–749, December 2006.

[53] F. Aharonian et al. Very high energy γ-ray observations of the binary PSR B1259-63/SS2883 around the 2007 Periastron. A&A, 507:389–396, November 2009.

[54] J. L. Skilton et al. The radio counterpart of the likely TeV binary HESSJ0632+057. MNRAS, 399:317–322, October 2009.

[55] A. Abramowski et al. (H. E. S. S. Collaboration). Discovery of VHE emission towards the Carina arm region with the H.E.S.S. telescope array: HESS J1018-589. A&A, 541:A5, May 2012.

[56] A. A. Abdo et al. Fermi LAT Observations of LS I +61°303: First Detection of an Orbital Modulation in GeV Gamma Rays. ApJ, 701:L123–L128, August 2009.

[57] A. A. Abdo et al. Fermi LAT observations of LS 5039. ApJ, 706:L56–L61, November 2009.

[58] A. A. Abdo et al. Discovery of High-energy Gamma-ray Emission from the Binary System PSR B1259-63/LS 2883 around Periastron with Fermi. ApJ, 736:L11, July 2011.

[59] A. A. Abdo et al. Periodic Emission from the Gamma-Ray Binary 1FGL J1018.6-5856. *Science*, 335:189–, January 2012.

[60] A. A. Abdo et al. (Fermi LAT Collaboration). Modulated High-Energy Gamma-Ray Emission from the Microquasar Cygnus X-3. *Science*, 326:1512–, December 2009.

[61] J. Albert et al. Very High Energy Gamma-Ray Radiation from the Stellar Mass Black Hole Binary Cygnus X-1. ApJ, 665:L51–L54, August 2007.

[62] S. Sabatini et al. AGILE gamma-ray detection of Cygnus X-1. *The Astronomer's Telegram*, 2715:1, July 2010.

[63] A. A. Abdo et al. Fermi Large Area Telescope Observation of a Gamma-ray Source at the Position of Eta Carinae. ApJ, 723:649–657, November 2010.

[64] A. A. Abdo, M. Ackermann, M. Ajello, W. B. Atwood, L. Baldini, J. Ballet, G. Barbiellini, D. Bastieri, K. Bechtol, R. Bellazzini, and et al. Gamma-Ray Emission Concurrent with the Nova in the Symbiotic Binary V407 Cygni. *Science*, 329:817–821, August 2010.

[65] D. R. Lorimer et al. The Parkes Multibeam Pulsar Survey - VI. Discovery and timing of 142 pulsars and a Galactic population analysis. MNRAS, 372:777–800, October 2006.

[66] M. S. E. Roberts. New Black Widows and Redbacks in the Galactic Field. In M. Burgay, N. D'Amico, P. Esposito, A. Pellizzoni, and A. Possenti, editors, *American Institute of Physics Conference Series*, volume 1357 of *American Institute of Physics Conference Series*, pages 127–130, August 2011.

[67] F. A. Aharonian and A. M. Atoyan. Gamma rays from galactic sources with relativistic jets. New A Rev., 42:579–584, December 1998.

[68] L. Maraschi and A. Treves. A model for LS I +61 303. MNRAS, 194:1P–5P, January 1981.

[69] E. J. A. Meurs and E. P. J. van den Heuvel. The number of evolved early-type close binaries in the Galaxy. A&A, 226:88–107, December 1989.

[70] P. L. Nolan et al. Fermi Large Area Telescope Second Source Catalog. ApJS, 199:31, April 2012.

[71] I. F. Mirabel. The Early History of Microquasar Research. *ArXiv e-prints*, June 2012.

[72] I. F. Mirabel and L. F. Rodríguez. A superluminal source in the Galaxy. Nature, 371:46–48, September 1994.

[73] V. Bosch-Ramon and D. Khangulyan. Understanding the Very-High Emission from Microquasars. *International Journal of Modern Physics D*, 18:347–387, 2009.

[74] E. Gallo et al. A dark jet dominates the power output of the stellar black hole Cygnus X-1. Nature, 436:819–821, August 2005.

[75] S. Corbel et al. Large-Scale, Decelerating, Relativistic X-ray Jets from the Microquasar XTE J1550-564. *Science*, 298:196–199, October 2002.

[76] G. E. Romero. Microquasars and Gamma-ray Sources. *Chinese Journal of Astronomy and Astrophysics Supplement*, 5:110–120, June 2005.

[77] S. Johnston, R. N. Manchester, A. G. Lyne, M. Bailes, V. M. Kaspi, G. Qiao, and N. D'Amico. PSR 1259-63 - A binary radio pulsar with a Be star companion. ApJ, 387:L37–L41, March 1992.

[78] V. Dhawan, A. Mioduszewski, and M. Rupen. LS I +61 303 is a Be-Pulsar binary, not a Microquasar. In *VI Microquasar Workshop: Microquasars and Beyond*, 2006.

[79] M. J. Coe, P. Reig, V. A. McBride, J. L. Galache, and J. Fabregat. A 0535+26: back in business. MNRAS, 368:447–453, May 2006.

[80] F. D. Rosenberg, C. J. Eyles, G. K. Skinner, and A. P. Willmore. Observations of a transient X-ray source with a period of 104 S. Nature, 256:628–630, August 1975.

[81] M. H. Finger, R. B. Wilson, and B. A. Harmon. Quasi-periodic Oscillations during a Giant Outburst of A0535+262. ApJ, 459:288, March 1996.

[82] A. Varlotta, G. Maier, and VERITAS. Gamma-Ray/X-Ray Observations Of The Be-pulsar Binary 1A 0535+262 During A Major Outburst. In *American Astronomical Society Meeting Abstracts #217*, volume 43 of *Bulletin of the American Astronomical Society*, page #144.29, January 2011.

[83] V. A. Acciari et al. Gamma-Ray Observations of the Be/Pulsar Binary 1A 0535+262 During a Giant X-Ray Outburst. ApJ, 733:96, June 2011. Reproduced by permission of the AAS.

[84] C. A. Wilson-Hodge, M. H. Finger, A. Camero-Arranz, and V. Connaughton. Rapid Brightening of A0535+26 Observed by Fermi GBM. *The Astronomer's Telegram*, 2324:1, December 2009.

[85] H. Krawczynski et al. Gamma hadron separation methods for the VERITAS array of four imaging atmospheric Cherenkov telescopes. *Astroparticle Physics*, 25:380–390, July 2006.

[86] V. P. Fomin, A. A. Stepanian, R. C. Lamb, D. A. Lewis, M. Punch, and T. C. Weekes. New methods of atmospheric Cherenkov imaging for gamma-ray astronomy. I. The false source method. *Astroparticle Physics*, 2:137–150, May 1994.

[87] M. A. C. Perryman et al. The HIPPARCOS Catalogue. A&A, 323:L49–L52, July 1997.

[88] F. Aharonian et al. The unidentified TeV source (TeV J2032+4130) and surrounding field: Final HEGRA IACT-System results. A&A, 431:197–202, February 2005.

[89] A. A. Abdo et al. Observation of Supernova Remnant IC 443 with the Fermi Large Area Telescope. ApJ, 712:459–468, March 2010.

[90] A. A. Abdo et al. Fermi-LAT Observations of the Geminga Pulsar. ApJ, 720:272–283, September 2010.

[91] A. A. Abdo et al. Fermi Large Area Telescope First Source Catalog. ApJS, 188:405–436, June 2010.

[92] J. R. Mattox et al. The Likelihood Analysis of EGRET Data. ApJ, 461:396, April 1996.

[93] M. Capalbi, M. Perri, B. Saija, F. Tamburelli, and L. Angelini. The Swift XRT Data Reduction Guide, Technical Report 1.2. *http://heasarc.nasa.gov/docs/swift/analysis/xrt_swguide_v1_2.pdf*, 2005.

[94] J. F. Steiner, J. E. McClintock, R. A. Remillard, L. Gou, S. Yamada, and R. Narayan. The Constant Inner-disk Radius of LMC X-3: A Basis for Measuring Black Hole Spin. ApJ, 718:L117–L121, August 2010.

[95] P. Romano et al. Panchromatic study of GRB 060124: from precursor to afterglow. A&A, 456:917–927, September 2006.

[96] E. Kendziorra et al. Evidence for cyclotron line features in high energy spectra of A 0535+26 during the March/April 1989 outburst. A&A, 291:L31–L34, November 1994.

[97] I. Caballero, P. Kretschmar, A. Santangelo, A. Segreto, C. Ferrigno, and R. Staubert. Pulse Period History and Phase Resolved Spectra of 1A 0535+262. In *ESA Special Publication*, volume 622 of *ESA Special Publication*, page 471, 2007.

[98] K. Jahoda et al. Calibration of the Rossi X-Ray Timing Explorer Proportional Counter Array. ApJS, 163:401–423, April 2006.

[99] O. Helene. Upper limit of peak area. *Nuclear Instruments and Methods in Physics Research*, 212:319–322, July 1983.

[100] F. Giovannelli and L. S. Graziati. A 0535 + 26/HDE 245770 - A typical X-ray/Be system. Space Sci. Rev., 59:1–81, January 1992.

[101] G. E. Romero, M. M. Kaufman Bernadó, J. A. Combi, and D. F. Torres. Variable gamma-ray emission from the Be/X-ray transient A0535+26? A&A, 376:599–605, September 2001.

[102] J. E. Grove et al. The soft gamma-ray spectrum of A0535+26: Detection of an absorption feature at 110 keV by OSSE. ApJ, 438:L25–L28, January 1995.

[103] M. Orellana, G. E. Romero, L. J. Pellizza, and S. Vidrih. Very high energy γ-ray emission from X-ray transients during major outbursts. A&A, 465:703–709, April 2007.

[104] W. Bednarek. Inverse Compton $e^{+/-}$ pair cascade model for the γ-ray production in massive binary LSI +61° 303. MNRAS, 371:1737–1743, October 2006.

[105] S. Archambault et al. VERITAS Observations of the Microquasar Cygnus X-3. *ArXiv e-prints*, November 2013. Accepted for publication in ApJ.

[106] P. Predehl, V. Burwitz, F. Paerels, and J. Trümper. Chandra measurement of the geometrical distance to Cyg X-3 using its X-ray scattering halo. A&A, 357:L25–L28, May 2000.

[107] Z. Ling, S. N. Zhang, and S. Tang. Determining the Distance of Cyg X-3 with its X-Ray Dust Scattering Halo. ApJ, 695:1111–1120, April 2009.

[108] M. H. van Kerkwijk, T. R. Geballe, D. L. King, M. van der Klis, and J. van Paradijs. The Wolf-Rayet counterpart of Cygnus X-3. A&A, 314:521–540, October 1996.

[109] A. J. Mioduszewski, M. P. Rupen, R. M. Hjellming, G. G. Pooley, and E. B. Waltman. A One-sided Highly Relativistic Jet from Cygnus X-3. ApJ, 553:766–775, June 2001.

[110] J. C. A. Miller-Jones, K. M. Blundell, M. P. Rupen, A. J. Mioduszewski, P. Duffy, and A. J. Beasley. Time-sequenced Multi-Radio Frequency Observations of Cygnus X-3 in Flare. ApJ, 600:368–389, January 2004.

[111] T. C. Weekes. TeV radiation from galactic sources. Space Sci. Rev., 59:315–364, February 1992.

[112] G. Chardin and G. Gerbier. Cygnus X-3 at high energies - A critical analysis of observational results. A&A, 210:52–65, February 1989.

[113] K. S. O'Flaherty et al. A search for TeV emission from Cygnus X-3. ApJ, 396:674–678, September 1992.

[114] A. Borione et al. High statistics search for ultrahigh energy γ-ray emission from Cygnus X-3 and Hercules X-1. Phys. Rev. D, 55:1714–1731, February 1997.

[115] M. Schilling, O. Mang, and M. Siems. Recent HEGRA Observations of Cygnus X-3. In International Cosmic Ray Conference, volume 6 of International Cosmic Ray Conference, page 2521, August 2001.

[116] J. Aleksić et al. MAGIC Constraints on γ-ray Emission from Cygnus X-3. ApJ, 721:843–855, September 2010.

[117] M. Mori et al. Cygnus X-3 and EGRET Gamma-Ray Observations. ApJ, 476:842, February 1997.

[118] M. Tavani et al. Extreme particle acceleration in the microquasar Cygnus X-3. Nature, 462:620–623, December 2009.

[119] W. Bednarek. On the possibility of sub-TeV -ray emission from CygX-3. MNRAS, 406:689–700, July 2010.

[120] G. Dubus, B. Cerutti, and G. Henri. The relativistic jet of Cygnus X-3 in gamma-rays. MNRAS, 404:L55–L59, May 2010.

[121] G. E. Romero, D. F. Torres, M. M. Kaufman Bernadó, and I. F. Mirabel. Hadronic gamma-ray emission from windy microquasars. A&A, 410:L1–L4, October 2003.

[122] E. B. Waltman, R. L. Fiedler, K. L. Johnston, and F. D. Ghigo. The quiescent level of Cygnus X-3 at 2.25 and 8.3 GHz: 1988-1992. AJ, 108:179–187, July 1994.

[123] M. L. McCollough et al. Discovery of Correlated Behavior between the Hard X-Ray and the Radio Bands in Cygnus X-3. ApJ, 517:951–955, June 1999.

[124] L. Hjalmarsdotter et al. The nature of the hard state of Cygnus X-3. MNRAS, 384:278–290, February 2008.

[125] M. Choudhury, A. R. Rao, S. V. Vadawale, C. H. Ishwara-Chandra, and A. K. Jain. Disk-jet connection in Cygnus X-3. A&A, 383:L35–L38, March 2002.

[126] A. Szostek, A. A. Zdziarski, and M. L. McCollough. A classification of the X-ray and radio states of Cyg X-3 and their long-term correlations. MNRAS, 388:1001–1010, August 2008.

[127] K. I. I. Koljonen, D. C. Hannikainen, M. L. McCollough, G. G. Pooley, and S. A. Trushkin. The hardness-intensity diagram of Cygnus X-3: revisiting the radio/X-ray states. MNRAS, 406:307–319, July 2010.

[128] V. A. Acciari et al. VERITAS Observations of the γ-Ray Binary LS I +61 303. ApJ, 679:1427–1432, June 2008.

[129] S. Corbel et al. A giant radio flare from Cygnus X-3 with associated γ-ray emission. MNRAS, 421:2947–2955, April 2012.

[130] P. S. Ray et al. Precise γ-ray Timing and Radio Observations of 17 Fermi γ-ray Pulsars. ApJS, 194:17, June 2011.

[131] F. Aharonian et al. Observations of 54 Active Galactic Nuclei with the HEGRA system of Cherenkov telescopes. A&A, 421:529–537, July 2004.

[132] W. A. Rolke, A. M. López, and J. Conrad. Limits and confidence intervals in the presence of nuisance parameters. *Nuclear Instruments and Methods in Physics Research A*, 551:493–503, October 2005.

[133] A. A. Zdziarski, C. Maitra, A. Frankowski, G. K. Skinner, and R. Misra. Energy-dependent orbital modulation of X-rays and constraints on emission of the jet in Cyg X-3. MNRAS, 426:1031–1042, October 2012.

[134] M. Tavani et al. AGILE detection of the gamma-ray source AGL J2030+4043. *The Astronomer's Telegram*, 1827:1, November 2008.

[135] M. Tavani et al. AGILE detection of a possible rebrightening of the gamma-ray source AGL J2021+4032 in the Cygnus Region. *The Astronomer's Telegram*, 1848:1, November 2008.

[136] G. Piano et al. The AGILE monitoring of Cygnus X-3: transient gamma-ray emission and spectral constraints. A&A, 545:A110, September 2012.

[137] A. Varlotta. Multi-wavelength observations of Cygnus X-3. In *X-ray Binaries. Celebrating 50 Years Since the Discovery of Sco X-1*, July 2012.

[138] A. Bulgarelli et al. AGILE detection of Cygnus X-3 γ-ray active states during the period mid-2009/mid-2010. A&A, 538:A63, February 2012.

[139] S. Sabatini et al. Gamma-Ray Observations of Cygnus X-1 above 100 MeV in the Hard and Soft States. ApJ, 766:83, April 2013.

[140] A. Varlotta and VERITAS Collaboration. Multi-wavelength Observations of Cygnus X-1. In *American Astronomical Society Meeting Abstracts #219*, volume 219 of *American Astronomical Society Meeting Abstracts*, page #149.05, January 2012.

[141] J. A. Orosz et al. The Mass of the Black Hole in Cygnus X-1. ApJ, 742:84, December 2011.

[142] A. A. Abdo et al. Pulsed Gamma-rays from PSR J2021+3651 with the Fermi Large Area Telescope. ApJ, 700:1059–1066, August 2009.

[143] A. Weinstein and for the VERITAS Collaboration. The VERITAS Survey of the Cygnus Region of the Galactic Plane. *ArXiv e-prints*, December 2009.

[144] W. H. G. Lewin and M. van der Klis. *Compact Stellar X-ray Sources*. April 2006.

[145] A. A. Abdo et al. Fermi/Large Area Telescope Bright Gamma-Ray Source List. ApJS, 183:46–66, July 2009.

[146] A. Bodaghee, J. A. Tomsick, K. Pottschmidt, J. Rodriguez, J. Wilms, and G. G. Pooley. Gamma-Ray Observations of the Microquasars Cygnus X-1, Cygnus X-3, GRS 1915+105, and GX 339-4 with the Fermi Large Area Telescope. ApJ, 775:98, October 2013.

[147] D. Malyshev, A. A. Zdziarski, and M. Chernyakova. High-energy gamma-ray emission from Cyg X-1 measured by Fermi and its theoretical implications. MNRAS, 434:2380–2389, September 2013.

VITA

VITA

Angelo Varlotta was born in Pittsburgh, PA (USA), from Italian parents who had lived and worked in the USA for almost 30 years. After attending elementary school in the USA, the family decided to move back to Italy, where he attended middle school and high school in Vercelli, Italy and then college in Torino, Italy at the Univsersità degi studi di Torino, graduating with a MS in physics and a specialization in theoretical astrophysics. After working for several years, the itch for astrophysics came back, and he decided to attend Michigan State University, in East Lansing, MI, receiving a MS in Astronomy & Astrophysics in 2006. Still not quite satisfied, he came to West Lafayette to Purdue University and obtained a PhD in high-energy astrophysics under Prof. Wei K. Cui in 2013. In a postdoctoral position, he will now start working in Cambridge, MA at the Harvard-Smithsonian Center for Astrophysics, continuing his work in multi-wavelength observations of Cygnus X-3.